

https://dspace.org/

Surface brillouin scattering (SBS) study of photoelastic properties of transparent materials

Dube, Hlosani Ngqongqotshi

2019

https://hdl.handle.net/10539/28812

Downloaded from a DSpace repository. https://dspace.org/



SURFACE BRILLOUIN SCATTERING (SBS) STUDY OF PHOTOELASTIC PROPERTIES OF TRANSPARENT MATERIALS.

Hlosani Ngqongqotshi Dube

A dissertation submitted to the Faculty of Science, University of the Witwatersrand, Johannesburg, in fulfillment of the academic requirements for the degree of Master of Science.

Johannesburg, February 2019

Declaration

I, the undersigned, declare that the analysis and results presented here are my original work and was carried under the guidance of Dr. B. Mathe (supervisor) and Prof. D. Wamwangi (co-supervisor). The use of other sources in this work has been duly acknowledged. This dissertation is being submitted for a Master of Science at the University of the Witwatersrand, Johannesburg and has not been submitted before for any degree or examination at any other University.

06 February 2018	
Date	Hlosani Ngqongqotshi Dube

Abstract

Brillouin spectroscopy (BS) was employed to investigate the elastic constants of bulk (strontium fluoride (SrF_2) and thin film (silicon carbide (SiC)) materials. Results of volume scattering experiments on SrF_2 provided an excellent baseline study of bulk modes which proved invaluable in the analysis of the scattering profile generated by the complex system of a-SiC films grown on transparent substrates in this unique study.

In this study, SrF_2, which has continued to be of technological interest because of its fast ion conductivity in the vicinity of its melting point, has its elastic constants measured using Brillouin scattering. Independent elastic constants of SrF_2 were determined from SBS measurements and were found to be $c_{11} \approx 116$ GPa, $c_{12} \approx 45$ GPa and $c_{44} \approx 33$ GPa. These values agree very well with those in literature.

SiC continues to receive intensive interest due to its applicability in micro electromechanical systems (MEMS) operating in harsh environments. In this study, amorphous thin films of SiC were deposited on different substrates using magnetron sputtering.The elastic constants of SiC thin films deposited on sapphire and silicon were obtained by inverse extraction of elastic constants using elastodynamic Green's function applied to the phonon dispersion curves. The films were characterized using microscopic and x-ray techniques, amongst others. The elastic constants of the amorphous films on sapphire were obtained as $c_{11} \approx 250$ GPa and $c_{44} \approx 74$ GPa and for amorphous films on silicon substrate were $c_{11} \approx 160$ GPa and $c_{44} \approx 100$ GPa. Some very interesting anomalous loading effects of the different substrates were observed. The analysis of the dispersion curves of thin SiC/substrate combinations characterized by stiffness effects showed the appearance of anomalous behavior in a range of small normalized thickness. Thus, the evolution of the dispersion curves are not only influenced by velocity but also by densities of the respective film/substrate materials.

To my parents:

"Your teachings and support have led here thus far.
eMpofu!"

To my fiancé:

"This is to our future"

Acknowledgements

This dissertation has been a success as a result of various contributions from interested individuals. I would like to express my sincere gratitude to my supervisors Dr. B. A. Mathe and Prof. D. Wamwangi for their support in grooming me to be the researcher I am. I also would like to thank them for their time, accommodating me for consultations even in none working hours and days. I would also like to express appreciation of their expertise and their constructive feedback from reading through the drafts of this dissertation. A researcher was born out of your determination and love of physics.

Special thanks goes to:

- Dr R. Erasmus from the School of Physics for helping with Raman spectroscopy measurements and analysis.
- Prof. A. Ziegler for training and granting access to the microscopy and micro-analysis unit in the School of Molecular and Cell Biology.
- Prof. D. Billing and Prof. D. Wamwangi for granting access to the X-Ray diffraction facility and Mr Adam Shnier for helping with X-Ray measurements.
- My family, colleagues and fellow students for their support through out these studies.
- The DST-NRF Centre of Excellence in Strong Materials (CoE-SM) and African Laser Centre (ALC) program for the financial support.
- The School of Physics staff for the administrative work done towards the completion of this research work.
- Our creator, we live and strive under his mercy.

Contents

Declaration i

Abstract ii

Dedication iii

Acknowledgements iv

List of figures x

List of tables xi

Chapter 1 1

1 Introduction 1

1.1 Brief background 3

1.2 Problem statement 4

1.2.1 Significance of the study 5

1.3 Study objectives 5

1.4 Dissertation outline 5

Chapter 2 7

2 Theoretical principles 7

2.1 Introduction 7

2.1.1 Elastic properties of solid materials 7

2.1.2 Elastic wave propagation 11

2.2 Brillouin scattering spectroscopy 14

2.2.1 Brillouin scattering mechanisms 14

2.2.2 Surface Brillouin scattering : Green's function 19

2.3 Thin film deposition 21

2.3.1 Radio Frequency (RF) magnetron sputtering 22

2.4 Summary 23

Chapter 3 **24**

3 Experimental techniques **24**

3.1 Introduction 24
3.2 Radio-Frequency magnetron sputtering 24
3.3 Raman Spectroscopy 26
3.4 Scanning electron microscopy and EDS 27
3.5 Grazing incidence X-ray diffraction (GIXRD) 28
3.6 X-ray reflectivity (XRR) 30
3.7 Rutherford backscattering 31
3.8 Optical Spectroscopy (Transmittance) measurements 32
3.9 SBS: Experimental setup 32
3.9.1 The laser 33
3.9.2 The tandem Fabry-Pérot interferometer (TFPI) 35
3.9.3 Photo - detectors 37
3.9.4 The multichannel analyzer 37
3.9.5 Alignment of the TFPI for SBS measurements 37
3.9.6 Error analysis in SBS measurements 39
3.10 Summary 39

Chapter 4 **40**

4 Elastic constants of transparent bulk material (SrF_2) **40**

4.1 Introduction 40
4.2 Characterization of SrF_2 40
4.2.1 Raman spectroscopy results 41
4.2.2 XRD results 42
4.2.3 EDS results 43
4.3 Brillouin scattering results on SrF_2 44
4.3.1 Summary 49

Chapter 5 **50**

5 Results and discussion : Characterization studies on (a-SiC) **50**

5.1 Introduction 50
5.1.1 Raman Spectroscopy Results 50
5.1.2 Grazing Incidence X-ray diffraction (GIXRD) Results 52
5.1.3 X-ray reflectometry (XRR) analysis of SiC thin films 54
5.1.4 SEM and EDS Results 57
5.1.5 Optical spectroscopy 60

5.1.6 Rutherford backscattering (RBS) Results 61
5.2 Summary 63

Chapter 6 **64**

6 Surface Brillouin scattering studies on SiC films **64**
6.1 Introduction 64
6.2 SBS on a-SiC films on Sapphire substrate 64
6.2.1 Extraction of effective elastic constants of a-SiC thin films . 69
6.3 SBS on a-SiC films on Si substrate 70
6.3.1 Extraction of effective elastic constants of a-SiC thin films . 71
6.4 Summary 73

Chapter 7 **74**

7 Conclusion and future work **74**

References **76**

Publications **86**

Conference presentations **86**

List of Figures

1.1 SiC power semiconductor statistics and forecast 2
1.2 Silicon carbide crystal structure. 3

2.1 General schematic of elasto-optic scattering mechanism 15
2.2 General schematic of ripple scattering mechanism 17
2.3 Computed combined surface and bulk Brillouin spectra 18
2.4 Brillouin scattering configuration and sample geometry 19
2.5 Thornton structure zone model 22

3.1 Pictorial view of the radio-frequency magnetron sputtering system. 25
3.2 Pictorial view of the scanning electron microscopy system. 27
3.3 The AXS Bruker D8 Discover High resolution X-ray diffraction instrument 28
3.4 General schematic of X-Ray diffraction 29
3.5 General schematic of XRR 31
3.6 Surface Brillouin scattering pictorial representation 33
3.7 Surface Brillouin scattering schematic representation 33
3.8 Laser source measurements 34
3.9 Pictorial view of the tandem Fabry-Pérot interferometer 35
3.10 Schematic view of two Fabry-Pérot interferometers on a translation stage 36
3.11 Diagrammatic representation of the pre-alignment process for the TFPI system. 38

4.1 Unit cell of SrF_2 known as the fluorite structure 41
4.2 Raman Spectrum of SrF_2 42
4.3 X-Ray diffraction pattern of SrF_2 43
4.4 Energy dispersion X-Ray spectroscopy pattern of SrF_2 43
4.5 Brillouin scattering spectra of SrF_2 bulk sample 44
4.6 Frequency dispersion plot for modes observed in the SrF_2 Brillouin spectra 45
4.7 Azimuthal dispersion plot for mode A in SrF_2 Brillouin spectra . . 47

4.8 Azimuthal dispersion plot for mode C in SrF_2 Brillouin spectra . . . 47
4.9 Azimuthal dispersion plot for mode B in SrF_2 Brillouin spectra . . . 48

5.1 Raman spectra of the as-prepared film on sapphire 51
5.2 Raman spectra of the as-prepared film on silicon 51
5.3 X-Ray diffraction pattern of a-SiC/Si system 52
5.4 Grazing incidence X-Ray diffraction pattern of a-SiC/Si system . . 53
5.5 Raman Spectra of annealed SiC film 54
5.6 X-ray reflectometry pattern of an a-SiC thin film deposited for three minutes on silicon 55
5.7 X-ray reflectometry pattern of an a-SiC thin film deposited for five minutes on silicon 55
5.8 X-ray reflectometry pattern of an a-SiC thin film deposited for seven minutes on silicon 56
5.9 Graph of film thickness against deposition time 56
5.10 SEM cross sectional image showing thin film thickness measurements 57
5.11 General SEM image of the as deposited a-SiC films 58
5.12 EDS spectra showing the elemental composition of the observed foreign particles 58
5.13 EDS spectra showing the elemental composition of the as deposited film on sapphire 59
5.14 EDS spectra showing the elemental composition of the as deposited film on Si 59
5.15 Optical transmission measurements of a-SiC films 60
5.16 Rutherford backscattering spectra for SiC films deposited for five minutes onto silicon substrate 62
5.17 Rutherford backscattering spectra for SiC films deposited for ten minutes onto silicon substrate 62
5.18 Rutherford backscattering spectra for SiC films deposited for twenty minutes onto silicon substrate 63

6.1 SBS spectra for sapphire substrate and a-SiC thin film on sapphire 65
6.2 Calculated sbs spectra on a-SiC film on Sapphire. 66
6.3 SBS spectra for 145 nm thick a-SiC thin film on sapphire, taken at laser incident angle of 70°. 67
6.4 Frequency dispersion curves of Peak A as the incident angle is varied from 30° to 80°. 68
6.5 Frequency dispersion curves of Peak B and C as the incident angle is varied from 30° to 80°. 68
6.6 Dispersion curves of a-SiC thin film on sapphire. 70

6.7 SBS specra on a-SiC film on Silicon. 71
6.8 Dispersion curves of a-SiC thin film on Si. 72

List of Tables

1.1 Table of electrical and physical properties of Si and SiC 4

2.1 Definition of one index symbols for the strain components 9
2.2 Definition of one index symbols for the stress components 9
2.3 Christoffel's equation solutions for a cubic symmetry 13
2.4 Christoffel's equation solutions for a hexagonal symmetry 13

3.1 SiC thin film deposition parameters. 26

4.1 Experimental SrF_2 elastic constants c_{11}, c_{12} and c_{44} values compared to the literature values. 49

5.1 Table of transmittance measurements at 532 nm relative to a-SiC film thickness.. 61

Chapter 1

Introduction

This study investigates the photo-elastic properties of transparent bulk (Strontium Fluoride (SrF_2)) and thin film (Silicon carbide (SiC)) materials. SrF_2 is a technologically essential bulk transparent material that has exhibited superionic transition or conductivity in the vicinity of the melting point [1]. Besides, it has recently been applied in extreme ultraviolet (EUV) lithography due to its excellent optical properties [2]. Despite the widespread scientific and industrial interest, the elastic properties of SrF_2 and dynamics of bulk acoustic propagations have not been investigated. It thus provides a foundation study on the propagations of acoustic waves in transparent materials, exhibiting anisotropic optical properties.

On the other hand, intensive interest in the mechanical properties of Silicon Carbide (SiC) at micro and nano scales, in recent years, has been driven primarily by device applications of small structures such as thin film systems in Micro Electro Mechanical Systems (MEMS) [3]. For MEMS structures, surface Brillouin scattering (SBS) is one of the best techniques for investigating the layer/substrate interaction by enabling direct measurement of elastic constants. In this study we seek to investigate this interaction between amorphous SiC and elastically hard transparent substrates. MEMS remains a bright spot in the semiconductor world, expanding faster than the overall chip industry. Consumer and mobile applications continue to be the leading MEMS segments despite saturation of the handset and tablet markets. Nevertheless, emerging areas which are envisaged to be the next major drivers of MEMS market growth, include application such as mandates on smart safety sensors which have attained full implementation in automotive industry.

The emerging market for silicon carbide (SiC) power semiconductors is expected to reach nearly $1 billion in 2020. The driving force for this growth is the incessant demand for SiC based products/devices from hybrid and electric vehicles, power supplies and photovoltaic (PV) inverters [3]. Figure 1.1 shows the road map based on more than thirty semiconductor supply-chains and potential

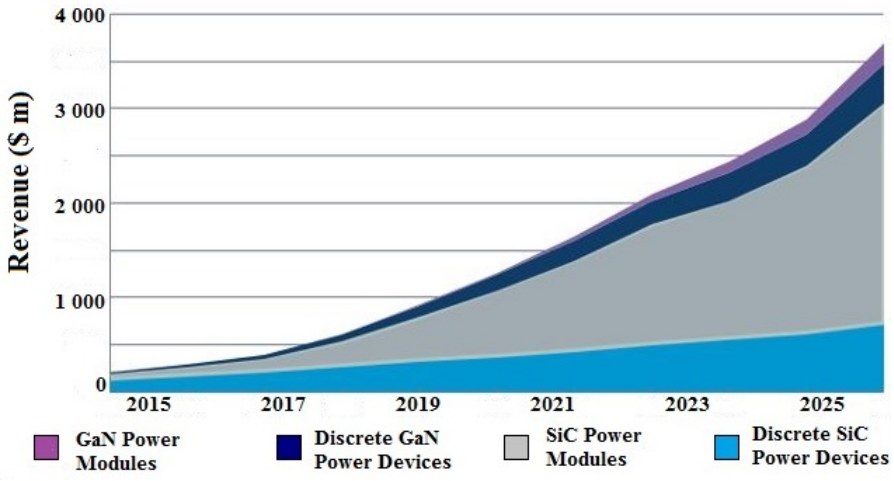

Figure 1.1: The global market for SiC and GaN power semiconductors is rising at a compound annual growth rate (CAGR) of around 33% from $210m in 2015 to about $1.265bn in 2020 then $3.7bn in 2025 [3].

end-user interviews done by Eden and Markides [3].

SiC is considered an excellent candidate for micro sensor and micro actuator applications in harsh environments due to its unique properties which include high hardness and wear resistance, high room temperature thermal conductivity (500 W m^{-1} K^{-1}) and chemical inertness [4]. Many of these applications, as well as the growth of the material itself, are critically dependent on the structural and electronic properties of surfaces and interfaces [5]. SiC is a unique wide band gap (IV-IV) compound semiconductor that forms a bridge between the elemental group-IV semiconductor materials (Si and Ge) and the III-V's (GaN, GaAs, etc) [6]. The average number of electrons per atom is, however, greater than that of group V and III-V. Epitaxially grown single and polycrystalline SiC layers on Si or silicon-on-insulator (SOI) wafers have enabled the realization of cost-effective SiC MEMS devices [7]. This has stimulated research on SiC thin film deposition and characterization. The mechanical properties of thin films are greatly dependent on the substrate and residual stress caused during deposition, hence, the properties of thin films can be tuned by growth conditions based on the Thornton model and the substrate mechanical and thermal properties [8]. Amorphous SiC (a-SiC) thin films are potentially strong contenders for MEMS application due to the preservation of many desirable properties where low deposition temperature is necessary [5]. Furthermore, their piezoelectric properties enable their applications be extended to multiferroics applications. Quite a number of a-SiC thin films on silicon have been studied [9]. However, there is no research that has been published on the properties of a-SiC thin film deposited on glass and sapphire substrates. In this work the mechanical properties of a-SiC will be carried out to provide suitable guidelines for MEMS and Nano Electro Mechanical Systems (NEMS) applications

in normal and hostile environments.

Most of the work presented in this dissertation is on SiC, a study on SrF_2 is given in chapter four.

1.1 Brief background

Silicon carbide, also known as carborundum, is a semiconductor material containing silicon and carbon, each atom is bonded to four atoms of the opposite type in a tetrahedral half-filled bonding configuration. SiC crystallizes in about 250 forms (polytypes). There are three possible arrangements of atoms in a layer of SiC crystal known as the A, B and C positions, and each polytype has a different stacking sequence of these layers [10]. The most commonly encountered polymorphs are the alpha (α) (4H-SiC, 6H-SiC) and the beta (β) (3C-SiC) which have a hexagonal and zinc blende crystal structures, respectively. Figure 1.2 illustrates the arrangements of atomic layers in different polytypes.

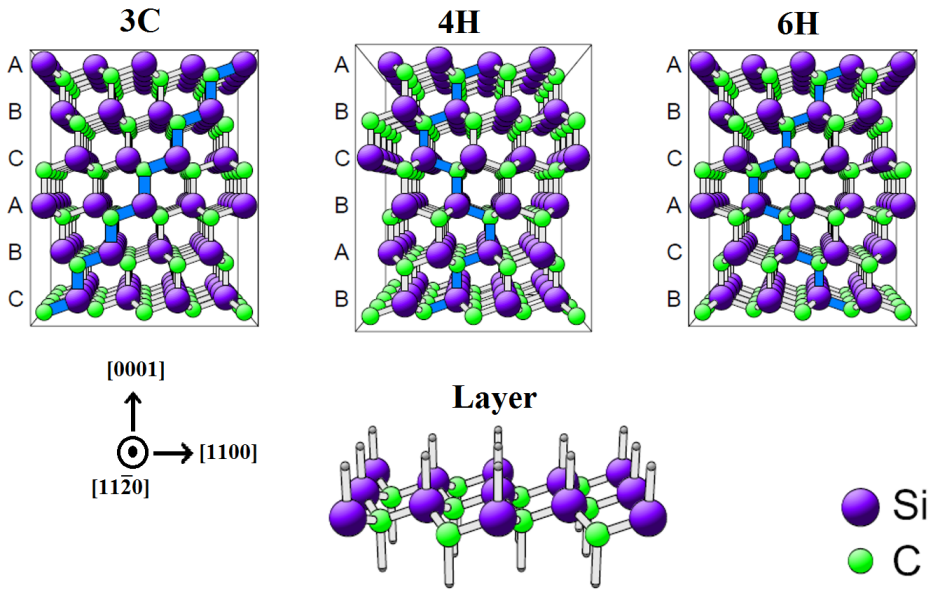

Figure 1.2: Different stacking scenarios of the silicon carbide atomic layer lead to different polymorph structures. Displayed are the 3C, 4H and 6H structures, the stacking direction is indicated by the blue bonding sticks [10].

Silicon carbide occurs naturally as the extremely rare mineral moissanite. It has, however, been mass produced in the powder form for use as an abrasive since 1893. Recent technologies have allowed growth of high quality SiC and this has broadened its applications significantly. SiC has long been recognized as a semiconductor with outstanding physical and chemical characteristics compared to its silicon (Si) counter part. The excellent properties include

- larger band gap (2.3 - 3.4 eV),
- higher breakdown field (30×10^5 V/cm),
- higher thermal conductivity (320 - 500 W/m·K),
- and a high saturation velocity (2×10^7 cm/s) than Si [4].

Thus enabling SiC to be a promising material for electron devices that function in radiation hard and harsh environments. Additionally it also exhibits superior mechanical properties, particularly hardness and wear resistance compared to its semiconductor counterparts. In terms of hardness, SiC has a Knoop hardness of 2480 kg/mm^2, which compares favorably with values for other hard materials such as diamond (7000 kg/mm^2) and aluminum oxide (2100 kg/mm^2), and greatly exceeds that of Si (850 kg/mm^2) [11]. SiC has a wear resistance value of 9.15, as compared with 10 for diamond and 9.00 for aluminum oxide [12]. Moreover, SiC has a high Young's modulus (700 GPa), which is about 3.5 times greater than the Young's modulus of Si (190 GPa) [11]. More SiC and Si properties are stated in table 1.1. These single crystal SiC properties are expected to be insignificantly different from the a-SiC properties, hence, motivating the study of a-SiC due to its relatively easy ways of fabrication.

Table 1.1: Table of electrical and physical properties of Si and SiC extracted from Ong et al. [13].

Properties	**Si**	**4H-SiC**	**6H-SiC**
Bandgap (eV)	1.10	3.30	3.00
Critical Field (MV/cm)	0.25	2.20	2.50
Electron saturation velocity (10^7 V/cm)	1.00	2.00	2.00
Electron mobility (cm^2/V·s)	1350	947	380
Hole mobility (cm^2/V·s)	480	120	80
Dielectric constant	11.80	9.70	9.70
Thermal conductivity (W/cm·K)	1.50	5.00	5.00
Melting point (^{o}C)	1420	2830	2830

1.2 Problem statement

SiC has by far proven to be of interest in MEMS industry [14, 9]. Previous research has dwelled much on the properties of SiC thin films on silicon or silicon-on-insulator (SOI) substrates. However, due to the difficult micro machining process and high density of defects when dealing with the SiC or sapphire substrate [15], no publication has been made on the elastic properties of a-SiC thin film on sapphire

substrate. This study will investigate the elastic constants of a-SiC on Si and sapphire substrates requisite for layered SiC based devices such as in MEMS.

1.2.1 Significance of the study

It has been proven experimentally that substrate hardness affects the measured film hardness for the case of a hard film on a soft substrate [16]. Saha and Nix [16] also confirmed that it is difficult to estimate the true hardness or elastic modulus of a film when there is a large elastic mismatch between the film and substrate. Relying on these results, it is believed that this research project will give accurate elastic constants of a-SiC thin film because there is not much elastic mismatch between a-SiC (film) and Sapphire (substrate) with Young's moduli of 410 GPa and 370 GPa respectively. Furthermore, the correlation between elastic properties and residual stress could provide useful information on the development of MEMS with high sensitivity and response.

1.3 Study objectives

Following the problem statement discussed in section 1.2 the objectives of this study are:

- Determination of the dynamics of bulk acoustic excitation and subsequently the elastic constants of cubic SrF_2.
- Synthesis and optimization of a-SiC thin films on <001> silicon and <0001> sapphire substrates,
- Determination of the structural and morphological properties of the a-SiC thin film and relate these to the measured elasticity,
- Determination of the elastic constants of a-SiC thin film on respective substrates and establish the effects of film/substrate combination on the a-SiC film elasticity,

1.4 Dissertation outline

This research project will focus on the analysis of Surface Brillouin Scattering (SBS) of as-deposited SiC thin films synthesized by radio-frequency magnetron sputtering. Based on the SBS results, acoustic velocities in thin films can be

obtained and the dependency of these velocities on substrate and on film thickness will be established. The elastic properties will then be extracted from the calculated phase velocities of the acoustic excitations.

The present chapter provides an introduction on the significance of the materials investigated. This includes a brief background of SiC, the problem statement and research objectives. In chapter two, the fundamental concepts of elasticity, acoustic wave propagation and surface Brillouin scattering mechanisms both in transparent bulk materials and transparent supported thin film are given. A detailed description of the thin film synthesis method and experimental techniques used in this study are given in chapter three.

Chapter four demonstrates the application of Brillouin scattering on transparent bulk samples (SrF_2). Elastic constants of strontium fluoride (SrF_2) are studied and compared with values found in literature. X-ray diffraction, Raman scattering and energy-dispersive X-ray spectroscopy (EDS) were used to characterize the SrF_2 sample. This chapter provides the basis for mode identification in transparent films deposited on transparent substrates. A typical example is the case of a-SiC thin films on sapphire.

Chapter five presents the characterization results of deposited thin films from Raman spectroscopy, Rutherford backscattering spectroscopy (RBS), grazing incidence X-Ray diffraction (GIXRD), X-Ray Reflectometry (XRR) and SEM. Chapter six presents the Brillouin scattering results obtained from a-SiC thin films. Finally, chapter seven gives the conclusions and suggestions for future work.

Chapter 2

Theoretical principles

2.1 Introduction

Spectroscopy deals with the interactions of radiation with matter. Incident radiations are usually in the form of, but not limited to, electromagnetic radiation [17], they can also be in the form of electrons, acoustic waves and beams of particles [18]. Isaac Newton is regarded as the founder of spectroscopy following his publications in the seventeenth century [19]. However, the Romans were already acquainted with the ability of a prism to generate a rainbow of colors [20].

The current study is mainly concerned with the interaction of electromagnetic waves in the visible range of the electromagnetic spectrum with the acoustic waves propagating in transparent materials. This chapter introduces the relationship between elasticity and acoustic waves. Brillouin scattering is discussed as a tool to investigate elastic constants. Also included in this chapter, is a discussion on thin film deposition.

2.1.1 Elastic properties of solid materials

A solid body may deform when subjected to stress. Provided the stress is below a threshold value, the elastic limit, the strain is reversible when the stress is withdrawn. Elasticity is basically the ability of a solid to retain its original form after an applied external force has been subsequently removed. Elasticity is conveniently described by stress and strain tensors. These are respectively concerned with the forces and with the continuous and periodic displacements of atoms from their equilibrium positions resulting to vibrations and waves. These waves form the basis of the analytical technique used in this study. Given an origin O, any point of the solid is located by the components x_1, x_2, x_3 of the vector $\boldsymbol{r}$. When

deformation occurs, the point moves to a new position $\boldsymbol{r}^{'}$ and the displacement is

$$u = \boldsymbol{r}^{'} - \boldsymbol{r} \tag{2.1}$$

In general when a solid deforms, the distance between any two points in the solid will change. Initially, prior to deformation, the distance between any two close neighboring points is denoted by dx, having components dx_i. After deformation, the distance becomes $dx^{'}$, with components $dx_i^{'}$, since

$$dx^{'} = dx + du, \quad \text{with} \quad du = \left(\frac{\partial u}{\partial x_i}\right) dx_i \tag{2.2}$$

The square of the distances between the two points is

$$(dx^{'})^2 = (dx)^2 + 2\epsilon_{ij}\ dx_i dx_j, \tag{2.3}$$

where ϵ_{ij} is given by

$$\epsilon_{ij} = \frac{1}{2}\left[\frac{\partial u_i}{\partial x_j} + \frac{\partial u_j}{\partial dx_i} + \left(\frac{\partial u_i}{\partial x_j}\right)\left(\frac{\partial u_j}{\partial x_i}\right)\right] \tag{2.4}$$

In the case of linear elasticity the stress and strain tensors are related by Hooke's law which states that stress is proportional to strain in the form

$$\sigma_{ij} = c_{ijkl}\epsilon_{kl}, \qquad i, j, k, l = 1, 2, 3... \tag{2.5}$$

where σ_{ij} is the Cauchy's stress second rank tensor, c_{ijkl} is the elastic constant tensor and it is a fourth rank tensor. ϵ_{kl} is a second rank tensor also known as the Cauchy's strain. In usual cases, the deformations in a solid are infinitesimal. The third term in equation (2.4) is negligible, hence, the tensor ϵ_{ij} reduces to

$$\epsilon_{kl} \approx \epsilon_{ij} = \frac{1}{2}\left[\left(\frac{\partial u_i}{\partial x_j}\right) + \left(\frac{\partial u_j}{\partial x_i}\right)\right], \tag{2.6}$$

where u_i and x_i are the components of the displacement vector and the position vector of a point in the material respectively. Equation (2.5) is preferentially expressed in matrix notation whose components/elements are dependent on the symmetry of the Bravais lattice. The elastic constant matrix is symmetric ($\sigma_{ij} = \sigma_{ji}$) and therefore has 21 independent components. Symmetric tensor means that the off-diagonal components are equal. As a result of the symmetry of the stress tensor and the strain tensor, only six state variables need to be evaluated [21]. The three components with the same subscripts, namely, ϵ_{11}, ϵ_{22}, ϵ_{33} define normal strain, representing change per unit length in the three direction specified by x_1, x_2, x_3 axes. The other three components, ϵ_{ij} (i $\neq$ j), define shear strain. Often,

it is convenient to introduce one index symbols (Voigt notation) for the strain components as shown in the Table 2.1. The stress tensor in equation (2.5), like

Table 2.1: Definition of one index symbols for the strain components

ϵ_1	ϵ_2	ϵ_3	ϵ_4	ϵ_5	ϵ_6
ϵ_{11}	ϵ_{22}	ϵ_{33}	ϵ_{23}	ϵ_{31}	ϵ_{12}

the strain tensor, has only six independent components. The three components σ_{ii} are referred to as normal stresses, while the other three σ_{ij} form the shear stresses. Using Voigt notation symbol the stress components can be represented as shown in Table 2.2.

Table 2.2: Definition of one index symbols for the stress components

σ_1	σ_2	σ_3	σ_4	σ_5	σ_6
σ_{11}	σ_{22}	σ_{33}	σ_{23}	σ_{31}	σ_{12}

Using the Voigt notation $c_{ijkl} = c_{\alpha\beta}$, that is $ij = \alpha = 1, 2, 3, ...$ and $kl = \beta = 1, 2, 3, ...$ Equation (2.5) may then be rewritten as,

$$\begin{bmatrix} \sigma_1 \\ \sigma_2 \\ \sigma_3 \\ \sigma_4 \\ \sigma_5 \\ \sigma_6 \end{bmatrix} = \begin{bmatrix} c_{11} & c_{12} & c_{13} & c_{14} & c_{15} & c_{16} \\ c_{21} & c_{22} & c_{23} & c_{24} & c_{25} & c_{26} \\ c_{31} & c_{32} & c_{33} & c_{34} & c_{35} & c_{36} \\ c_{41} & c_{42} & c_{43} & c_{44} & c_{45} & c_{46} \\ c_{51} & c_{52} & c_{53} & c_{54} & c_{55} & c_{56} \\ c_{61} & c_{62} & c_{63} & c_{64} & c_{65} & c_{66} \end{bmatrix} \begin{bmatrix} \epsilon_1 \\ \epsilon_2 \\ \epsilon_3 \\ \epsilon_4 \\ \epsilon_5 \\ \epsilon_6 \end{bmatrix}. \tag{2.7}$$

In general, single-crystal elasticity is not isotropic. The number of independent material parameters depends on the level of symmetry of the crystal structure. In hexagonal crystal structures, six independent parameters are needed for a complete description of the constitutive behavior,

$$\begin{bmatrix} \sigma_1 \\ \sigma_2 \\ \sigma_3 \\ \sigma_4 \\ \sigma_5 \\ \sigma_6 \end{bmatrix} = \begin{bmatrix} c_{11} & c_{12} & c_{13} & 0 & 0 & 0 \\ c_{12} & c_{11} & c_{13} & 0 & 0 & 0 \\ c_{13} & c_{13} & c_{33} & 0 & 0 & 0 \\ 0 & 0 & 0 & c_{44} & 0 & 0 \\ 0 & 0 & 0 & 0 & c_{44} & 0 \\ 0 & 0 & 0 & 0 & 0 & c_{66} \end{bmatrix} \begin{bmatrix} \epsilon_1 \\ \epsilon_2 \\ \epsilon_3 \\ \epsilon_4 \\ \epsilon_5 \\ \epsilon_6 \end{bmatrix}. \tag{2.8}$$

For a cubic crystal, as is the case with SrF_2 studied in this work, equation (2.7)

can be written in terms of three independent material parameters as

$$\begin{bmatrix}\sigma_1\\ \sigma_2\\ \sigma_3\\ \sigma_4\\ \sigma_5\\ \sigma_6\end{bmatrix} = \begin{bmatrix} c_{11} & c_{12} & c_{12} & 0 & 0 & 0\\ c_{12} & c_{11} & c_{12} & 0 & 0 & 0\\ c_{12} & c_{12} & c_{11} & 0 & 0 & 0\\ 0 & 0 & 0 & c_{44} & 0 & 0\\ 0 & 0 & 0 & 0 & c_{44} & 0\\ 0 & 0 & 0 & 0 & 0 & c_{44}\end{bmatrix} \begin{bmatrix}\epsilon_1\\ \epsilon_2\\ \epsilon_3\\ \epsilon_4\\ \epsilon_5\\ \epsilon_6\end{bmatrix}, \tag{2.9}$$

[22]. A solid is elastically isotropic if its elastic behavior is independent of orientation. This may not only occur if its crystal structure is elastically isotropic, but also if it consists of a collection of anisotropic crystals arranged at random. Most materials are polycrystalline, in which the crystallites are very small and randomly oriented, hence, have isotropic elastic properties. Amorphous materials (which we will be dwelling most in in this work) are also elastically isotropic materials. Only two independent elastic constants for isotropic materials exist and are characterized by c_{11} and c_{44} in the relation,

$$c_{12} = c_{11} - 2c_{44}. \tag{2.10}$$

Isotropy for hexagonal systems exhibit hexagonal symmetry, in which transverse anisotropy leads to five independent elastic constants, namely, c_{11}, c_{12}, c_{13}, c_{33} and c_{44}. The engineering constants in equation 2.10 are best represented by Lamé coefficients, λ and μ, such that,

$$\begin{aligned}\lambda &= c_{12};\\ \mu &= c_{44};\\ 2\mu + \lambda &= c_{11}.\end{aligned} \tag{2.11}$$

The behavior of isotropic linear elastic materials can be described by a set of two independent parameters, that is, Poisson's ratio υ and Young's modulus E. Young's modulus E, is defined as the tensile stress divided by the longitudinal strain for a rod, that is,

$$E = \frac{\mu\big(3\lambda + 2\mu\big)}{\big(\lambda + \mu\big)} = \frac{c_{44}\big(3c_{12} + 2c_{44}\big)}{\big(c_{12} + c_{44}\big)} \tag{2.12}$$

Poisson's ratio Υ, is the negative of the ratio of the transverse strain to the longitudinal strain for a rod and is given by

$$\Upsilon = \frac{\lambda}{2\big(\lambda + \mu\big)} = \frac{c_{12}}{2\big(c_{12} + c_{44}\big)} \tag{2.13}$$

In terms of these parameters, the elasticity matrix c for isotropic materials is given by

$$c = \frac{E}{(1+\Upsilon)(1-2\Upsilon)} \begin{bmatrix} 1-\Upsilon & \Upsilon & \Upsilon & 0 & 0 & 0 \\ \Upsilon & 1-\Upsilon & \Upsilon & 0 & 0 & 0 \\ \Upsilon & \Upsilon & 1-\Upsilon & 0 & 0 & 0 \\ 0 & 0 & 0 & \frac{1}{2}(1-2\Upsilon) & 0 & 0 \\ 0 & 0 & 0 & 0 & \frac{1}{2}(1-2\Upsilon) & 0 \\ 0 & 0 & 0 & 0 & 0 & \frac{1}{2}(1-2\Upsilon) \end{bmatrix}. \tag{2.14}$$

Isotropic linear elastic behavior can also be characterized by the shear modulus G combined with the bulk modulus K. Shear modulus G, is the applied shear stress divided by the resulting shear strain, therefore

$$G = \mu = c_{44}. \tag{2.15}$$

The bulk modulus K, is defined as the negative of the ratio of pressure to the relative change in the volume and its given by

$$K = \frac{(3\lambda + 2\mu)}{3} = \frac{(3c_{12} + 2c_{44})}{3} \tag{2.16}$$

The four engineering constants G, K, E and Υ, stated above are related by

$$\begin{aligned} G &= \frac{E}{2(1+\Upsilon)}; \\ K &= \frac{E}{3(1-2\Upsilon)}. \end{aligned} \tag{2.17}$$

2.1.2 Elastic wave propagation

The equation of motion for a continuum body, in the absence of unbalanced external forces, is given by

$$\rho\left(\frac{\partial^2 u_i}{\partial t^2}\right) = \left(\frac{\partial \sigma_{ij}}{\partial x_j}\right), \qquad i,j = 1,2,3 \tag{2.18}$$

where ρ is the density of the medium and u_i as defined earlier, is a component of the displacement vector. The first suffix in the stress tensor σ_{ij} denotes the direction in which the force acts and the second the direction of the outward normal to the surface on which the force acts. Substituting equations (2.5) and (2.6) into equation (2.18), the equation of motion using Einstein's notation for

tensor addition assumes the form

$$\rho\left(\frac{\partial^2 u_i}{\partial t^2}\right) = c_{ijkl}\left(\frac{\partial^2 u_l}{\partial x_j \partial x_k}\right). \tag{2.19}$$

Assuming a plane wave propagating in the direction n with components n_i, the displacement is

$$u_i = a_i e^{(n_j x_j - vt)} \tag{2.20}$$

where a_i is a component of the amplitude of the particle, x_j is a component of the particle position, v is the speed of the wave propagation, and t is time. Substituting equation (2.20) into equation (2.19) gives

$$a_k c_{ijkl}\, n_j n_l = \rho v^2 a_i \tag{2.21}$$

Introducing the notation

$$\Gamma_{ik} = c_{ijkl} n_j n_l \tag{2.22}$$

where Γ_{ik} is a component of the matrix known as the Kelvin-Christoffel stiffness matrix. Equation (2.21) can then be easily written as

$$\Gamma_{ik} a_k = \rho v^2 a_i \tag{2.23}$$

If for a tensor L_{ij}, for example, there is a relationship $L_{ij} m_j = \lambda m_i$, then m_i is a component of an eigenvector of the tensor and λ is the corresponding eigenvalue. Thus, a_i is a component of an eigenvector of Γ_{ik} and ρv^2 is the corresponding eigenvalue. Γ_{ik} is a real symmetric matrix, hence, for a wave propagating in any direction in a general anisotropic material there are three modes (longitudinal (L), slow transverse (ST) and fast transverse (FT) modes) of propagation, each with a different velocity and a different direction of particle displacement. The directions of particle displacement for the three modes are given by the eigenvectors of Γ_{ik} and are orthogonal. The velocities of the three modes are related to the eigenvalues, λ_j, of Γ_{ik} through the equation

$$v_j = \sqrt{\left(\frac{\lambda_j}{\rho}\right)} \tag{2.24}$$

For the propagations along symmetry directions, the cubic equation factorizes and simple linear or quadratic equations are obtained for the respective velocities. Table 2.3 lists the solutions for the case of a medium of cubic symmetry and Table 2.4 lists the solutions for the case of a medium of hexagonal symmetry.

Table 2.3: Solutions of Christoffel's equation for cubic symmetry, [23]

Propagation direction n	**Polarization direction** u	**Wave Mode**	**Velocity equation** $\rho v^2 =$
$[100]$	$[100]$	L	c_{11}
$[100]$	$[010]$, $[001]$	$T(2)$	c_{44}
$[110]$	$[001]$	T	c_{44}
$[110]$	$[1\bar{1}0]$	T	$\frac{1}{2}(c_{11}-c_{12})$
$[110]$	$[110]$	L	$\frac{1}{2}(c_{11}+c_{12}+2c_{44})$
$[111]$	$[1\bar{1}0]$, $[11\bar{2}]$	$T(2)$	$\frac{1}{3}(c_{11}-c_{12}+2c_{44})$
$[111]$	$[111]$	L	$\frac{1}{3}(c_{11}+2c_{12}+4c_{44})$
$[\cos\theta, \sin\theta, 0]$	$[001]$	T	c_{44}
$[\cos\theta, \sin\theta, 0]$	(001) plane	qL, qT	$\frac{1}{2}\{B \pm \sqrt{B^2-4C}\}$

In Table 2.3;
$B = c_{44} + c_{11}$ and
$C = \left(c_{11}\cos^2\theta + c_{44}\sin^2\theta\right)\left(c_{44}\cos^2\theta + c_{11}\sin^2\theta\right) - \left(c_{12}+c_{44}\right)^2\cos^2\theta\sin^2\theta.$

Table 2.4: Solutions of Christoffel's equation for hexagonal symmetry (transverse isotropy) [23].

Propagation direction n	**Polarization direction** u	**Wave Mode**	**Velocity equation** $\rho v^2 =$
x_1x_2 plane	$[001]$	T	c_{44}
x_1x_2 plane	$[001] \times n$	T	c_{66}
x_1x_2 plane	n	L	c_{11}
$[001]$	$[001]$	L	c_{33}
$[001]$	$[100]$, $[010]$	$T(2)$	c_{44}
$[0, \sin\theta, \cos\theta]$	$[100]$	T	A
$[0, \sin\theta, \cos\theta]$	(100) plane	qL, qT	$\frac{1}{2}\{B \pm \sqrt{C^2+D^2}\}$

In Table 2.4;
$A = c_{66}\sin^2\theta + c_{44}\cos^2\theta$,
$B = c_{44} + c_{11}\sin^2\theta + c_{33}\cos^2\theta$,
$C = (c_{44} - c_{11})\sin^2\theta + (c_{33} - c_{44})\cos^2\theta$,
$D = (c_{13} + c_{44})\sin 2\theta$,
$c_{66} = c' = \dfrac{1}{2}(c_{11} - c_{12})$.
Given the discussion above, if the stiffness matrix for a material is known, it is possible to determine the components of the Kelvin-Christoffel stiffness matrix for any direction n with components n_i. Using the obtained Kelvin-Christoffel stiffness matrix for a particular direction, it is possible to determine the velocities and particle displacements for the three modes of wave propagation in that direction. The components of the Kelvin-Christoffel stiffness matrix in terms of the components of the stiffness matrix, c_{ij} are discussed in detail by Van Buskirk et al. [24].

2.2 Brillouin scattering spectroscopy

In this dissertation, Brillouin scattering was used to investigate the elastic properties of transparent bulk cubic crystals and transparent thin supported amorphous films. Brillouin scattering is the inelastic scattering of photons by thermally excited acoustic phonons in materials, whose wave vector, selected by the kinematics of scattering lies near the center of the Brillouin zone [25]. This phenomenon was first investigated by Brillouin [26] and has acquired huge interest for probing elastic and optoelastic properties of transparent materials since the emergence of the laser as a powerful source of monochromatic light [27].

Brillouin scattering is usually compared to X-ray diffraction from crystals, because of the formal analogy between the conditions of interference (Bragg relation) [28]. The inelastic scattering of X-rays by electrons is the same phenomenon as Brillouin scattering, the only difference is that the selective reflection of the incident electromagnetic wave is on lattice plane in the case of X-ray diffraction and on planes of maximum atomic density in the case of Brillouin scattering [28]. In Brillouin scattering, a frequency shift due to Doppler effect is observed as a result of the planes in motion. These frequency shifts were experimentally observed by Gross [29] and later confirmed by Meyer [30]. The Brillouin scattering technique is a contact-less probing method and measurements can be made on very small specimen (one millimeter on edge). Measurements may also be made on ambient and at high temperatures [31, 32]. Reviews have been made in the past to discuss how the technique is used to study elastic properties of crystals and different types of phase transitions [33–37]

The frequency shifts, also known as Brillouin shifts, in the Brillouin scattering process are in the GHz range. To achieve high resolution for such shifts, Tandem Fabry-Pérot interferometer (TFPI) is used as a scanning spectrometer [38]. The TFPI used in this work will be discussed in chapter three.

2.2.1 Brillouin scattering mechanisms

As defined in the last section, Brillouin scattering is the inelastic scattering of light by acoustic phonons in materials. This interaction enables the study of surface and bulk acoustic waves. In the simplest case of an isotropic solid, there exist one true surface wave excitation, namely the Rayleigh wave (RW), while the three bulk acoustic waves have pure longitudinal or transverse polarization, with equal sound velocities for the transverse waves [39].

There are two distinct mechanisms in which acoustic waves can scatter light, in fact, the light can exchange momentum and energy with the phonon field through the dynamical corrugation of the surface(ripple effect) and the modulation of the

dielectric tensor of the medium (elasto-optic effect). Experiments and calculations have been made in the last century which clarified the conditions under which each scattering mechanism dominates [40–42, 39, 43].

Elasto-optic mechanism (Bulk scattering)

In elasto-optic mechanism, the dynamic fluctuations in the strain field bring about fluctuations in the dielectric constant thus introducing fluctuations in the refractive index. These fluctuations result in inelastic scattering of the light as it passes through the material. The movement of phonons within a material is in thermal equilibrium with small amplitudes creating fluctuations in the dielectric constant, and this is interpreted as a moving diffraction grating by an incident light wave. In a transparent solid, most of the scattered light originate from the refracted beam in a region away from the surface, and the kinematic conditions relating wave vector k and frequency shift $(\Delta\omega, \omega)$ of the light pertain to bulk acoustic wave scattering. In figure 2.1 the green and blue arrows demonstrate the incident (k_i)

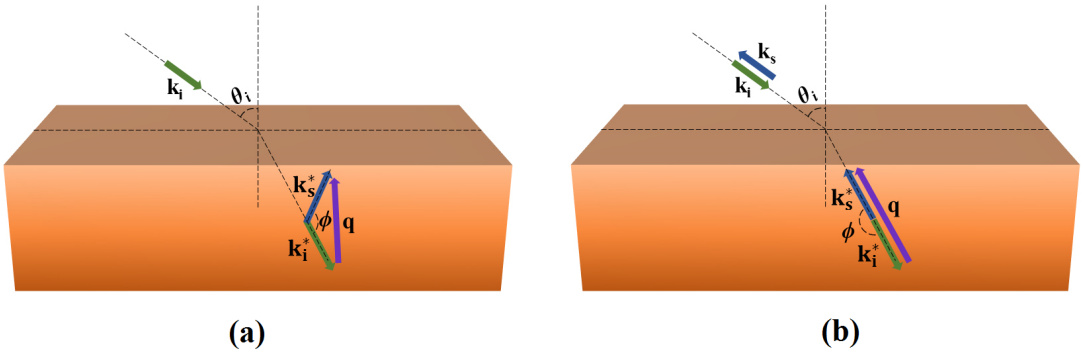

Figure 2.1: (a) General schematic of light scattering from bulk phonons. (b) Schematic of the light scattering from bulk phonons in the backscattering configuration.

and scattered (k_s) wave vectors respectively. The acoustic phonon wave vector q is indicated by the purple arrow. ϕ is the scattering angle and θ_i is the incident light angle measured to the normal of the sample surface. The magnitude of wave vector k_i passing through a medium of refractive index n is

$$k_i = \frac{2\pi n}{\lambda_i} = \frac{n\omega_i}{c}, \tag{2.25}$$

where ω_i is the angular frequency of the incident light ray, λ_i is the wavelength, and c is the velocity of light in vacuum. A fluctuation in the dielectric constant associated with an acoustic mode of wave vector q and angular frequency,

$$\omega = vq, \tag{2.26}$$

where v is the acoustic velocity, will result in a small part of the incident light being inelastically scattered with wave vector

$$k_s = k_i \pm q \implies q = \pm(k_i - k_s), \tag{2.27}$$

and angular frequency

$$\omega_s = \omega_i \pm \omega. \tag{2.28}$$

The phonons, satisfying the wave vector conservation in a given Brillouin scattering geometry, e.g. Figure 2.1, in a cubic and hence optically isotropic material, have wave vectors given by equation (2.27) and

$$|q| = \pm 2|k_i|\sin\theta. \tag{2.29}$$

The vibrational frequency is much smaller relative to the optical frequency by a factor of order $v/c \approx 10^{-5}$, so ω_i and ω_s differ only very slightly, k_s and k_i are approximately equal in magnitude. Figure 2.1 (a) leads to

$$q = 2k_i sin(\frac{\phi}{2}) = \frac{4\pi n}{\lambda_i} sin(\frac{\phi}{2}). \tag{2.30}$$

With respect to equation (2.26) and (2.30) the acoustic phase velocity can be written as

$$v = \frac{\Delta\omega\lambda_i}{4\pi n\ sin(\frac{\phi}{2})}, \tag{2.31}$$

$\Delta\omega$ is the frequency shift. In these equations, ϕ is the scattering angle (Figure 2.1 (a)). In the present work backscattering geometry (Figure 2.1 (b)) is used. In backscattering ϕ is 180° and therefore, the phonon wave vector is given by

$$q = \frac{4\pi n}{\lambda_i}. \tag{2.32}$$

Equation (2.32) shows that in the backscattering configuration, the phonon wave vector is only dependent on the refractive index of scattering medium (n) and the excitation wave length of probing laser (λ_i) assuming that the scattering surface is specularly smooth.

Surface ripple mechanism (Surface scattering)

In opaque thin films and bulk materials, the ripples produced by Brownian motion of atoms can scatter incident laser light, hence, the name surface Brillouin scattering (SBS). In investigating materials with high absorption coefficient and thin films, ripple scattering is the dominant scattering mechanism. Thus, the phonon

wave vector is conserved in the direction parallel to the surface of the sample, Figure 2.2 illustrates. Momentum and energy conservation dictates that the wave vector $q_{\parallel}$ and velocity V of the surface wave must satisfy these equations;

$$q_{\parallel} = 2k_i \sin\theta_i \tag{2.33}$$

$$V = \frac{\Delta\omega}{q_{\parallel}} \tag{2.34}$$

k_i and $\Delta\omega = \pm(\omega_i - \omega_s)$ are the incident wave vector and the change in the

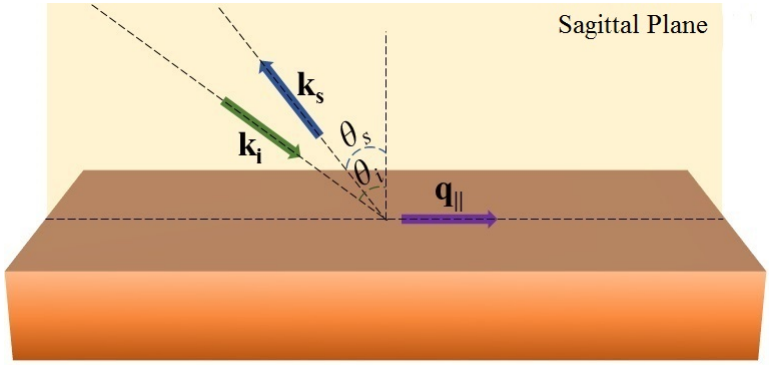

Figure 2.2: General schematic of light scattering from surface phonons.

angular frequency of the scattered light. The phonon wave vector, $q_{\parallel}$, is parallel to the surface of the sample at the intersection of the scattering plane and the sample surface. Unlike scattering from bulk phonons, the wave-vector of the surface phonons, $q_{\parallel}$, is dependent on the incident and scattered light angles denoted by θ_i and θ_s, respectively. In the backscattering geometry, $\theta_i \approx \theta_s$, therefore, the phonon wave vector is

$$q_{\parallel} = \frac{4\pi \sin\theta_i}{\lambda_i}, \tag{2.35}$$

thus, $q_{\parallel}$ can be varied solely by changing the angle of incidence. In general, in ripple mechanism; phonon vibrations cause the surface to appear as a moving grating, that is, a ripple capable by itself of producing diffraction and changing the frequency of the incoming light (Doppler Effect) without invoking any modulation of the dielectric field in the interior of the crystal (Figure 2.2).

Surface Brillouin scattering (SBS) in semi-opaque solids

In semi-opaque materials, both bulk and surface Brillouin can be observed. The more transparent the solid, the greater the penetration of light into the medium. Thus the greater the proportion of bulk elasto-optically scattered light in the spectrum. As a consequence of attenuation of light in the medium, the incident

and scattered light wave vectors, k_i and k_s, are complex, hence, the scattered light is broadened in frequency. Figure 2.3 illustrates the combined surface and bulk Brillouin spectra for various values of the complex dielectric constant $\epsilon = \epsilon_1 + i\epsilon_2$ of a solid calculated by Mills and Subbaswamy [44]. The imaginary part of ϵ determines the attenuation. If ϵ_2 is very small (transparent media), as shown

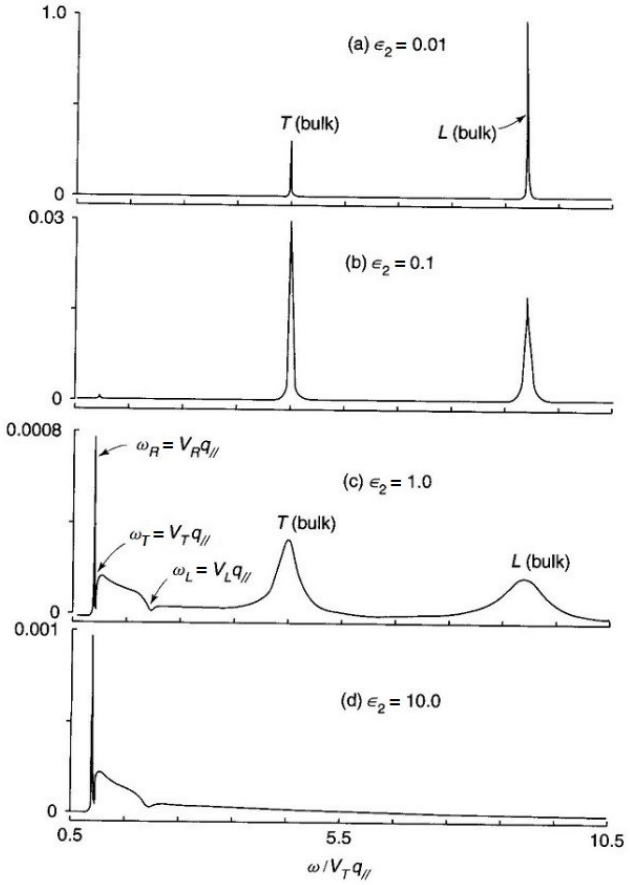

Figure 2.3: Computed combined surface and bulk Brillouin spectra for various values of the complex dielectric constant and $\epsilon = \epsilon_1 + i\epsilon_2$. From Mills and Subbaswamy [44].

in Figure 2.3(a), the bulk longitudinal (L) and transverse (T) scattering peaks are very sharp and there is no peak associated with SBS. As the value of the dielectric constant increases the bulk L and T peaks broaden and a trace of the Rayleigh surface acoustic peak appear. A larger value of the dielectric constant yield significantly more broadened bulk L and T peaks and a clearer SBS spectrum. The broadening in the bulk peaks is consistent with the uncertainty principle, i.e. an increasingly confined scattering region results in an increasing momentum spread. As shown in Figure 2.3(d), a very large value of ϵ_2 yields a clear SBS spectrum and no trace of bulk scattering. The Rayleigh surface acoustic wave (RSAW) becomes dominant (ripple scattering) and two dips at the frequencies ω_L and ω_T appear due to interference of bulk waves. Bulk acoustic waves incident on

the surface can also cause dynamic surface corrugations, and these will be detected if the component of their wave vector in the surface is equal to q. Combined with their normal component, the wave vectors of these bulk waves take on a continuum of values, and this gives rise to a broad continuum in the Brillouin spectrum extending from the bulk transverse wave threshold to high frequencies. This is known as the Lamb shoulder, and is the broad band to the right of the RSAW peak in 2.3. The Lamb shoulder results from a so-called 'mixture of modes', modes are mixtures between sinusoidally varying (transverse) and exponentially decaying (longitudinal) modes. Below the transverse threshold ω_T all amplitudes are decaying for z $\rightarrow -\infty$ and at ω_R the Rayleigh wave is localized at the surface. In this way, the RSAW propagates undamped along the surface and made up of a longitudinal and shear vertical wave with exponentially decaying amplitudes.

Experiments done in the past, including those by Riobóo et al. [45], demonstrate the ability of SBS to collect surface acoustic waves (SAW) data from transparent bulk samples and that way extends this non-destructive and contact-less method to a wider range of bulk materials.

2.2.2 Surface Brillouin scattering : Green's function

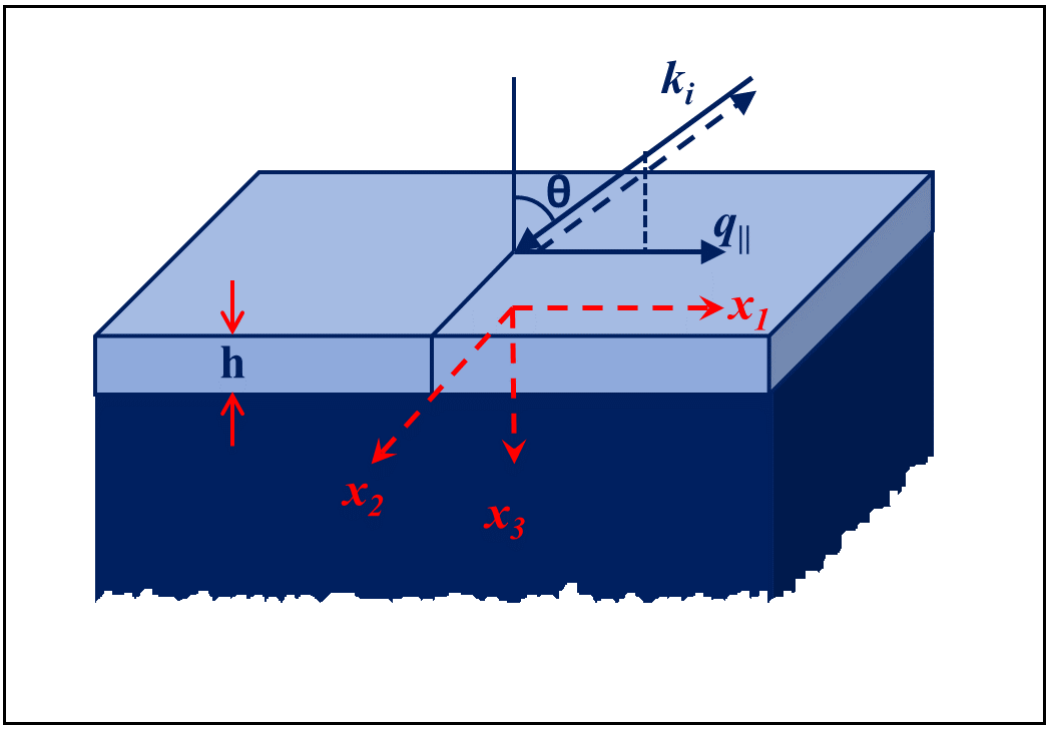

Figure 2.4: Brillouin scattering configuration and sample geometry. The x_1 and x_2 axes are parallel to the sample surface. The x_3 axis is normal to the sample surface and its origin is taken at the interface [46].

The theoretical interpretation of the SBS spectral intensity was performed

using the elastodynamic Green's function approach. For a layer perfectly bonded to its substrate as shown in Figure 2.4. $-x_3$ in Figure 2.4 is the outward normal to the surface and the origin is at the interface between the layer and the substrate. The layer, of thickness h, occupies the region $-h < x_3 < 0$

The cross section for the scattering of light by the ripple mechanism with angular frequency change ω and surface scattering wave vector $q_\parallel$ is proportional to the power spectrum of thermal fluctuations in the normal displacement of the surface profile [39, 47, 46, 48]. For sufficiently high temperature $T >> \hbar\omega/k_B$, where k_B is Boltzmann's constant and $\hbar$ is the Planck's constant, the scattering cross section is given by [46]

$$I(\omega) = D\frac{T}{\omega}\mathrm{Im}\Big\{G_{33}(q_\parallel, x_3 = -h, \omega + i0)\Big\} \tag{2.36}$$

where D is a constant that depends on the scattering geometry, frequency and polarization of the incident light and optical properties of the medium. G_{33} is the (x_3, x_3)component of the Fourier domain surface elastodynamic Green's function tensor $G_{ij}(x,t)$, evaluated at the outer surface $x_3 = -h$ of the layer/film. In a substrate and layer system for a given value of $q_\parallel$ and ω, the equations of motion admit six plane wave solutions. These partial waves pertain to different wave-vector components $k_3^{(n)}$ perpendicular to the free surface, which may be real or complex and are solutions of the sextic Christoffel equation. For the layer, all six phase matched plane waves (n = 1,2,...,6) are used; while for the substrate only the three outgoing plane waves (n = 7,8,9) are retained [49]. The outgoing waves are either homogeneous with $k_3^{(n)}$ real and having ray vectors $v = \partial\omega/\partial k$ directed into the interior of the substrate, or evanescent waves with $\mathrm{Im}(k_3^{(n)}) > 0$, so that their amplitudes fall off into the interior.The boundary conditions on the surface tractions and displacements provide nine equations for determining the partial wave amplitudes. The Green's function $G_{33}(q_\parallel, x_3 = -h, \omega)$ is obtained as the superposition of six partial waves in the layer;

$$G_{33}(q_\parallel, x_3 = -h, \omega) = \frac{i}{\omega}\sum_{n=1}^{6}(B^{-1})_3^{(n)}U_3^{(n)}\exp\{-ik_3^{(n)}d\}, \tag{2.37}$$

in which

$$B_l^{(n)} = \sum_{pq} c^-_{3lpq}U_p^{(n)}k_q^{(n)}\exp\{-ik_3^{(n)}d\}/\omega \qquad n = 1,2,...,6 \quad l = 1,2, \tag{2.38}$$

the boundary condition matrix is given by B. $U_3^{(n)}$ are the x_3 components of the polarization vectors. A detailed method of calculation of G_{33} is provided by Zhang

et al. [50].

Expressing the light scattering in terms of Green's function is just a convenient computational method, and hence, it should not be concluded from equation (2.36) that the incident light is causing the fluctuations, the light is only probing existing thermal fluctuations. Considering half space materials, the Brillouin scattering spectrum, consists of a sharp line associated with the true Rayleigh SAW and then at higher frequencies a continuum of excitations extending from a threshold, known as the transonic state, to higher frequencies. A true SAW arises when B^{-1} becomes singular. Some resonances can be observed within the frequency region of the Lamb shoulder, these are associated with pseudo surface acoustic waves (PSAW). In this study an open source program, written in FORTRAN (a programming language that is especially suited to numeric computation and scientific computing), was used for the calculation of SAWs in the analysis of SBS spectra [47].

2.3 Thin film deposition

Thin film deposition is the technology of coating a very thin film of material, in the nanometer range, onto a substrate. Thin film deposition is usually divided into two broad categories, chemical vapor deposition and physical vapor deposition coating systems. Chemical vapor deposition is when a volatile fluid precursor produces a chemical change on a surface leaving a chemically deposited coating. Physical vapor deposition (PVD) refers to a wide range of technologies where a material is released from a source and deposited on a substrate using mechanical, electromechanical or thermodynamic processes. The PVD processes include, pulsed laser deposition (PLD), molecular beam epitaxy (MBE), thermal evaporation and sputtering. Radio frequency (RF) magnetron sputtering was used to grow thin films using the concepts of the Thornton structure zone model shown in Figure 2.5 [8, 51]. The Thornton model has two governing factors; the amount of added energy (pressure) and homologous growth temperature (T/T_m), where T is the substrate temperature and T_m is the melting point of the film material. The sputtered material leaves the sputter source with relatively high energies (several electron volts) and more sputtering occurs as the sputtering pressure is increased. In this study, thin films were deposited at ambient substrate temperature, hence, according to the Thornton model, the films fall within Zone 1 structural properties. Zone 1 has a columnar structure consisting of tapered units defined by voided growth boundaries and occurs at very low homologous deposition temperature ($T/T_m < 0.3$) [8]. The RF magnetron sputtering technique was the deposition method of choice as a consequence of the following advantages:

- low deposition temperatures;
- produces better film quality and step coverage compared to evaporation;
- versatility in the deposition of wide variety of insulators, metals, alloys, composites etc;
- charge-up effects are avoided and arcing is reduced due to use of alternating current (AC) radio frequency (RF) source of frequency 13.56 MHz. This is due to the fact that electric field sign at every surface inside plasma chamber changes with RF;
- high film-substrate adhesion;
- relatively low operational costs (compared to Knudsen cell);
- ability to vary the deposition conditions, and
- allows control over film stoichiometry and microstructure [52, 53].

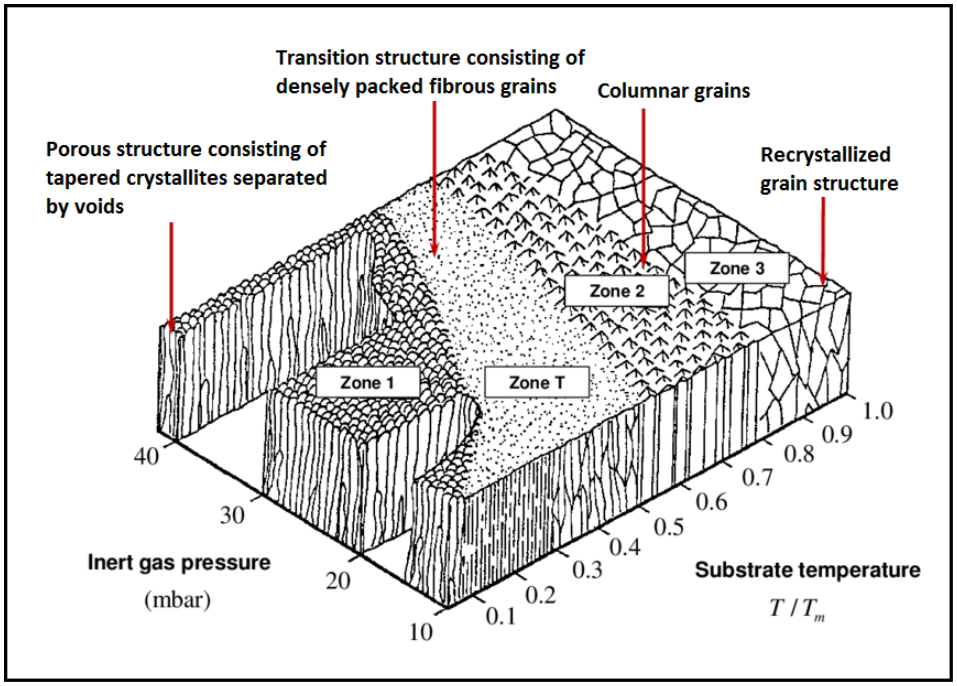

Figure 2.5: The Thornton structure zone model extracted from Thornton [8].

2.3.1 Radio Frequency (RF) magnetron sputtering

A number of books and articles have covered the topic of magnetron sputtering with great comprehensiveness. Amongst the most helpful ones are books by Kern [54], Wasa and Hayakawa [55], Bunshah and Blocher [56] and review articles by

Arnell and Kelly [51], Kelly and Arnell [57], Kouznetsov et al. [58] and Braun [59]. Sputtering involves the bombardment of a target material with high energy particles (Ar^+) that are to be deposited on a substrate. The collision results in a momentum transfer from Ar^+ through the knock-off effect to the target [60]. The ad atoms are then deposited as thin films on the substrate [61]. Secondary electrons are also emitted from the target surface as a result of the ion bombardment, and these electrons play an important role in maintaining the plasma.

Magnetrons make use of the fact that a magnetic field configured parallel to the target surface can constrain secondary electron motion to the vicinity of the target. The magnets are arranged in such a way that one pole is positioned at the central axis of the target and the second pole is formed by a ring of magnets around the outer edge of the target. Trapping the electrons in this way substantially increases the probability of an ionization through an enhanced electron-atom collisions occurring. The increased ionization efficiency of a magnetron results in a dense plasma in the target region. This, in turn, leads to increased ion bombardment of the target, giving higher sputtering rates and, therefore, higher deposition rates at the substrate. Moreover, the increased ionization efficiency achieved in the magnetron mode allows the discharge to be maintained at lower operating pressures (typically, 10^{-3} mbar, compared to 10^{-2} mbar) and lower operating voltages than is possible in the basic sputtering mode [51]. Schematic and pictorial representation of the RF magnetron sputtering technique will be presented in Chapter 3.

2.4 Summary

In this chapter the theoretical aspects of this work were discussed, namely, elastic waves, Brillouin scattering spectroscopy and thin film deposition. The relationship between elastic and acoustic waves used in Brillouin scattering spectroscopy was established. The advantages of using RF magnetron sputtering as a film deposition technique were stated. Chapter three gives experimental parameters used during film deposition and also highlights on the experimental techniques used to characterize deposited films.

Chapter 3

Experimental techniques

3.1 Introduction

This chapter presents the discussion on experimental techniques used to fabricate thin films (a-SiC) and establish the properties of transparent materials SrF_2 and a-SiC. These techniques include, radio frequency (RF) magnetron sputtering for fabrication of thin films, Raman spectroscopy for structural properties for both a-SiC and SrF_2, scanning electron microscopy (SEM) for imaging and energy dispersive x-ray spectroscopy (EDS) measurements (on a-SiC), x-ray reflectivity (XRR) for density and film thickness measurements, x-ray diffraction (a-SiC and SrF_2), grazing incident x-ray diffraction (GXRD) (on a-SiC), Rutherford backscattering (RBS)(on a-SiC), optical spectroscopy (on a-SiC) and finally surface Brillouin scattering (SBS)(on a-SiC and SrF_2). SBS is described with more depth relative to other techniques owing to it being the main technique in this study.

3.2 Radio-Frequency magnetron sputtering

Thin film synthesis was the first step prior to the determination of the elastic constants of the film. Section 2.3.1 presented the physical principles behind RF magnetron sputtering. The current section presents the apparatus (shown in Figure 3.1) that made upholding of physical principles in section 2.3.1 possible. A comprehensive overview of the technique has been covered by Kukla [62].

Figure 3.1 shows a pictorial representation of the RF magnetron sputtering setup used for SiC film deposition (located at the School of Physics, University of the Witwatersrand, Johannesburg). A stoichiometric SiC target material manufactured by Semiconductor Wafer. Inc. with a diameter of 76 mm, thickness 6 mm and 99.9% purity was used. Before deposition, the substrates were cleaned using detergent and water, rinsed with acetone in an ultrasonic bath for five minutes and

then blow dried with ultra-pure nitrogen gas (5N). The target and substrate are mounted in the deposition chamber at a fixed separation of 60 mm. The chamber is initially evacuated using a rotary oil pump to a vacuum pressure of the order 10^{-2} mbar. An optimum vacuum pressure of the order 10^{-5} mbar is then attained using a turbo-molecular pump. High purity argon gas is then bled into the chamber and the RF generator with an output frequency of 13.56 MHz is used to ignite the plasma. The target is pre-sputtered for ten minutes to remove any adsorbates on its surface prior to deposition. A deposition pressure of the order 10^{-3} mbar was used to grow the SiC thin films at a constant argon gas flow rate of 13.0 sccm.

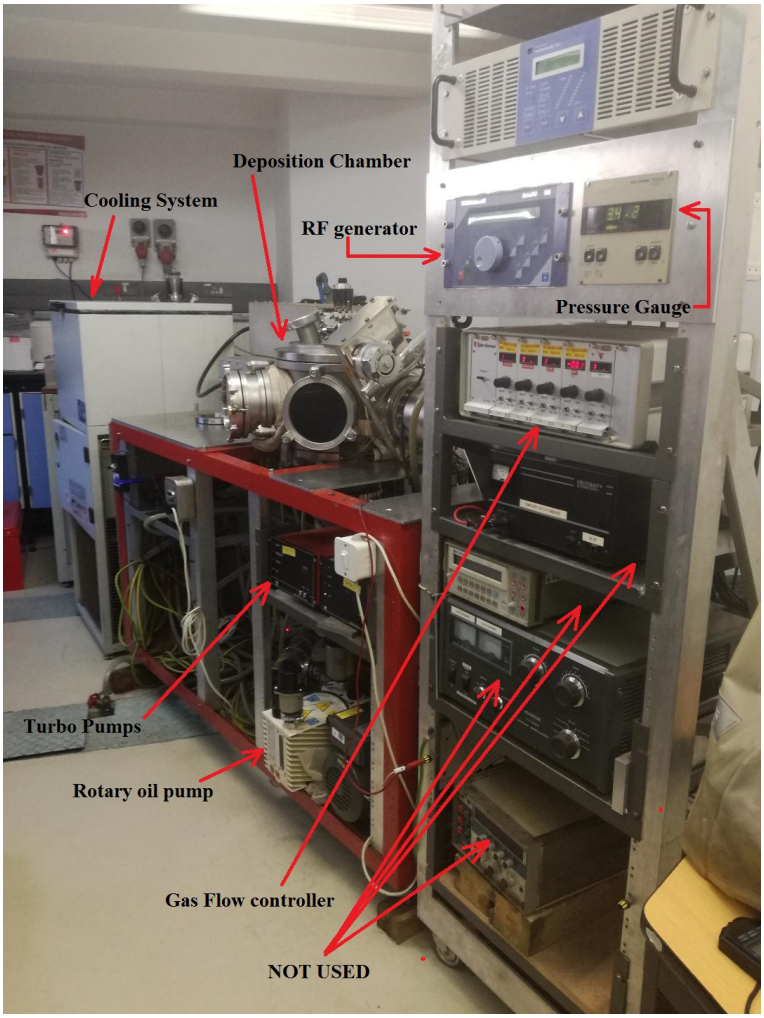

Figure 3.1: The radio-frequency magnetron sputtering system used for the deposition of the SiC thin films. The deposition system components are labeled. The part shown on the picture but not used by the system are also labeled.

All SiC films were deposited at room temperature (300 K) for five, ten and twenty minutes, respectively, for each substrate type. A set of SiC thin films were grown at 100 W and 150 W RF powers with no substrate bias. After deposition, the films were left for an hour to enable ventilation of the chamber when the turbo-molecular pumps were stationary and to allow films to gradually cool down

before removal from the chamber. This minimized the thermal stress developed by rapid quenching to room temperature. The films were 290 and 260 nm thick (SEM measurements, chapter five) at 20 minutes deposition time for 100 and 150 W deposition powers respectively. The deposition rates of the sputter system were then calculated to be 14.5 and 13.0 nm per minute at 100 and 150 W deposition powers respectively. The set of films deposited at 150 W were subsequently analyzed for elastic properties.

Table 3.1: SiC thin film deposition parameters.

Parameter	**Values**
RF Power (W)	100 , 150
Argon flow rate (sccm)	13
Base pressure (mbar)	order of 10^{-5}
Deposition pressure (mbar)	order of 10^{-3}
Deposition time (minutes)	5, 10, 20 minutes
Substrate	Si , Sapphire

3.3 Raman Spectroscopy

SiC can crystallize in about 250 polymorphs. It was, however, imperative to investigate the structural properties of deposited thin films and identify the phase present. Each of the possible SiC polymorphs produce different Raman spectra as a result of their atomic layer stacking sequences, some of which are shown in Figure 1.2. As a consequence the Raman Spectroscopy was employed (located at the School of Biology, University of the Witwatersrand, Johannesburg).

Raman spectroscopy is an analytical technique that provides information about the molecular structures and chemical environments of organic and inorganic molecules and molecular ions [63]. For detailed information about the technique, reviews by Herrero [64] and Rostron et al. [65] are helpful. The SiC film samples were analyzed with a Horiba Scientific LabRAM HR Raman spectrometer equipped with an Ar^+ excitation laser (514.5)(laser power in the range 0.2 to 1 mW). The laser spot diameter was varied between 7 and 100 μm (depending on which of the magnification microscope objectives was used). Data acquisition times varied between 60 and 120 s depending on the scattering efficiency of the sample. Several regions on the surface of each film were investigated in order to sample the different phases present in each sample.

3.4 Scanning electron microscopy and EDS

Scanning electron microscopy (SEM) involves scanning using a focused electron beam that is rastered laterally across a sample in a vacuum chamber. SEM provides important information which can range from topography (specimen texture), morphology, chemical compositions, such as elements and compounds present in the specimen [66], and it also shows the relative amount of composition and information when EDS is attached with it. A key feature of SEM is that it provides 3D images by scanning a particular selected area along parallel line patterns. A scanning electron microscope consists of some essential components including an electron emitting source for electron beam generation, anode, condenser lens, scanning coils, apertures and a user control interface. Inelastically scattered secondary electrons, backscattered electrons, and X-ray emissions are detected by a secondary electron detector (SED), elastically backscattered electron detector (BSED), and energy dispersive X-ray spectroscopy detector (EDX/EDS), respectively [66].



Figure 3.2: The scanning electron microscopy (SEM) used in the imaging and elemental composition determination of the deposited thin film.

To determine the thickness and elemental composition of SiC films deposited by RF magnetron sputtering method (discussed above), cross section SEM and EDS measurements were, respectively, carried out using the Carl Zeiss sigma field emission scanning electron microscope (FESEM) equipped with an Oxford x-act EDS detector (Figure 3.2). The SEM images and the EDS spectra of the as-prepared thin films were obtained using an emission current of 20 A and a bias voltage

of 16 kV. These measurements were conducted in the School of Chemical and Metallurgical Engineering, at the University of the Witwatersrand, Johannesburg.

3.5 Grazing incidence X-ray diffraction (GIXRD)

X-ray diffraction measurements of thin films using conventional $\theta/2\theta$ (Bragg Brentano geometry) scanning methods generally produces a weak signal from the film and an intense signal from the substrate. This is mainly due to the limited scattering volume. One of the ways to avoid intense signal from the substrate and get stronger signal from the film itself is to perform a scan with a fixed grazing angle of incidence, popularly known as GIXRD. GIXRD also allows the scattering vector ($\vec{q}$) to change with 2θ (detector angle) this enables probing of randomly oriented grains. The fixed angle is generally chosen to be slightly above the critical angle for total reflection of the film material [67].



Figure 3.3: The AXS Bruker D8 Discover X-ray diffraction instrument used for GIXRD and XRR measurements.

When an incident X-ray beam is directed towards a sample, the atoms of the sample will scatter the incident X-rays, generating a diffraction pattern. This diffraction pattern will form in positions where the scattered X-rays undergo con-

structive interference. It constitutes diffraction peaks whose pattern is a signature of the crystal structure unique to the material under investigation. For constructive interference to occur, the scattered X-rays must satisfy Braggs law given by

$$n\lambda = 2\,d_{hkl}\,sin\,\theta, \tag{3.1}$$

where λ is the wavelength of the monochromatic incident x-ray, θ is the Bragg angle, n is the order of diffraction and d_{hkl} is the inter-planar distance. The position of the diffraction peak relies on the inter-planar distance d_{hkl} between successive diffraction planes and the wavelength of the incident radiation as shown in Figure 3.4. Different plane orientations result in different 2 diffraction peaks. These planes are denoted by the Miller indices (hkl).

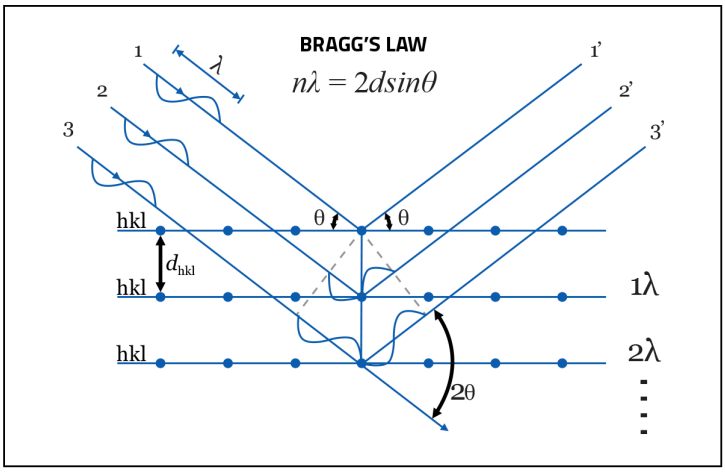

Figure 3.4: General schematic of X-ray diffraction by a crystal of inter-planar distance d_{hkl}.

In this study, the GIXRD based on the Seeman-Bohlin geometry was used to investigate the structural phases of a-SiC thin films. The Seeman-Bohlin geometry minimizes the substrate contribution to X-ray scattering through variation of the incidence angle, thus making the technique surface selective [68]. This geometry is restricted to samples with very smooth surfaces. Furthermore, the diffraction peaks are generally of low intensity due to the limited scatter volume. The penetration is highly dependent on the incident angle [68]. The GIXRD measurements were conducted using the Bruker AXS D8 Discover (shown in Figure 3.3) situated in the School of Chemistry at the University of the Witwatersrand, Johannesburg. The XRD patterns from the SiC/Si(001) from this study are presented in chapter five.

3.6 X-ray reflectivity (XRR)

XRR is a surface sensitive x-ray scattering technique employed to:

- study single crystalline, polycrystalline or amorphous material.
- evaluate surface roughness and interface width (< 3-5 nm)(arising from roughness and inter diffusion) nondestructively.
- measure film thickness from 0.1 to 1000 nm.
- study material density (< 1-2 %).

The XRR technique is based on the total external reflection since the refractive index of the medium for X-rays is less than 1 (refractive index of air). In this arrangement X-rays incident at an angle less than the critical angle θ_c will be reflected at the air-film interface. Using Snells law and elastic scattering, the electron density of the film can be obtained from the critical angle for total external reflection, θ_c, in the form:

$$\theta_c = \lambda\sqrt{\frac{r_e\rho_e}{\pi}}, \tag{3.2}$$

where r_e is the classical electron radius and ρ_e is the electron density. The oscillation curve of the XRR spectrum is a function of the film thickness and refractive index σ of the layer in which information about the film thickness, thickness of Kiess fringes, is obtained. The film thickness can then be given as

$$d = \frac{m\lambda}{2\sqrt{\theta_m^2 - \theta_c^2}}, \tag{3.3}$$

where m is the order of the interference maximum and d is the thickness. A comprehensive review on XRR has been covered by Janik [69]. Figure 3.5 shows a typical X-ray reflectivity geometry to illustrate the interference of reflected X-rays at the film-substrate and air-film interfaces. The XRR measurements were performed in a Bruker AXS D8 Discovery instrument equipped with a special reflectivity sample stage, a 4-bounce Ge monochromator crystal, a Ge(220s) analyzer crystal, a Goebel mirror and a 0.1 mm detector controlled slit (reasonable resolution requires slit of 0.1 - 0.2 mm). The selection of the primary and secondary optics is carried out to provide a symmetric geometry. The measurements were conducted in the School of Chemistry at the University of the Witwatersrand, Johannesburg. The measured XRR data were simulated on a Leptos software from Bruker AXS.

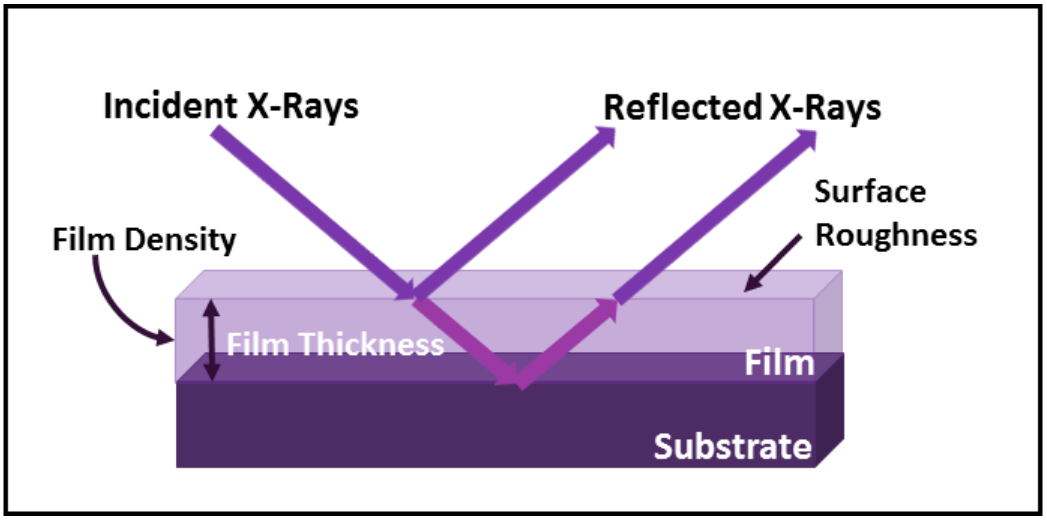

Figure 3.5: General schematic of X-ray reflectivity from film surface .

3.7 Rutherford backscattering

Rutherford Backscattering Spectrometry (RBS) is a widely used method for the near surface layer analysis of solids. It was used in this study to compliment EDS and Raman measurements. The thin films were bombarded with ions ($4He^{+}$) at an energy in the MeV-range (2 MeV), and the energy of the backscattered projectiles was recorded using a silicon detector tilted at 165°. The 20 keV energy resolution of the system was determined from the signal of thin a-SiC layers. The beam used was 1 mm wide and had current ranging from 300 - 550 pA for respective experiments. The detector-sample distance was 50 mm. The pressure in the chamber during the experiments was around 10^{-6} mbar. Basic data acquisition were done with the OM-DAQ program [70].

The information in the RBS spectrum were used to establish the thickness and composition of the layers in the sample. In general, for a simple spectra, it is sufficient to measure peak heights, area or widths and follow simple analysis procedures to determine these quantities [71]. In analyzing more complex spectra, it is usually adequate to use a computer program which generates a theoretical spectra based on hypothesized sample structures. The standard technique is to view an overlay of synthesized spectrum with the experimental one, and iteratively modify the parameters of the synthesis until an adequate fit is achieved [72]. In this work, the obtained experimental data were simulated and analyzed using RUMP software package [73]. The RBS equipment used in this work was from iThemba LABS, Johannesburg.

3.8 Optical Spectroscopy (Transmittance) measurements

Material opacity plays an important role in SBS measurements; since it determines the nature of the scattering geometry and the dominant scattering mechanism (chapter 2). Additionally it prescribes the scattered light polarization to be used for observing certain exotic modes (in transparent samples "love" modes can only be observed at p-s scattered light polarization [74]).

SiC/Sapphire samples appeared to be transparent when viewed by a naked eye. From this observation, it was then important to measure the transmission spectrum of a-SiC. Transmission measurements were done using the UV-VIS-NIR 500 Cary spectrophotometer found in the School of Physics, University of the Witwatersrand, Johannesburg. The 8.01 version of the instrument was used, ran on a control software called Scan Software Version 4.10(464). After baseline calibration for 0 and 100 % transmittance the sample was scanned from 400 - 700 nm since the main analytical technique, SBS, utilizes visible light. Transmission measurements are presented in chapter five.

3.9 SBS: Experimental setup

This section presents a comprehensive overview of the SBS experimental technique (equipment located at the School of Physics, University of the Witwatersrand, Johannesburg). SBS serves as the last and main experimental technique to determine the elastic constants of a-SiC film. A theoretical description of the SBS experiment was highlighted in chapter two, as stated, a resolution of weak inelastically scattered light by thermally induced acoustic waves forms the most important part of SBS. As highlighted in section 2.2, this resolution requires a highly sensitive instrument. The high contrast (10^{11}), described by Mock et al. [75], of the multipass Fabry-Pérot interferometer developed by Sandercock serves that purpose.

A basic Brillouin scattering interferometer requires: a source of highly monochromatic coherent laser light, a high resolution (GHz range) and high contrast (10^{11}) spectrometer, a very sensitive detector and a multichannel analyzer. Figure 3.6 shows a pictorial view of the SBS setup. Figure 3.7 presents a schematic representation of the SBS apparatus highlighting the external optics, the 3+3–pass tandem Fabry-Pérot interferometers (TFPI) and the data collection equipment.

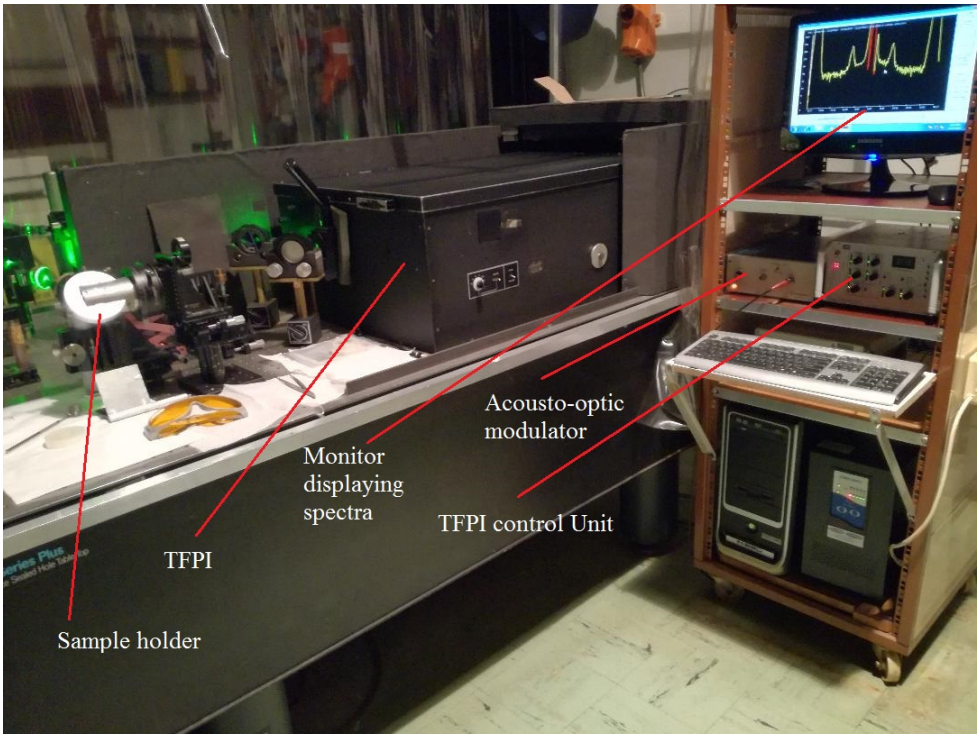

Figure 3.6: Surface Brillouin scattering pictorial representation showing the Tandem Fabry Pérot Interferometer (TFPI) and auxiliary electronics.

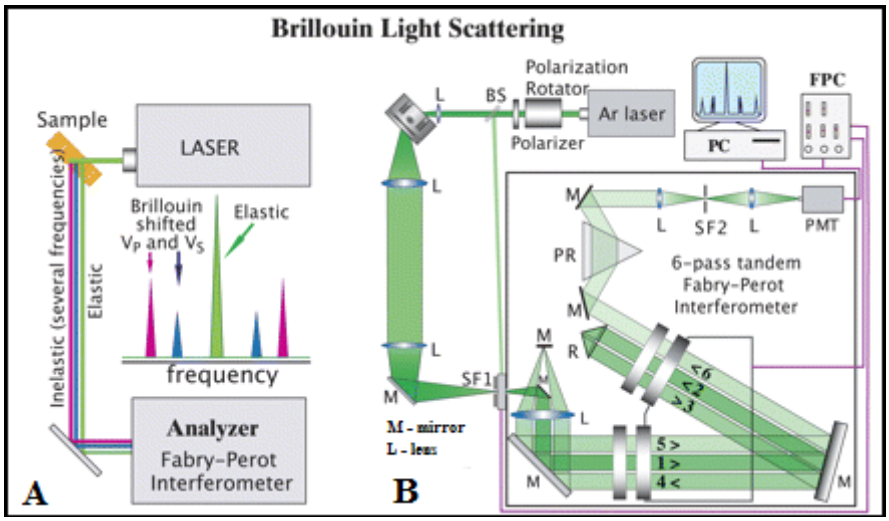

Figure 3.7: (A) General schematic for most light-scattering experiments. Laser light hits the sample and the scattered light is analyzed. (B) A more complete diagram of a Brillouin-scattering experiment. PC = personal computer; PMT = photomultiplier tube; FPC = Fabry-Perot controller; BS = beam splitter [76].

3.9.1 The laser

A compact and reliable Diode-Pumped Solid State (DPSS) laser (Torus 532 laser system of Laser Quantum) was used in the SBS measurements. The torus 532 laser is a high specification, emitting visible light at 532 nm with an output power up to 750 mW making it ideal for Brillouin scattering. Using intelligent electron-

ics, the torus continually tracks its longitudinal mode position and ensures there is no mode-hop. In order to strongly attenuate the intensity of relatively spurious secondary laser modes, a temperature stabilized etalon device (Temperature controlled filter (TCF)) is used. These modes are very weak, with an intensity typically 10^{-8} to 10^{-11} of the laser intensity, however, these lie in the region of interest for Brillouin spectroscopy measurements, hence, the need for attenuation. Figure 3.8 shows the spectrum of the laser source measured using the JRS high contrast tandem interferometer. The main laser peak has been strongly attenuated relative to the secondary peaks. A Brillouin spectrum measured in the presence of a strong elastic component will show these secondary peaks in the background, making interpretation of the spectrum difficult. The TCF attenuates theses modes below the detection threshold.

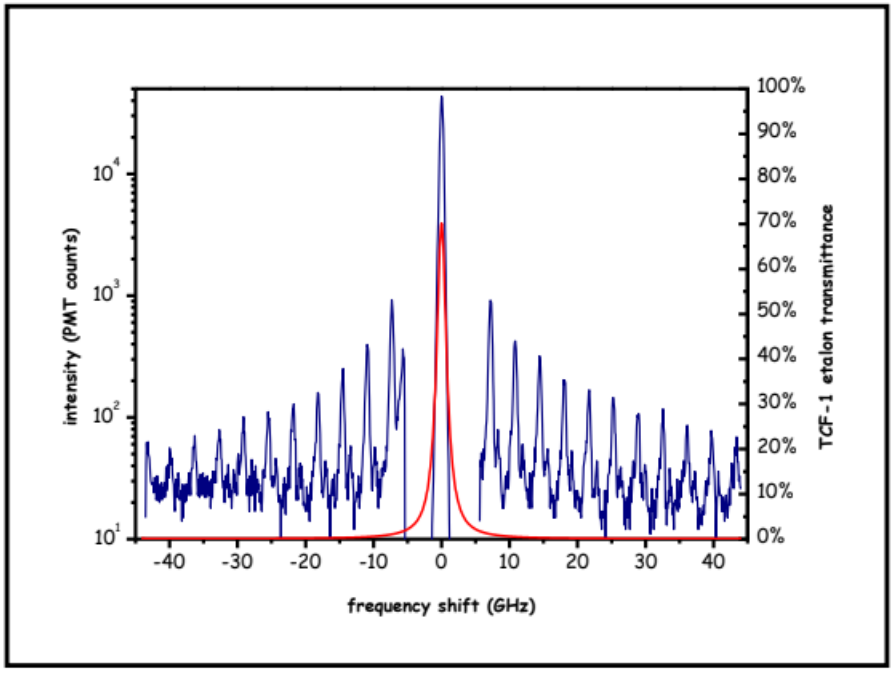

Figure 3.8: Spectral cleaning. The blue curve shows the spectrum of a laser source, showing several additional modes extending out as far as 100 GHz, as was seen by means of a high contrast Fabry-Pérot interferometer. The red curve shows the theoretical transmission curve of a TCF unit (Extracted from the "Temperature controlled laser filters TCF-1/TCF-2" Instruction manual).

The torus is a single longitudinal mode laser. Control of the laser can be accessed through a dedicated RS232 port on the PSU. The unique patented travelling-wave cavity results in an ultra-low noise output. The torus TEM_{00} spatial mode gives a beam with Gaussian intensity profile (bandwidth – 1 MHz), minimum divergence (<0.4 mrad) and the smallest spot size (1.7 ± 0.2 mm).

3.9.2 The tandem Fabry-Pérot interferometer (TFPI)

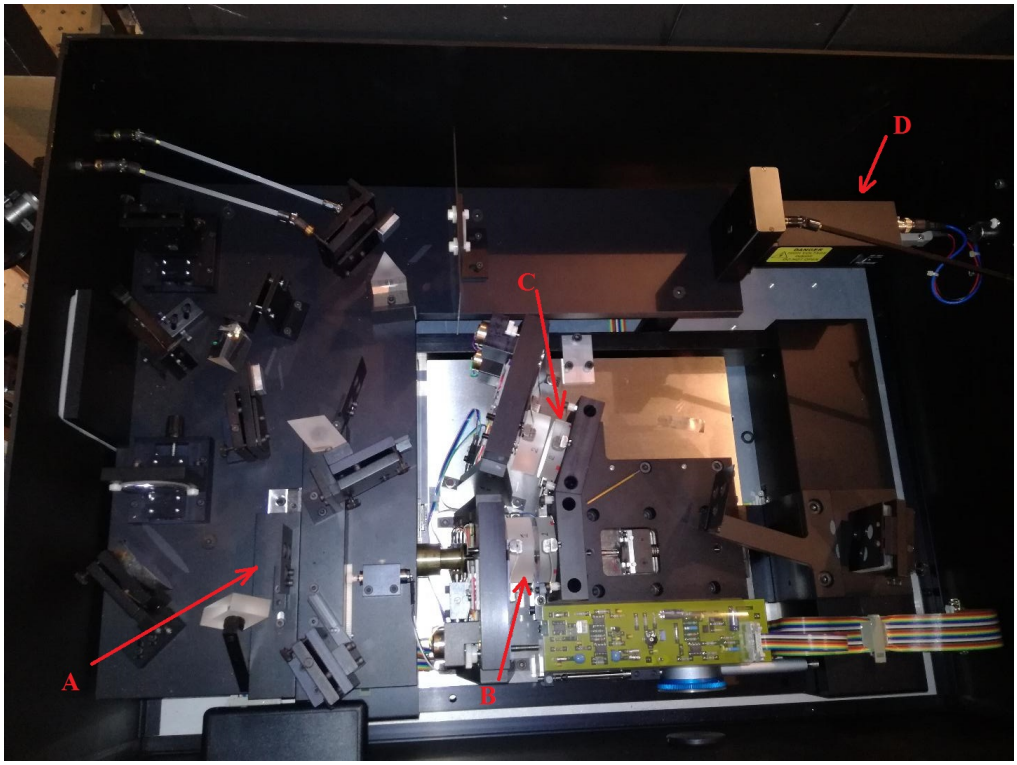

Figure 3.9: Aerial view of the JRS Instruments (3+3) multipass Tandem Fabry-Pérot Interferometer used in the experiments. (A) marks the position of a translation stage for switching between alignment mode and tandem mode during set-up procedure, (B) and (C) mark Fabry-Pérot 1 and Fabry-Pérot 2 respectively and (D) is the detector.

The history of the Brillouin spectroscopy shows several main stages of advancement connected to improvements in Fabry Pérot interferometers and methods for employing them [77, 75, 78]. A basic Fabry-Pérot interferometer (FPI) consists of two plane mirrors mounted such that they are parallel to each other, with an optical spacing L between them. The FPI produces a series of peaks when there are constructive interference within the cavity. For normal incidence, the instrument transmits light of wavelength λ only if the distance L is equal to a multiple of half the value of the incident wavelength, namely $L = m\lambda/2$ where m is an integer. This can be understood by considering the interference between the ray directly transmitted by the two mirrors and the ray that experiences double reflection inside the interferometer cavity. Neighboring orders of interference are therefore separated in frequency by an amount $\Delta v = L/2$ wavenumbers ($\Delta v = L/2 = 150/L$ GHz mm^{-1}). The inter-order spacing is called the free spectral range (FSR).

Considering the multiple reflections inside the interferometer cavity the trans-

mitted intensity is given by the Airy function $T(L/\lambda)$

$$T\left(\frac{L}{\lambda}\right) = \frac{T_o}{1 + \left(\frac{2F}{\pi}\right)^2 sin^2\left(\frac{2\pi L}{\lambda}\right)} \tag{3.4}$$

where $T_o(< 1)$ is the maximum transmission and F is the finesse of the interferometer which is responsible for the fringes' width and depends on the flatness and reflectivity of the mirrors. The single FPI suffers from overlapping of interference orders of different spectral features of the scattered signal. One way of attending to this problem would be using large values of FSR, however, this sets a limit on the spectral resolution, low-energy peaks in the spectrum cannot be resolved from the central elastic peak. The best way to solving this problem is by using equipment with two interferometers mounted on the same scanning stage at an angle θ (as shown in Figure 3.10) having different mirror spacings, L_1 and L_2 (tandem interferometer). This configuration works as a tunable optical filter whose peak transmission is close to unity over a narrow spectral interval. In practice the ratio is set at $L_2/L_1 = 0.95$, a condition required for synchronization of the two interferometer scans [79]. The total transmission curve is composed of a central elastic peak and small ghosts symmetrically positioned on either side representing weakly transmitted interference orders of the two interferometers.

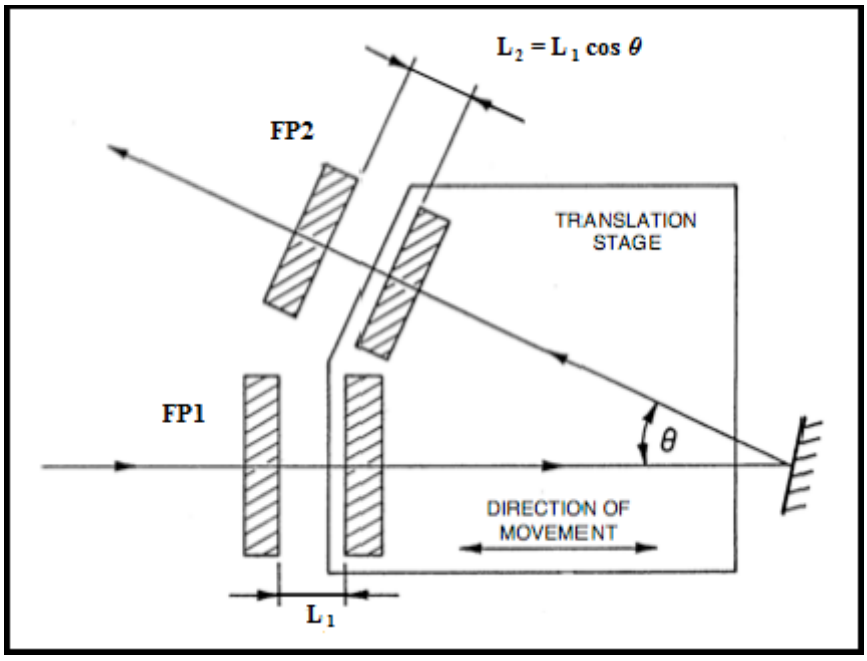

Figure 3.10: A schematic plan view of the two Fabry-Pérot interferometer on a single translation stage [75].

In the present work, a (3+3)-Pass TFPI (shown in Figure 3.9) mounted on a Vibration Isolation System MOD - 2 (produced by JRS Scientific Instruments) was used. The TFPI achieved a contrast as high as 10^{11} providing the capability

to distinguish the weak inelastically scattered light from the intense elastically scattered light. Thus, it was possible to study the weak acoustic phonon modes from the surface and observe the weak longitudinal and transverse thresholds of the Lamb continuum.

3.9.3 Photo - detectors

As a consequence of the low intensity of the Brillouin signals, a single-photon counting detector is recommended. For this purpose, low-noise photomultiplier tubes (PMT) having a dark count 0.3 per second are generally used. The EG&G Optoelectronics Canada SPCM-200-PQ silicon avalanche photo-diode was used for all the experiments in this work. This device has a higher quantum efficiency advantage over a PMT, however, it has a disadvantage of a higher dark count of 1 per second relative to 0.3 per second for the PMT. In practice nevertheless, the higher quantum efficiency translates to reduced time to accumulate a spectrum of between four and five times for the EG&G device compared to a PMT.

3.9.4 The multichannel analyzer

The spectra in this present work were recorded using a personal computer based multichannel analyzer (MCA) interfaced with the TFPI and the detector. The MCA used was a Windows based JRS Scientific Instruments Ghost multichannel analyzer. The MCA works with a software for data analysis and spectrum calibration. The spectra were stored in ASCII format and later analyzed using the OriginLab software. Up to 512 channels were used to obtain spectra of sufficient quality and also provided an acceptable interplay between acquisition time and resolution. All spectra were collected at 600 scan amplitude which gave spectra in the range -40 to 40 GHz.

3.9.5 Alignment of the TFPI for SBS measurements

This section aims to highlight the daily operation of the SBS equipment, also included is the discussion on aligning the TFPI for SBS measurements. It should be noted that all operations of the SBS instrument were done in a dark environment. This was done to avoid possibly saturating the detector and to avoid interfering with the adjustment of the auxiliary optics for focusing.

Measurements on the a-SiC films and SrF_2 were done with samples mounted on a machined sample holder fitted with a goniometer to enable angular variations for both incident and azimuthal angles. All measurements were done in backscattering geometry (180° scattering) meaning the scattered light was collected by the

same lens and steered to the entrance pinhole of the TFPI by two optical mirrors operated in a periscope alignment. Simultaneous fine adjustments of the steering mirrors and the focal length projected the image of the sample onto a white card that was placed on the translation stage of the TFPI (the card was removed after confirming the projection of the image). Viewing of the image was usually done at full laser intensity (depending on the scattered light) which was adjustable by using a acousto-optic modulator (AOM). The AOM was used to adjust the intensity of the laser beam, implying, the laser power source was only set once per measurement. When the image on the white card showed a circular bright image against a dark background, the focusing was at its optimum position.

The next step was the alignment of the TFPI as explained in the JRS Operator Manual for the tandem interferometer [80]. The typical output, before and after optimization, with the TFPI in alignment mode is shown in Figure 3.11. When there was satisfaction that the experimental setup was optimal, the collection of the SBS spectra was started.

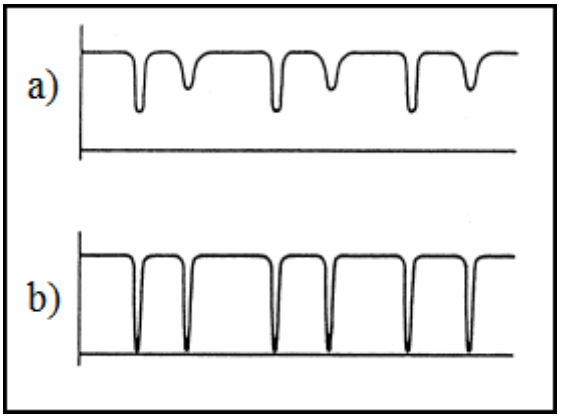

Figure 3.11: Diagrammatic representation of the pre-alignment process for the TFPI system. a) Shows the measured reflected intensity for two imperfectly aligned interferometers, b) shows the intensity after correct alignment but before synchronization [80]

.

The measurements done in this work used a 4 mm mirror spacing to separate the weaker surface wave excitations from the intense elastic peak. A comprehensive discussion on mirror spacing was done by Sussner and Vacher [81]. SBS spectra were collected at angles 30° to 80° with accumulation time of about 8 – 36 hours per angle at 10° intervals. The long accumulation times were a consequence of the low scattering efficiency of SiC film.

3.9.6 Error analysis in SBS measurements

Most errors in the SBS technique are identified as; instrumental errors, scattering geometry errors and errors from the scattering cross section. Instrumental errors are associated with the calculation of the frequency shifts of corresponding Brillouin scattering peaks and these calculations are a result of an error in measuring the mirror spacing, the position of the ghost peaks and Brillouin scattering peaks.

Brillouin scattering is sensitive to scattering geometry. Scattering geometry errors arise from the collection of scattered light by an aperture collection lens. The aperture allows phonons with a range of wave vectors to contribute to the measured scattered light leading to the broadening of the phonon line shape resulting in the introduction of a systematic shift in the position of the peak. When the scattering geometry is well controlled, the uncertainty in measured frequency is typically less than 0.5 – 1 % [82].

Errors associated with the scattering cross section depend on the scattering intensity as a function of scattering angle. In the case of polarization in the sagittal plane (p-p polarization) of the backscattering geometry, an error of 1° in the external scattering angle (in symmetric geometry with an 80° scattering angle) will produce approximately 1% error in the measured frequency [82]. To minimize these errors scattering angles are kept between 30° and 70°, 70° being the most favorable because of the increased scattering intensity which directly translates to better spectral features.

In response to these identified errors, the mirror spacing was kept at 4 mm by adjusting a precision clock gauge to within 0.01 mm. Following the latter statement, an error of 0.25 % can result in the setting of the free spectral range (FSR). Calculating an arithmetic average of the obtained Brillouin frequency shifts helped in eliminating the error in the elastic peak position. An overall error estimate from the discussion above amount to between 1-2 % of the measured frequency shift [83].

3.10 Summary

This chapter defined and highlighted on the experimental techniques that were used in characterizing the deposited films. Specific machines used were stated including the procedures followed to obtain results. All physical aspects of the main technique (Brillouin scattering spectroscopy) were highlighted. Chapter four presents an investigation of elastic constants of a bulk transparent sample.

Chapter 4

Elastic constants of transparent bulk material (SrF_2)

4.1 Introduction

The alkaline-earth fluorides have long attracted the scientific and technological interest because of their fast-ion conductivity in the vicinity of the melting temperature [84]. More recently alkali earth fluorites have been used for extreme ultra violet based lithography which requires precise determination of their elastic strain. The elastic properties of these alkaline-earth fluorides have been investigated over the years by using the traditional ultrasonic pulse-echo technique [84]. The present chapter describes the measurements of elastic constants of Strontium Fluoride (SrF_2) at ambient temperature and pressure by Brillouin light scattering technique. The measurement of frequency shifts of Brillouin lines along a specific propagation direction allows the determination of the phase velocity of the elastic waves by a simple application of Snells law [28]. The elastic properties and velocities obtained of transverse and longitudinal acoustic modes of SrF_2 were compared to those found in literature [84].

4.2 Characterization of SrF_2

Strontium Fluoride (SrF_2) is a super-ionic conductor with a fluorite structure that is based on a face-centered cubic (Figure 4.1), space group Fm3m, with four atoms per unit lattice cell. The fluorite structure has eight fluorine atoms arranged in a cube around the strontium atom, with the cubes of fluorine edge connected in a face-centered cubic array. The fluorine atom is surrounded by four strontium atoms arranged in an ideal tetrahedron, with the tetrahedra also edge-connected [85, 86]. SrF_2 offers a range of transparency from the ultraviolet to the long wave

infrared, with low reflectance loss and low dispersion which promotes its optical applications [87, 88].

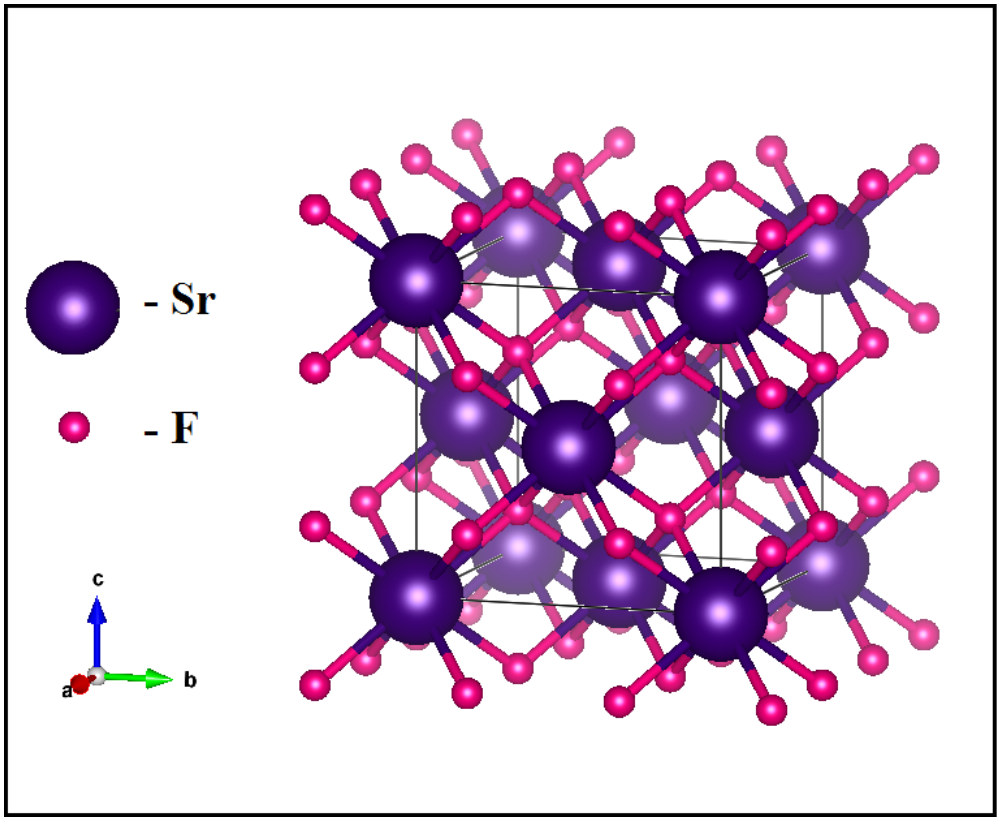

Figure 4.1: Unit cell of SrF_2 known as the fluorite structure, drawn using VESTA 3 software developed by Momma and Izumi [89].

4.2.1 Raman spectroscopy results

Raman spectroscopy was used to verify the crystallinity of the SrF_2 sample. The Raman bands of the sample were examined using a Horiba LabRAM HR Raman spectrometer equipped with an Ar ion laser (514.5 nm) and a laser power of 0.4 mW. Figure 4.2 shows a typical Raman spectrum for the SrF_2 sample at ambient temperature. It reveals a peak located at 289 cm^{-1}, normally observed at low temperatures ($\approx$ room temperature) as an intense T_{2g} phonon. The position of this peak is in good agreement with observations reported by Glynn et al. [90] and Van der Marel and Den Hartog [91], associated with single crystals of (001) lattice plane.

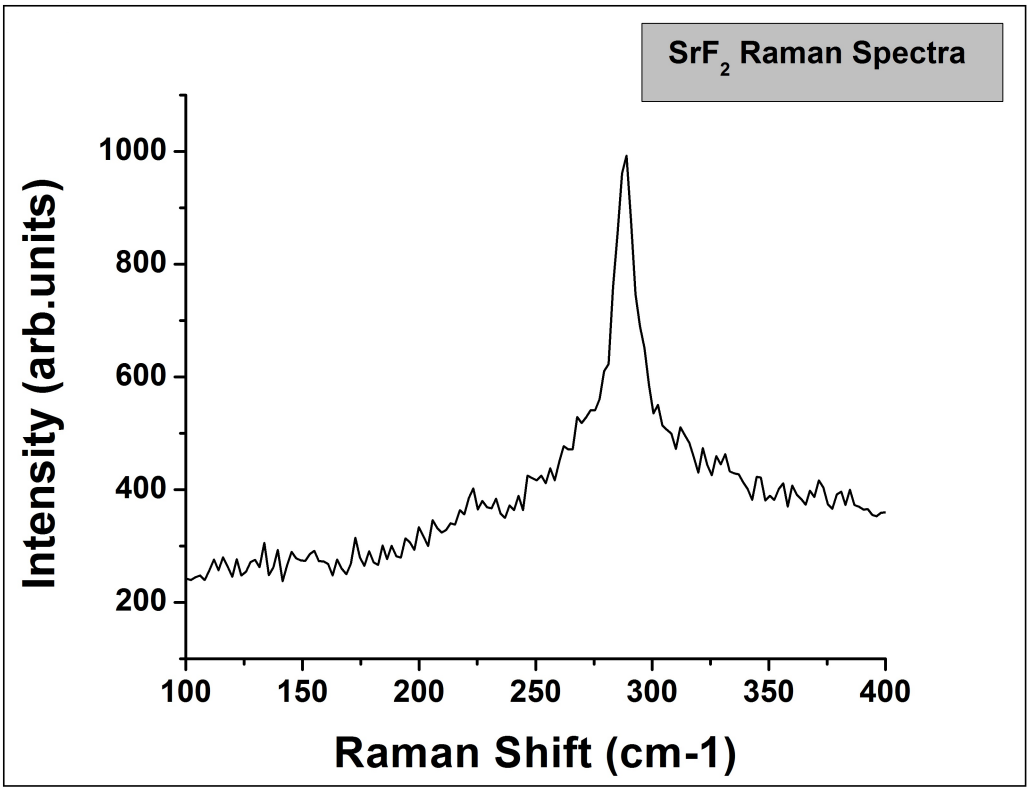

Figure 4.2: Raman spectrum of SrF_2 showing the allowed Raman-active phonon for the pure SrF_2 crystal at 289 cm^2.

4.2.2 XRD results

The crystallinity of as-prepared SrF_2 was characterized using powder X-ray diffraction (XRD). Figure 4.3 shows the diffraction pattern collected for SrF_2 sample in the 2θ range of 10 - 100 degrees. No impurities were observed in the sample. All of the diffraction peaks in Figure 4.3 are indexed to a pure face-centered cubic phase [space group: Fm3m (225)] of SrF_2 with an accompanying lattice constant a = 5.805 $\mathring{A}$ comparable to the corresponding literature value of a = 5.800 $\mathring{A}$ (JCPDS 06-0262). The XRD atomic density was determined to be 4.26 gcm^{-3} for an ideal SrF_2 lattice with 4 atoms of Sr and F. The weakness of the (200) reflex in Figure 4.3 implies that there could be an axis tilt from the [100] direction (SrF_2 sample was not perfectly oriented).

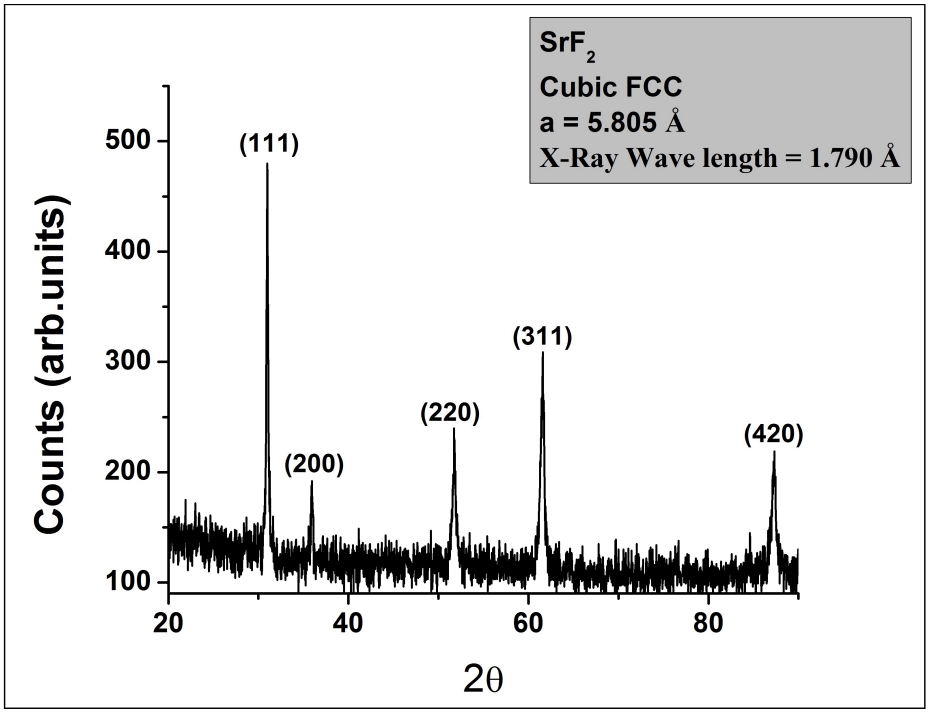

Figure 4.3: X-Ray diffraction pattern of SrF_2.

4.2.3 EDS results

Energy dispersion x-ray spectroscopy (EDS) was performed on the SrF_2 sample to supplement the XRD results and determine the elemental composition of the sample. Figure 4.4 shows the EDS spectrum obtained from a SEM described in section 3.4 with 1500 × magnification at 30.00 kV HV. EDS confirmed the presence of Sr and F elements.

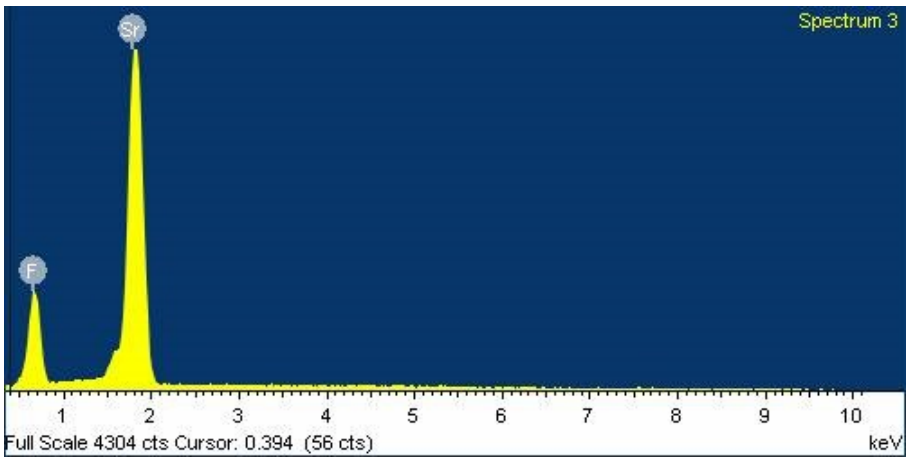

Figure 4.4: EDS pattern of SrF_2.

After characterization and knowing the crystal structure and crystallinity of the SrF_2 sample the elastic properties were then investigated using Brillouin scattering spectroscopy.

4.3 Brillouin scattering results on SrF_2

Unlike in the thin film surface Brillouin scattering (SBS), in bulk transparent materials the elasto-optic Brillouin scattering mechanism (section 2.2.1) is dominant. Back scattering configuration (Figure 2.1) was used to obtain three independent elastic constants of SrF_2. The phonons, satisfying the wave vector conservation in a given Brillouin scattering geometry (e.g Figure 2.1) have wave vectors given by $q = \pm(k_i - k_s)$; $|q| = \pm 2|k_i| \sin\theta$ (section 2.2.1). The relationship between sound velocity v and the Brillouin scattering frequency shift $\Delta\omega$ can be determined by these scattering geometries. With back scattering (180° scattering),used in this study, $v = 2\pi\Delta\omega/q$, where q is the phonon wave vector equivalent to $4\pi n/\lambda$, with n being the refractive index of the crystal and λ, the wavelength of the laser. The laser used in this study emits 532 nm wavelength radiation and SrF_2 has a refractive index of 1.440 [33]. The elastic constants of a material, along with its density, determine the phase velocity of acoustic waves along their polarization modes.

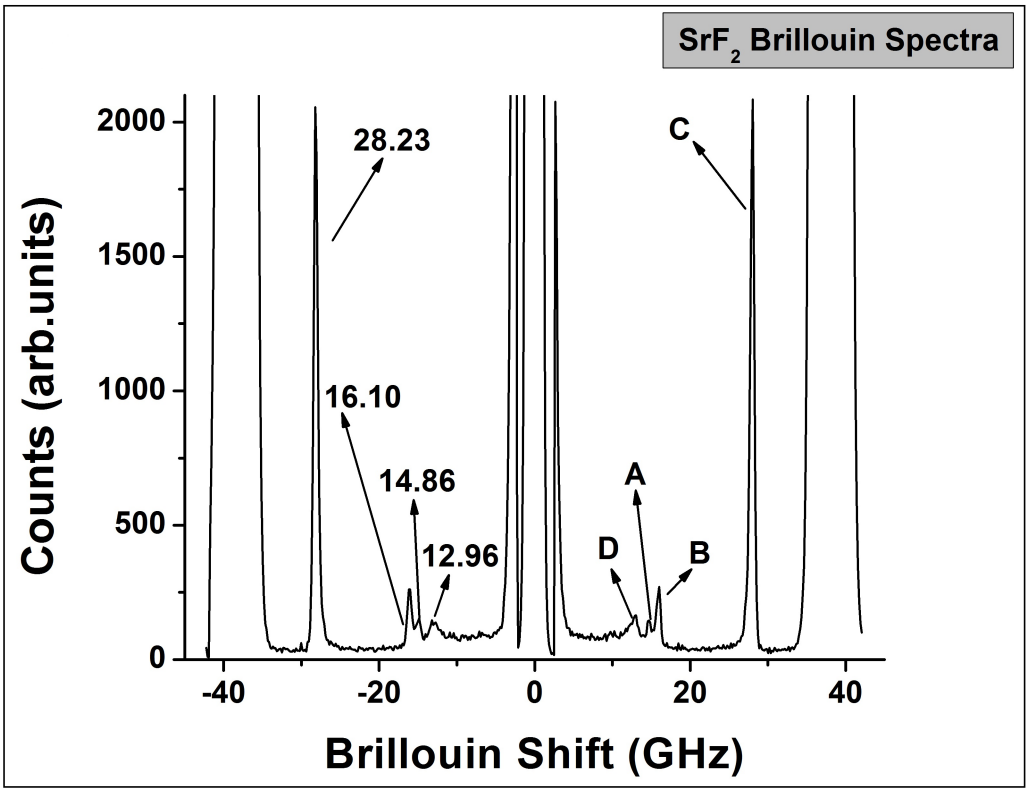

Figure 4.5: Brillouin spectra of SrF_2 showing all modes observed at incident angle of 60°.

In order to observe the longitudinal acoustic phonon (LA) and two transverse acoustic phonons (TA1 and TA2), in Brillouin scattering, the polarization of scattered light was not analyzed in the experiment. A typical Brillouin spectra collected from the SrF_2 sample is shown in Figure 4.5. The strong signal at

zero Brillouin shift arises from Rayleigh scattering. The spectrum consists of A, B, C and D modes that are symmetric about zero Brillouin shift, corresponding to Stokes and anti-Stokes scattering. The data accumulation time from the 512-channel analyzer varied from about 30 minutes to an hour. Frequency dispersion curves were obtained to establish the nature of the modes observed and the directional dependence of the phonon wave vector. By varying the angle of incidence, it was possible to establish whether the observed modes were surface or bulk modes. Taking $q = 4\pi \sin\theta/\lambda$ for surface modes, frequency dispersion curves were plotted (Figure 4.6). The modes A, B and C showed that the Brillouin shift is invariant to the incident angle suggesting that these are bulk acoustic modes. The expression

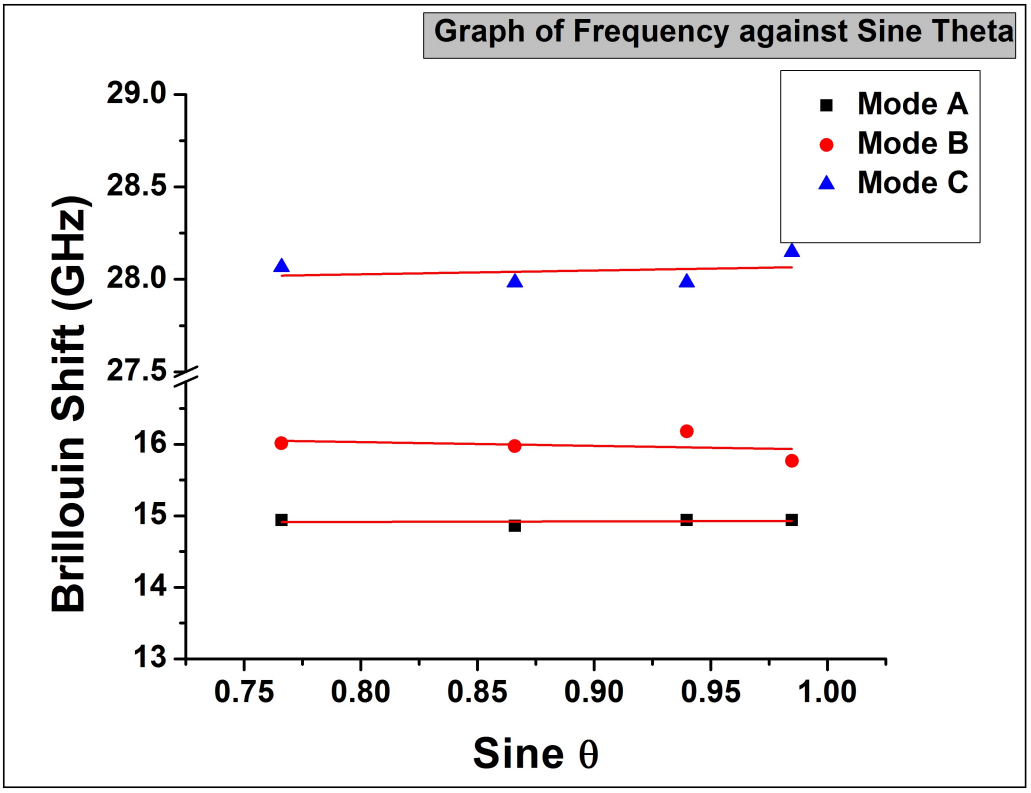

Figure 4.6: Frequency dispersion plot for modes A, B and C observed in Figure 4.5.

for q above is true only for surface acoustic waves (SAW) and gives a linear graph in response to the change of $\sin\theta$. In the case that the modes under investigation are found to be bulk modes, $q = 4\pi n/\lambda$ is used to calculate the phonon velocities. The velocities for modes A, B and C were calculated to be 2770, 2960 and 5180 m/s respectively and these compare well with values obtained by Crouch et al. [92] and Gerlich [84] of 2720, 3040 and 5200 m/s respectively.

Brillouin scattering from cubic crystals has been analyzed theoretically by Benedek and Fritsch [93],their theory was further extended to describe the spectra scattered from a cubic crystal in an arbitrary orientation with respect to the

incident light beam [42]. The generalization was necessary and applicable to the present investigation because it was difficult to know the exact crystal orientation, though Raman results seem to indicate a likely (001) plane. The anisotropic cubic SrF_2 is characterized by three independent elements of the elastic tensor, namely; c_{11}, c_{12}, and c_{44} (section 2.1.1). Using a quarter-wave plate, the incident light for the Brillouin light scattering was set as a mixture of p and s-polarization. This approach enabled the observation of the dependence of the acoustic waves with polarization directions. The s-s polarization means both the incident light and the scattered light were normal to the sagittal plane (the plane of incidence). The p-p polarization means both the incident light and scattered light lay on the sagittal plane. The s-s and the p-p states describe both the pure surface and bulk contributions to a scattering cross-section [42]. However, mixed configurations, namely s-p and p-s, describe only elasto-optic contributions [94].

After confirming the bulk nature of the modes in Figure 4.6 $q = 4\pi n/\lambda$ was used to calculate the velocities and to plot the azimuthal dispersion curves of individual modes in Figures 4.7 and 4.8. The Brillouin spectra were obtained at fixed 60° incident angle at 5° azimuthal angle intervals from 0° to 90°. Figures 4.7 and 4.8 show the orientation dependences of the longitudinal and shear moduli of the SrF_2 crystal in (100) plane, in which solid lines represent the angular dependences of ρv^2 for different modes, and the shaded squares represent experimentally measured data. It turns out that the velocity of the compressional (LA) mode is strongly dependent on orientation. It follows from Figure 4.8 that its velocity reaches a maximum along the [001] propagation direction, and it decreases to a minimum in the [011] direction. The velocities of the first shear (TA_1) mode (Mode B in Figure 4.6) do not change for different propagation directions (dispersion plot shown in Figure 4.9). TA_1 is a shear mode with predominantly vertical polarization, whilst TA_2 and LA modes have predominantly horizontal polarization and thus exhibit weakly anisotropic behavior. On the other hand, the velocities of the second shear (TA_2) mode (Mode A) change significantly with propagation direction. The TA_1 and the TA_2 modes represent the shear waves propagating in the same (100) plane with their particle displacements perpendicular to the plane. The TA_2 mode has a maximum velocity in [011] and a minimum velocity in [001], which indicates the presence of a soft shear acoustic mode in [100] of SrF_2. Mode D at about 13 GHz was unidentified since it only appeared on the p-s polarization state. For the (001) surface cut, because the normal to the (001) plane is a fourfold symmetry axis, the SAW speed is periodic every $\Delta\theta = 90^o$. In addition, the $< 110 >$ direction is a twofold symmetry axis, and therefore the SAW speed is symmetric about that direction $\theta = 45^o$ in Figures 4.7 and 4.8. Materials with Zener anisotropy ratio $\eta = 1$ are nearly isotropic and hence have nearly constant SAW speed for all directions,

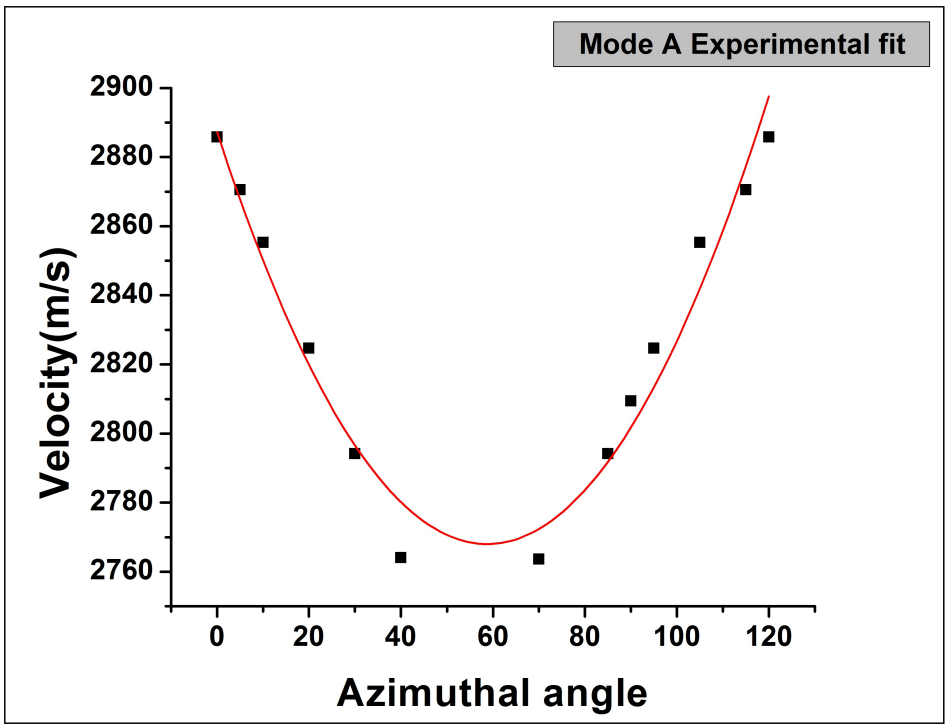

Figure 4.7: Azimuthal dispersion plot for mode A in SrF_2 Brillouin spectra taken at 60° constant incident angle.

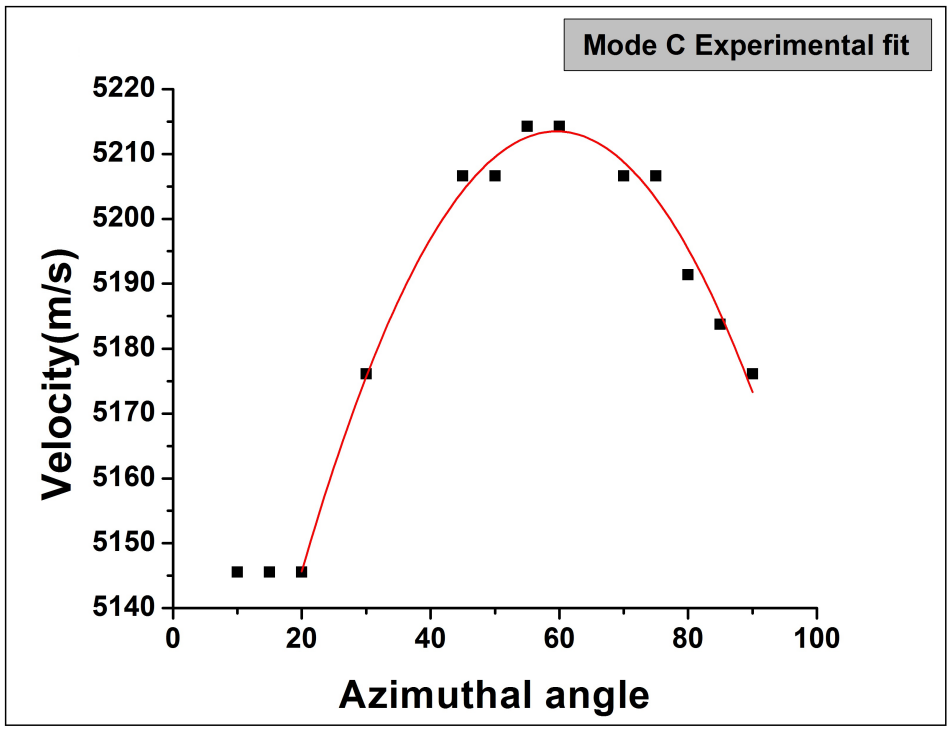

Figure 4.8: Azimuthal dispersion plot for mode C in SrF_2 Brillouin spectra taken at 60° constant incident angle.

SrF_2 has $\eta \approx 0.80$. For all materials, the direction $\theta = 0^o$ is a pure mode, and the particle trajectories are confined to the sagittal plane. Some materials have

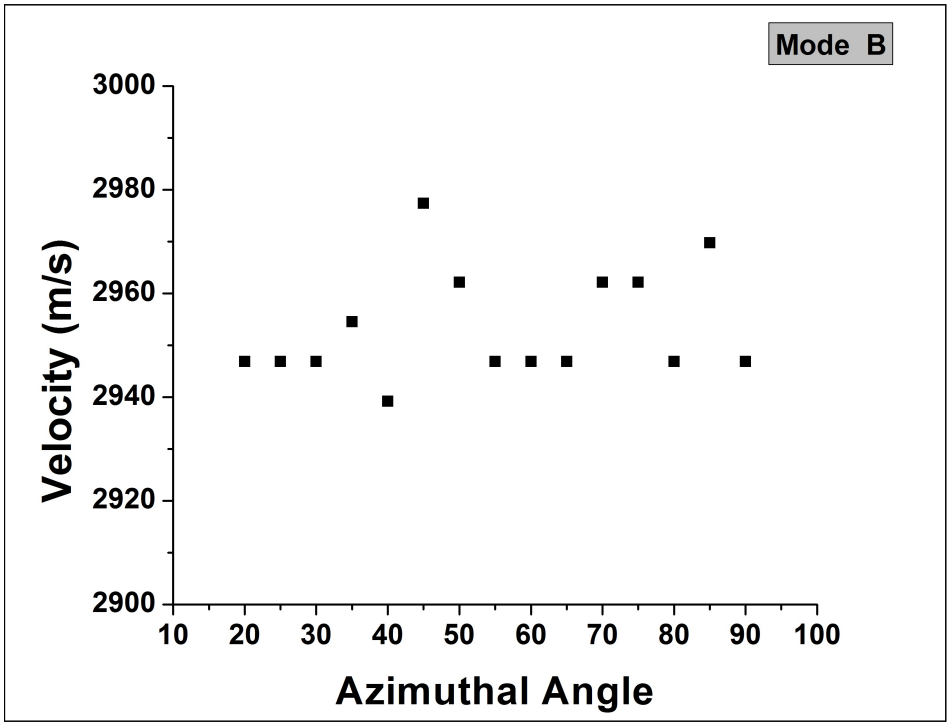

Figure 4.9: Azimuthal dispersion plot for mode B in SrF_2 Brillouin spectra taken at 60° constant incident angle.

additional pure modes in other directions, but in these cases the SAW often has a transverse component e.g., Ni, Cu, Si, Ge [95]. In some materials, the SAW speed approaches the transverse bulk wave speed as the direction approaches $\theta = 45^o$. This effect is the source of the dip in the SAW speeds of Ni, Cu, Si, and SrF_2 as observed in Figure 4.7. The SAW becomes a shear horizontal bulk wave at $\theta = 45^o$, a direction that coincides with the $< 110 >$ diagonal.

The values of elastic moduli c_{ij} may be obtained from the relationship $c_{ij} = \rho v^2$ (Table 2.3). Figure 4.7, gives the transverse mode (TA_2) propagation velocity in the [100] direction, giving $v_{TA(2)} = 2764.6$ m/s at 59.9^o thus $c_{44} = 32.5$ GPa, these values that compare very well with Gerlich [84] and Catlow et al. [33]. Figure 4.8, on the same propagation direction [100] we get the longitudinal mode propagation velocity to be $v_L = 5215$ m/s at 58.2^o thus $c_{11} = 116$ GPa. The SAW speed ($\approx$ 2890 m/s) approaches the transverse bulk wave speed as the direction approaches $\theta = 45^o$ giving $c_{12} = 44.6$ GPa. Table 4.1 outlines the comparison of obtained c_{11}, c_{12} and c_{44} values with those found in literature.

Table 4.1: Experimental SrF_2 elastic constants c_{11}, c_{12} and c_{44} values compared to the literature values.

	ρ (g/cm^3)	Refractive index	Elastic Constants (GPa)			Technique
			c_{11}	c_{12}	c_{44}	
SrF_2	4.275	1.44	123.8	42.6	32	Brillouin [33]
			123.5	43.05	31.28	Ultrasonics [84]
	4.26	1.44	115.8	44.6	32.5	This work
			121.6	43	29.93	Pulse-echo [92]

4.3.1 Summary

The bulk elastic constant of a transparent material were investigated in this chapter. An appreciation of the Brillouin elasto-optic scattering mechanism was gained. Three independent elastic constants of the SrF_2 sample were determined using the Brillouin light scattering spectroscopy. c_{12} and c_{44} values are similar to that found in literature, whilst the c_{11} value deviates from that found in literature by about 6 %. The deviation could be attributed to slight disorientation of the plane, hence affecting the location of the minimum/maximum on the dispersion curve. The error may also be caused by the use of literature value of the refractive index which may differ from the actual value of our sample. It was possible to determine c_{12} by combining measurements of v_L and $v_{TA(2)}$ for propagation along the [100] and [110] axis respectively.

To facilitate error analysis, the sources of uncertainties in the elastics constants are generally put into two categories, the systematic error and the random error. The systematic error results from the values of λ, θ, n and ρ. The combined uncertainties of these quantities were calculated to be 0.4 % [83]. The random error is attributed to the measured Brillouin frequency shift, which was estimated quantitatively from the variation of θ. The uncertainties of the LA and TA modes were less than 0.2 %, giving an overall error estimate of between 1 – 2 %, determined for the elastic constants.

Chapter 5

Results and discussion : Characterization studies on (a-SiC)

5.1 Introduction

This chapter presents the results observed in the characterization of a-SiC thin films. The theoretical aspects of techniques used in obtaining these results were discussed in chapter three.

5.1.1 Raman Spectroscopy Results

Raman spectrum is, generally, treated as a chemical composition fingerprint tool for different compounds [96]. The obtained spectrum of the analyte can be used as qualitative analysis for unknown samples or a mixture of components. The as-deposited films on sapphire and silicon substrates were examined using this technique. The Raman spectra for the film on sapphire is shown on Figure 5.1. The results obtained show similarities with studies done by Musumeci et al. [97], Sorieul et al. [98] and El Khalfi et al. [99]. Group-theory analysis shows that the Raman-active modes of the wurtzite structure (C6v symmetry for hexagonal polytypes) are the A_1, E_1 and E_2 modes. The A_1 and E_1 phonon modes are split into longitudinal (LO) and transverse (TO) optical modes. In backscattering geometry, the A_1 (LO), E_1 (TO) and E_2 phonons are expected to be seen in the Raman spectra [98]. Relying on these expectations it was possible to identify the broad bands in Figure 5.1 around 200, 500, and 1400 cm^{-1}. They are characteristic of Si-Si (200 and 500 cm^{-1}) and C-C homo-nuclear bonds (1420 cm^{-1}) [98]. The broad peak at 766 cm^{-1} is associated with SiC, theoretically expected to be in the range 700 - 1000 cm^{-1}. The Raman spectra for the film on silicon is shown

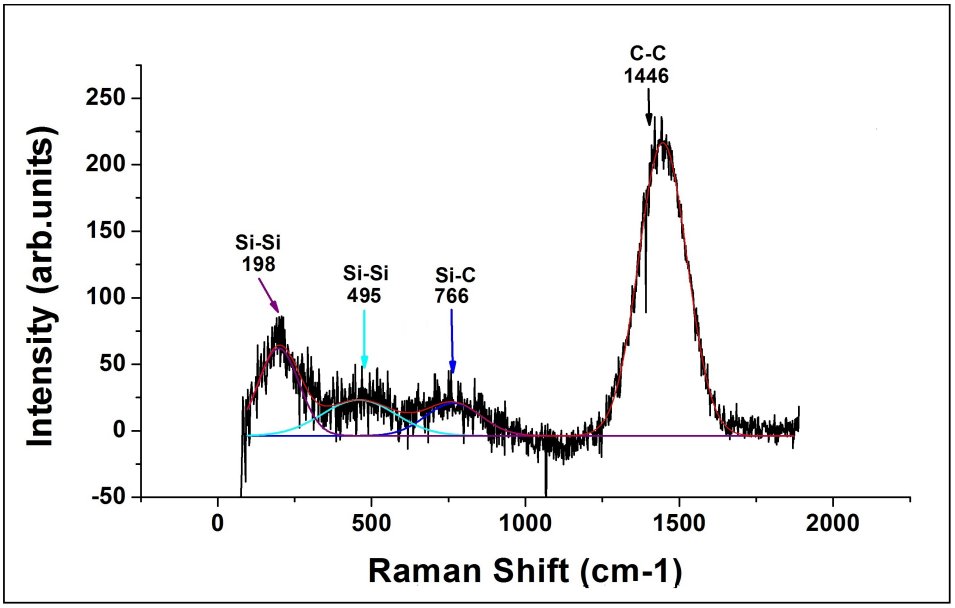

Figure 5.1: Raman spectra of the as-prepared film on sapphire (background subtracted and peak fitted).

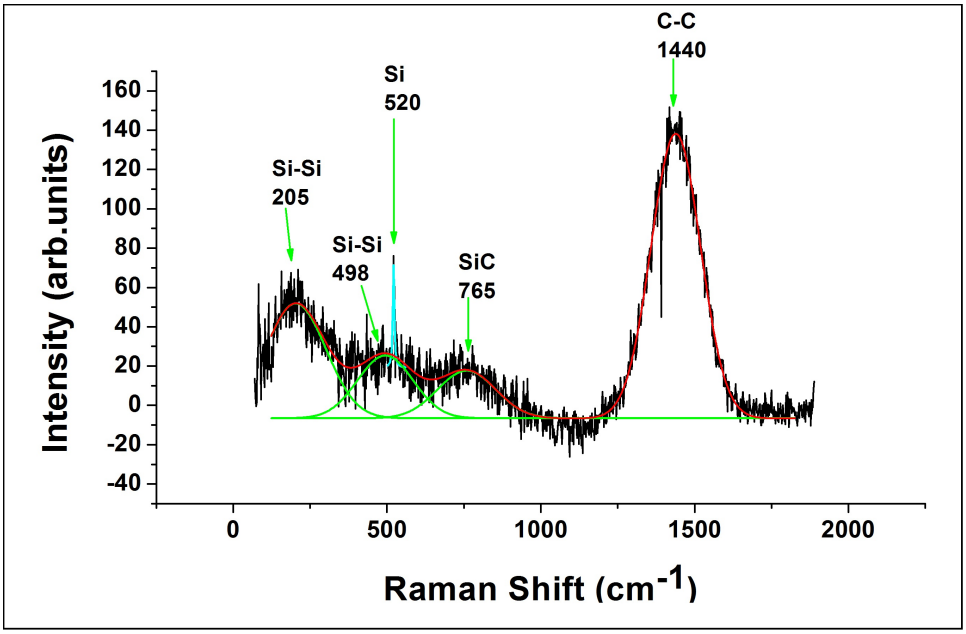

Figure 5.2: Raman spectra of the as-prepared film on silicon (background subtracted and peak fitted).

on Figure 5.2. The spectra shows an additional sharp peak, at 520 cm $^{-1}$, when compared to the spectra of the film on sapphire. The sharp peak is attributed to crystal silicon substrate [99]. Peaks at 205 - 498, 765 and 1440 cm $^{-1}$ correspond to Si-Si, SiC and C-C vibrations as discussed above, respectively.

The Raman analysis confirms that the prepared films in this work were indeed amorphous SiC, the amorphous nature is concluded from the broadness of the peaks. The polytype of these films was taken to be 6H following the polytype

of the target used (examined by Raman spectroscopy). Grazing incidence X-ray diffraction was employed to verify the latter statement.

5.1.2 Grazing Incidence X-ray diffraction (GIXRD) Results

In theory, atoms in amorphous materials are arranged randomly, thus, x-rays incident on atoms in a plane are scattered in a random direction due to the random orientation of atoms and give broad peaks. For this reason the SiC/Si sample was annealed up to 1000 ^oC to introduce order into the system and hopefully get sharp peaks on the x-ray diffraction (XRD) pattern. Figure 5.3 shows the XRD pattern obtained in the Bragg-Brentano geometry. The peaks observed are from the crystalline silicon substrate and from carbon in the film, as illustrated (Figure 5.3). The SiC peaks expected at around 35°, 41°, 60° and 72° [100] are not

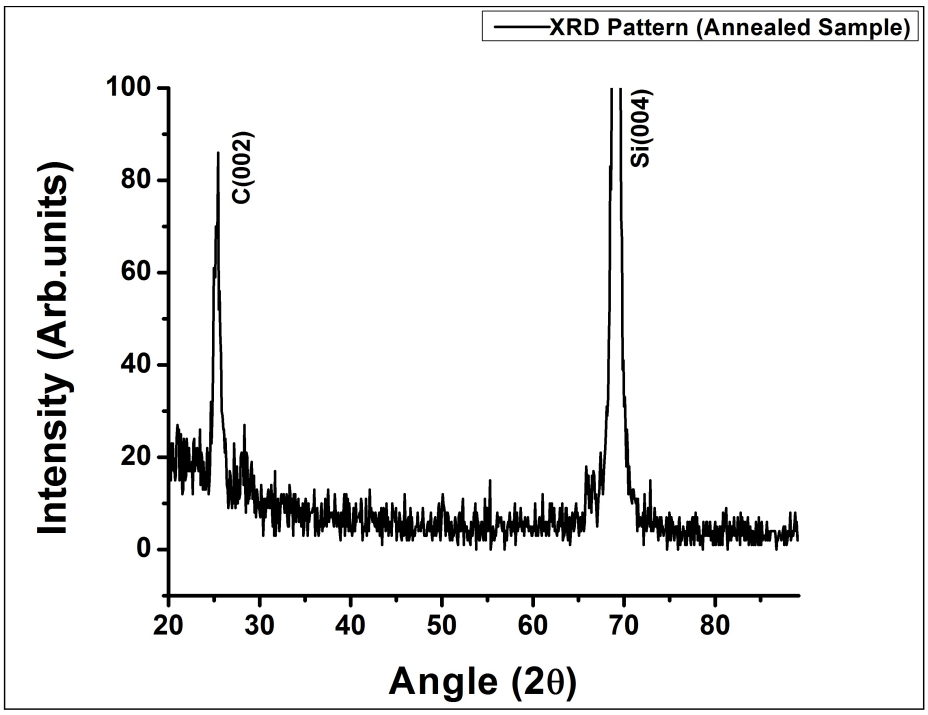

Figure 5.3: Indexed X-Ray diffraction pattern of a-SiC/Si system. Only peaks from Si and C are observed.

visible which may possibly be a result of the limited penetration depth of the x-rays in the Bragg-Brentano configuration and possibly due to the small scattering volume of the crystalline structure. As a result of this observation GIXRD was then employed to probe the surface of a-SiC/Si system. Figure 5.4 illustrates the GIXRD pattern observed. Small reflection signals (red asterisks) were observed and indexed to be elemental carbon (C), from (002) and (101) planes. Peaks from SiC are indexed as shown in Figure 5.4 where the broad peak at around 35° was

identified as a combination of two peaks of 6H-SiC from (101) and (102) planes [101, 102]. With these results, it can be confirmed that the sputtered thin films produced were amorphous 6H-SiC films as evident from the Raman Spectra in Figure 5.5. The broad peak at around 35° suggests, even after annealing up to 1000 ^{o}C the film still possesses some amorphous nature.

The presented Raman range in Figure 5.5 was sufficient for SiC polymorph identification. It was not necessary to do any further characterization techniques on annealed sample since the objective was accomplished (i.e. identifying the polymorph). Also, the interest in this study was on amorphous SiC (because of its ease fabrication methods) not crystallized SiC, hence, not much attention was given to annealed samples.

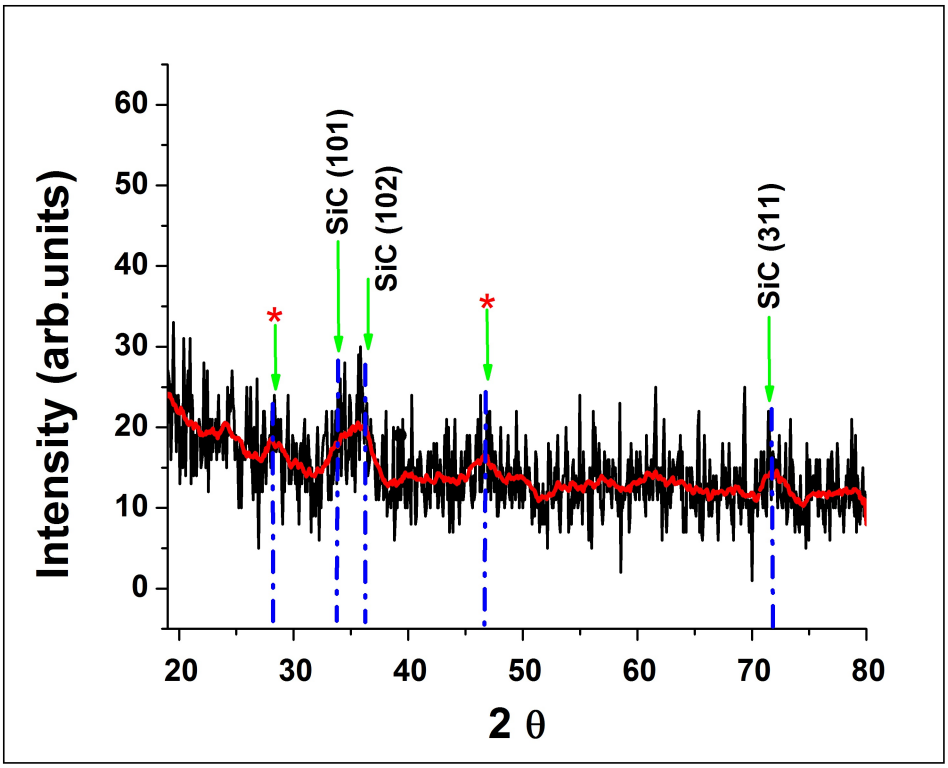

Figure 5.4: Smoothened (Red) and original (black) grazing incidence x-ray diffraction pattern of a-SiC/Si system (incidence angle = 2°). Reflections of C are marked with asterisks.

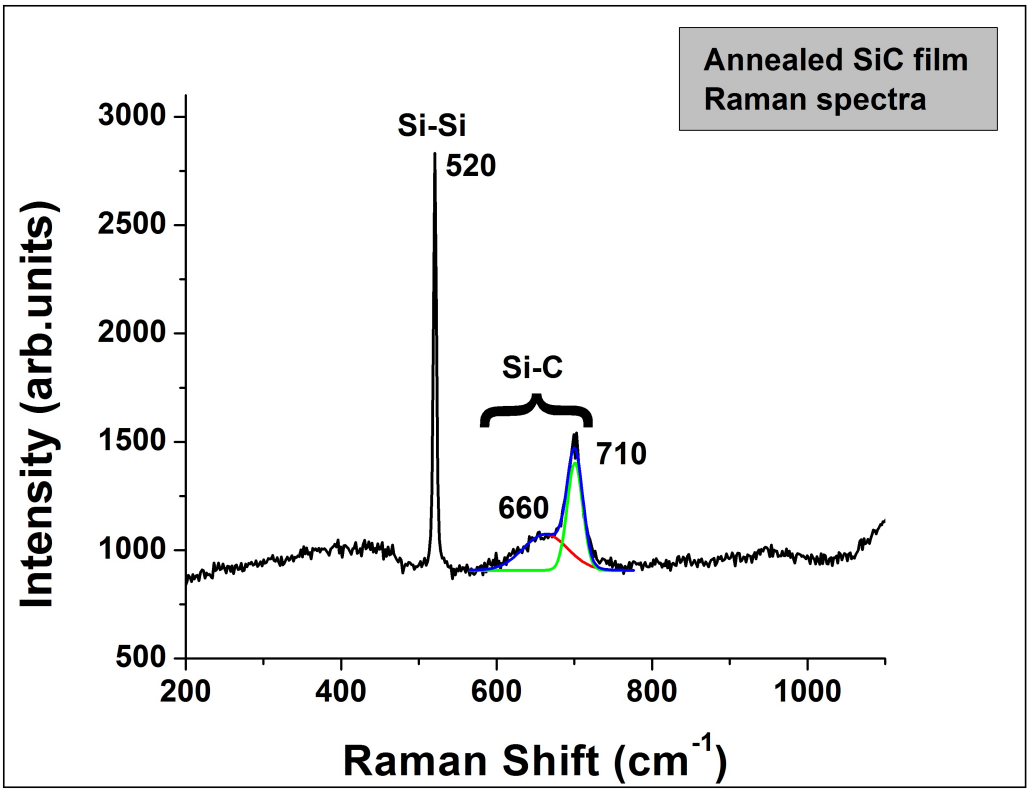

Figure 5.5: Peak fitted Raman Spectra of annealed SiC film. The shift in SiC peaks is attributed to stresses in the film.

5.1.3 X-ray reflectometry (XRR) analysis of SiC thin films

Figures 5.6, 5.7 and 5.8 present the XRR experimental (black line) results and simulations (red dots) obtained from a-SiC thin films deposited on (001) silicon for three, five and seven minutes respectively at 150 W. Simulations of the experimental data were performed using a DIFFRACPLUS LEPTOS 7 software from Bruker AXS.

The extracted average film density (3.01 $\pm$0.05 g cm^{-3}) falls within the range reported by Matsukawa et al. [103]. The thickness of films deposited at three, five and seven minutes were obtained as 36.70, 59.70 and 84.20 $\pm$ 0.50 nm respectively. The errors in XRR measurements are associated with experimental uncertainties in the x-ray optical constants and the uncertainties given by the adopted simulation program such that the uncertainty ranges from 2 - 5.6 %. Using the thickness values obtained for the three different deposition times, namely, three, five and seven minutes, Figure 5.9 was plotted to obtain the deposition rate of a-SiC thin film (12.0 $\pm$ 0.1 nm/min). This rate compared very well to that predicted in section 3.2, to within 0.1 %. The calibration plot was performed to confirm the linear relation of film thickness with deposition time.

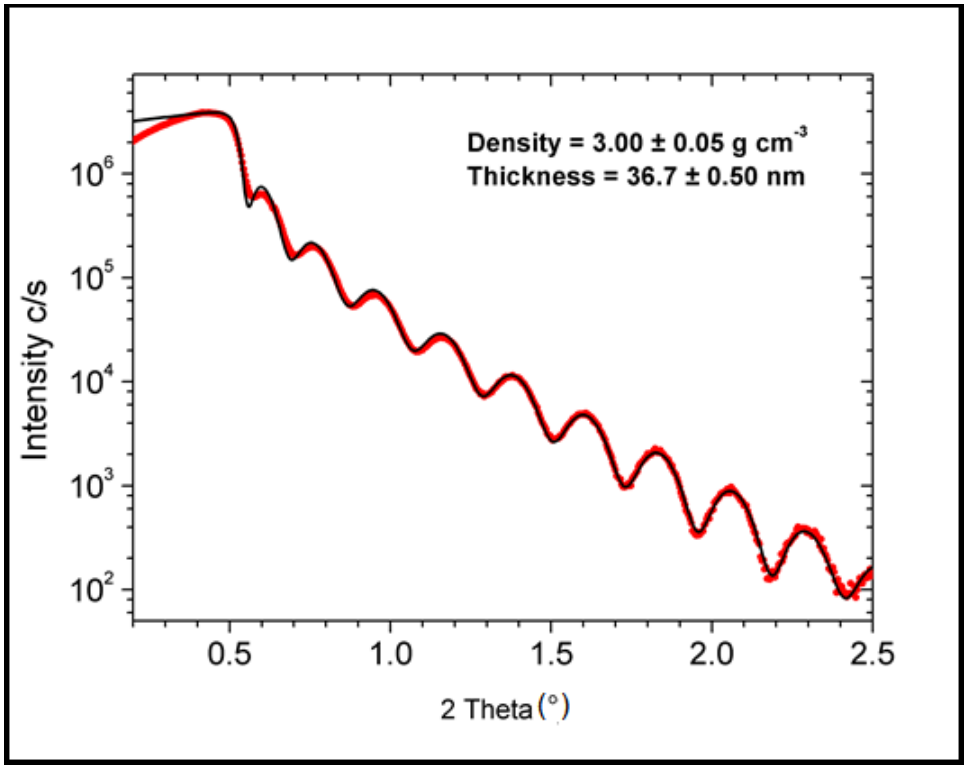

Figure 5.6: X-ray reflectometry pattern of an a-SiC thin film deposited for three minutes on silicon. Black line and red dots are experimental and simulated data respectively.

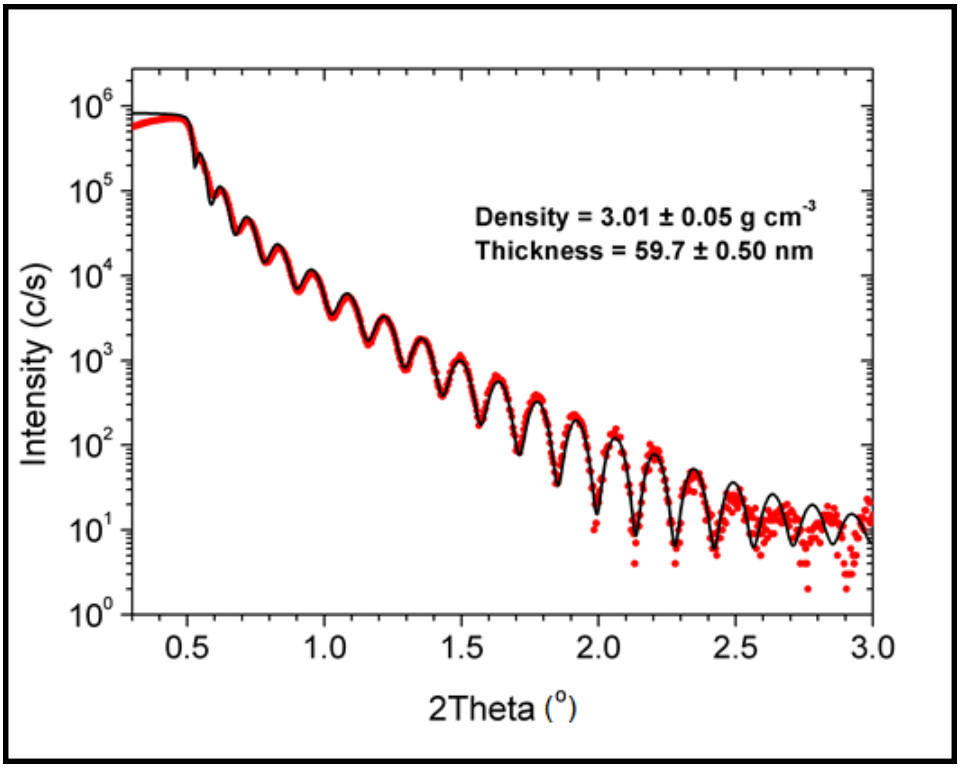

Figure 5.7: X-ray reflectometry pattern of an a-SiC thin film deposited for five minutes on silicon. Black line and red dots are experimental and simulated data respectively.

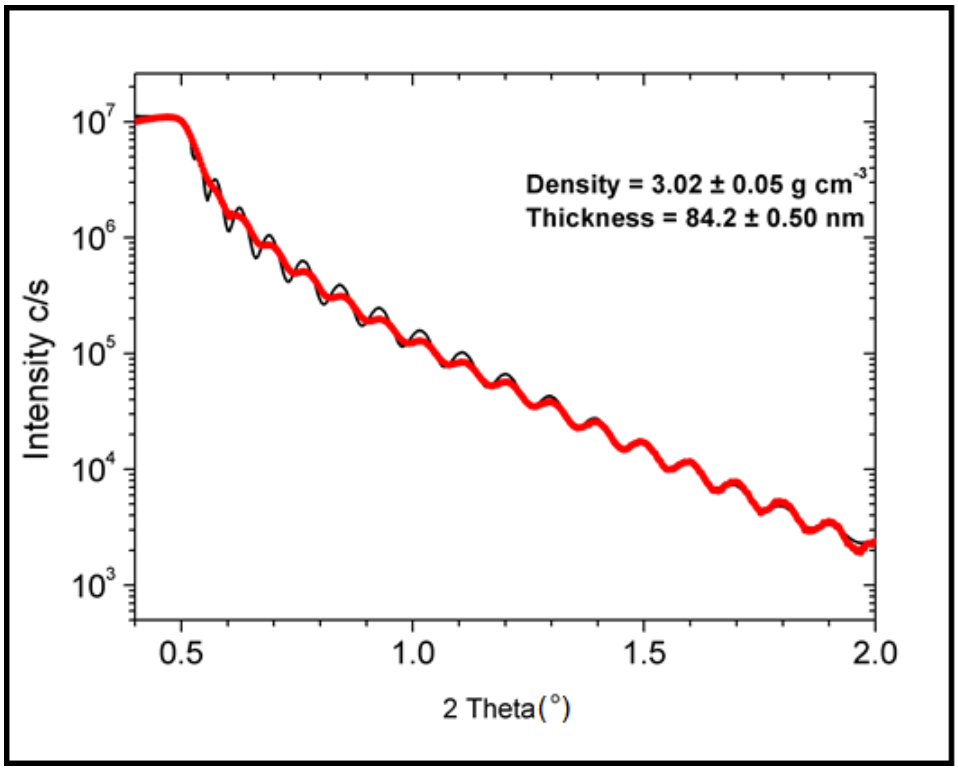

Figure 5.8: X-ray reflectometry pattern of an a-SiC thin film deposited for seven minutes on silicon. Black line and red dots are experimental and simulated data respectively.

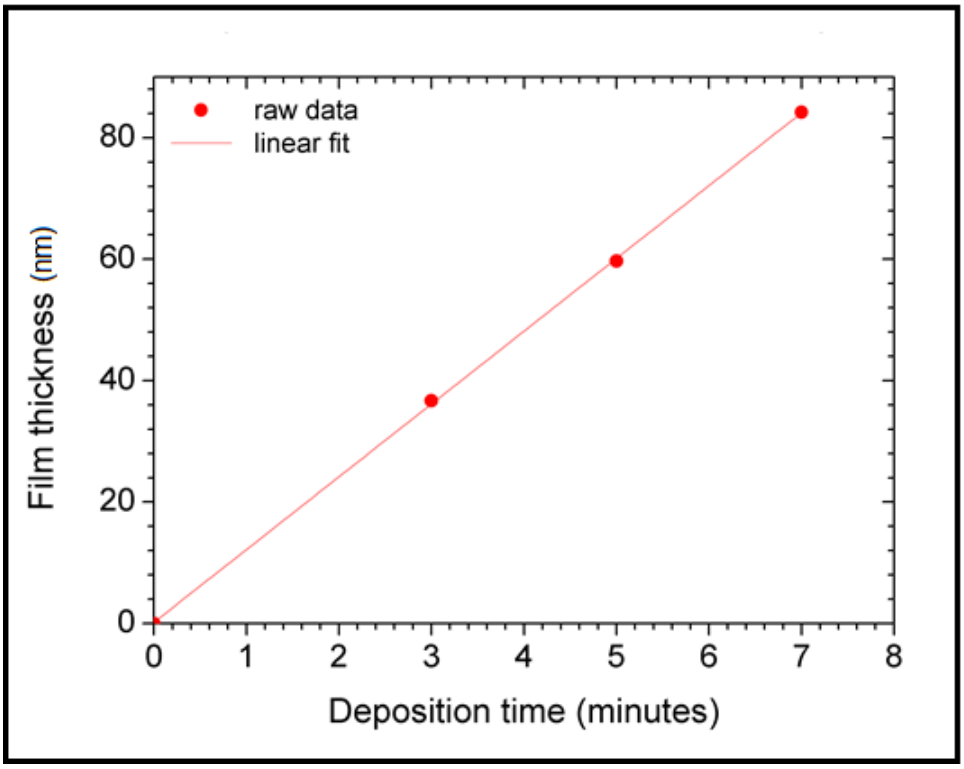

Figure 5.9: Graph of film thickness against deposition time. Deposition rate of 12.0 ± 0.1 nm/min was obtained.

5.1.4 SEM and EDS Results

Figure 5.10 illustrates the image obtained from the cross sectional SEM. The film thickness was measured to an average of 245 nm, for the sample deposited for 20 minutes, as illustrated in the figure. One plane film view SEM image is presented in Figure 5.11, only one image is presented as all other samples appeared the same. Some particles on the film could be evidently seen as labeled in Figure 5.11. Energy dispersive X-ray spectroscopy detector (EDX/EDS) was then employed to determine the nature of these particles and is presented in Figure 5.12. The particles contain Fe and Cr. Si, C, Al, and O also seem to be present in the particles, however, these are attributed to film and substrate compositions. The origin of Fe and Cr could not be pin pointed, it was thought that sample holders contaminated the films since averagely all films had Fe and Cr on their surface and are only 4 % of the film composition. Further EDS measurements were done on films on sapphire and silicon and are presented in Figures 5.13 and 5.14 respectively. Si, C and O are common in all samples as expected. Other elements observed are relatively attributed to respective substrates. The Si:C ratios across samples of same deposition time were 1.0 : 2.3 and 1.0 : 0.6 for sapphire and silicon substrates respectively. Si is higher on films on Si substrate as measured by EDS and this is a result of detection of Si element from the substrate. In general, deposited films in this work are not stoichiometric and are carbon rich with an average Si:C ratio of 1:1.5 as measured from EDS.

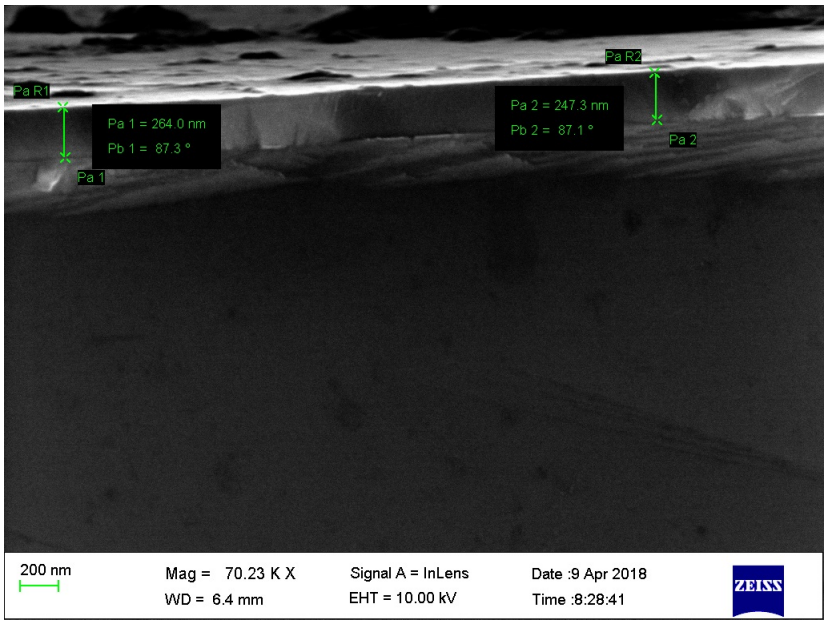

Figure 5.10: SEM cross sectional image showing thickness measurement of as deposited a-SiC film. Deposited for 20 minutes at 150 W rf sputtering power. (Image shows two measurements (264 and 247 nm) of several averaged film thicknesses)

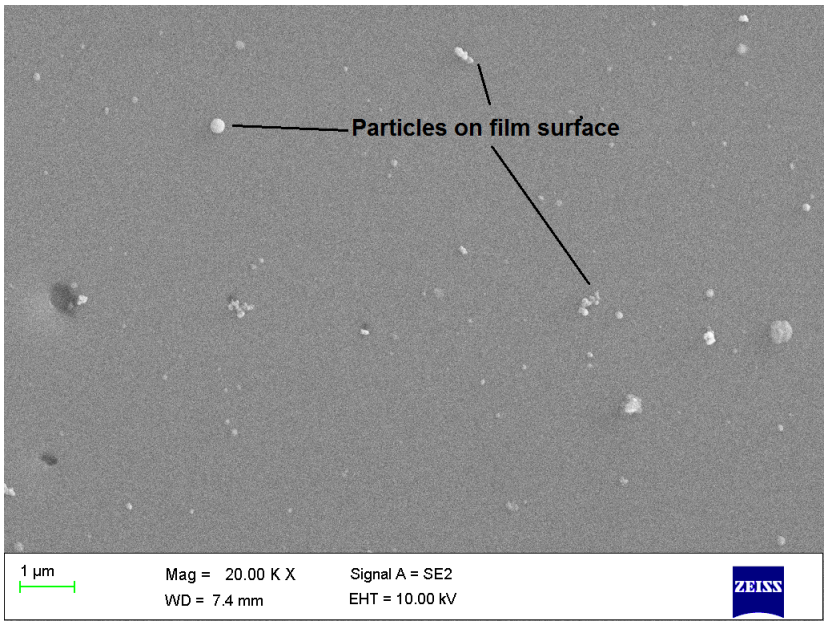

Figure 5.11: General SEM image of the as deposited a-SiC films (the present image is from a film on sapphire(Al_2O_3)). Presence of foreign particles on the film are observed.

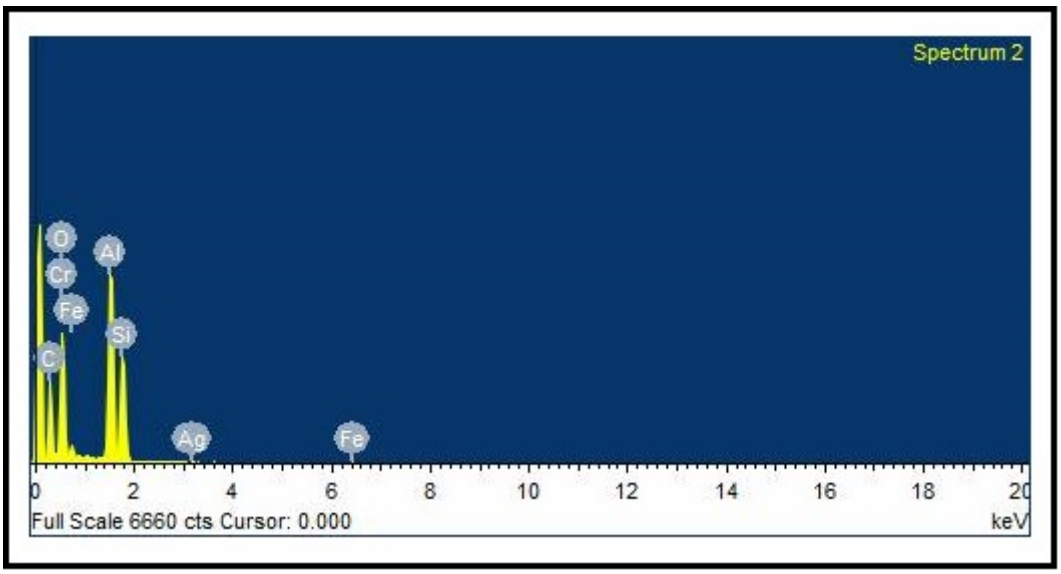

Figure 5.12: EDS spectra showing the elemental composition of the observed foreign particles in Figure 5.11.

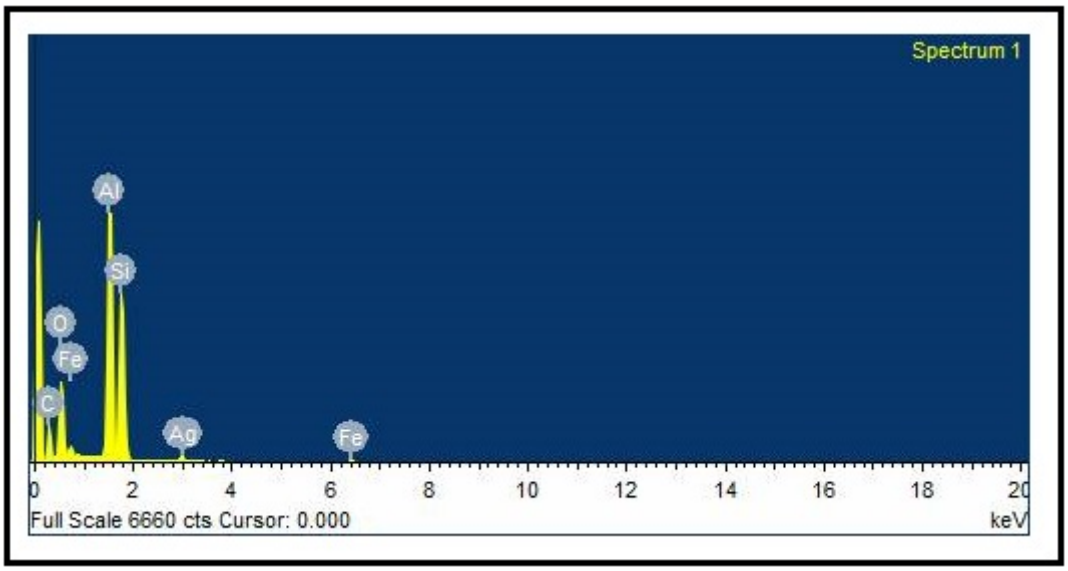

Figure 5.13: EDS spectra showing the elemental composition of as deposited a-SiC thin film on sapphire

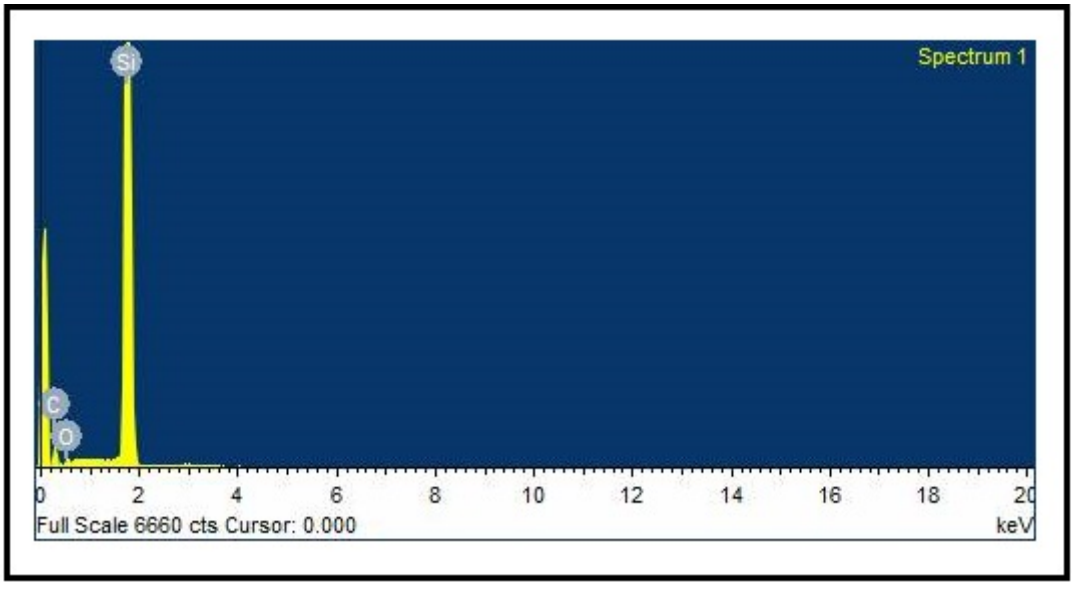

Figure 5.14: EDS spectra showing the elemental composition of as deposited a-SiC thin film on Si

5.1.5 Optical spectroscopy

The results of optical absorption measurements of as deposited a-SiC on sapphire are shown on Figure 5.15. The absorbance appears to be increasing as the film thickness increases. The software for the spectrometer provide absorbance using

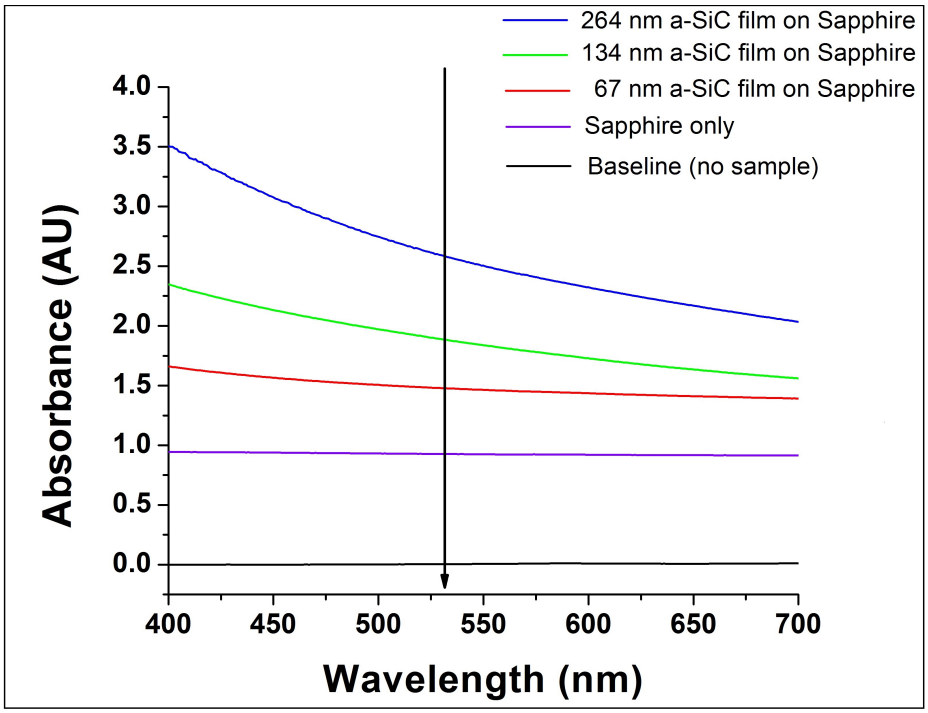

Figure 5.15: Optical absorbance of SiC on sapphire sample. The thickness of the thicker sample (264 nm) was taken from SEM cross sectional images, the other two thickness were deduced from the assumption that the film thickness increases linearly with deposition time. The arrow indicates the SBS laser wavelength at 532 nm.

the convention from the spectroscopy, chemistry, and mineralogy literature (SCM) [104],

$$a_{SCM} = -log_{10}\left(\frac{I_{meas}}{I_o}\right) \tag{5.1}$$

where I_{meas} is the intensity exiting the sample and I_o is the intensity entering the sample (which is obtained by collecting the reference spectrum, shown by the black line in Figure 5.15). Following the latter statement transmission was calculated using $T = I_{meas}/I_o$. The results are tabulated in Table 5.1 and are presented with sapphire substrate effect subtracted.

It is obvious that compared to sapphire substrate only, the SiC/sapphire system has enhanced light absorption (Figure 5.15) with film transmittance lower than 30 % in the region of interest (525 - 550 nm). The latter discussion essentially promotes the surface ripple mechanism (discussed in section 2.2.1) applicable to conditions for SBS experiment. It is therefore concluded that surface ripple

scattering mechanism is the most dominant for this study.

Table 5.1: Table of transmittance measurements at 532 nm relative to a-SiC film thickness..

Film thickness (nm)	Transmittance (%)
0.00	100.00
67.00	28.29
134.00	11.03
263.00	2.49

5.1.6 Rutherford backscattering (RBS) Results

The elemental composition of samples prepared were determined by RBS analysis, in complementation with energy dispersive X-ray spectroscopy (EDX/EDS). The RBS plots were simulated using Rutherford Universal Manipulation (RUMP) software and this enabled to determine layer by layer information on thickness and composition. The RBS spectra and simulations for the as-deposited SiC-Si thin film, samples deposited for five, ten and twenty minutes at 150 W sputtering power are shown in Figures 5.16, 5.17, 5.18 respectively. The arrows indicate the surface channels of observed elements. The spectrum display presence of SiC layer, illustrated by a step labeled 'Si-SiC interface' [105]. The step broadens as the layer thickness increases as shown in Figures below. In theory, FWHM of the peaks observed represent the total energy loss of $4He^{+}$ ion as it penetrates a certain distance of the sample and it is highly utilized in computer simulations. Rump simulations show a thickness of 75, 145 and 270 nm for samples deposited for 5, 10 and 20 minutes respectively. The Si:C atomic % ratio for the 75 and 270 nm samples were 1:2.24 and 1:2.16, respectively, for the sapphire and silicon substrates giving an average composition ratio of 1:2 of as deposited samples. Some impurities of Fe and Ca are also observed on the layer which are less than 2 % in composition of SiC layer. It is assumed that all samples have a layer of SiO_2 just above the Si substrate layer attributed to the natural presence of oxygen and that the samples were deposited at room temperature. The SiO_2 layer was given a thickness of five nm in all three simulated samples. The O peak was not noticeable from the experimental data due to relative signal to noise ratio.

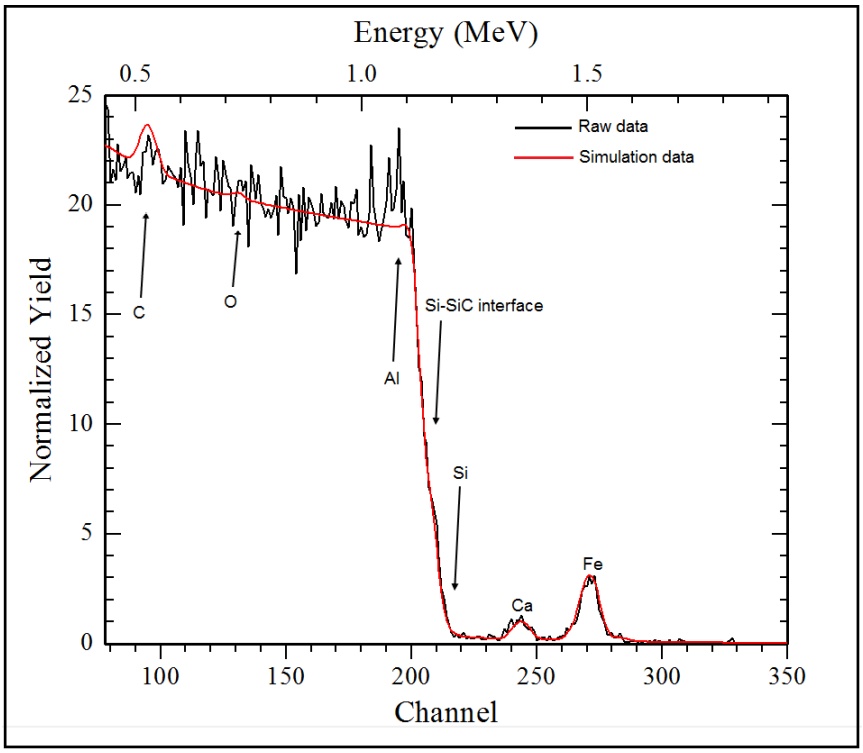

Figure 5.16: RBS spectra for SiC films deposited for five minutes (75 nm) onto silicon substrate. The black and red plots are actual and simulated profiles respectively.

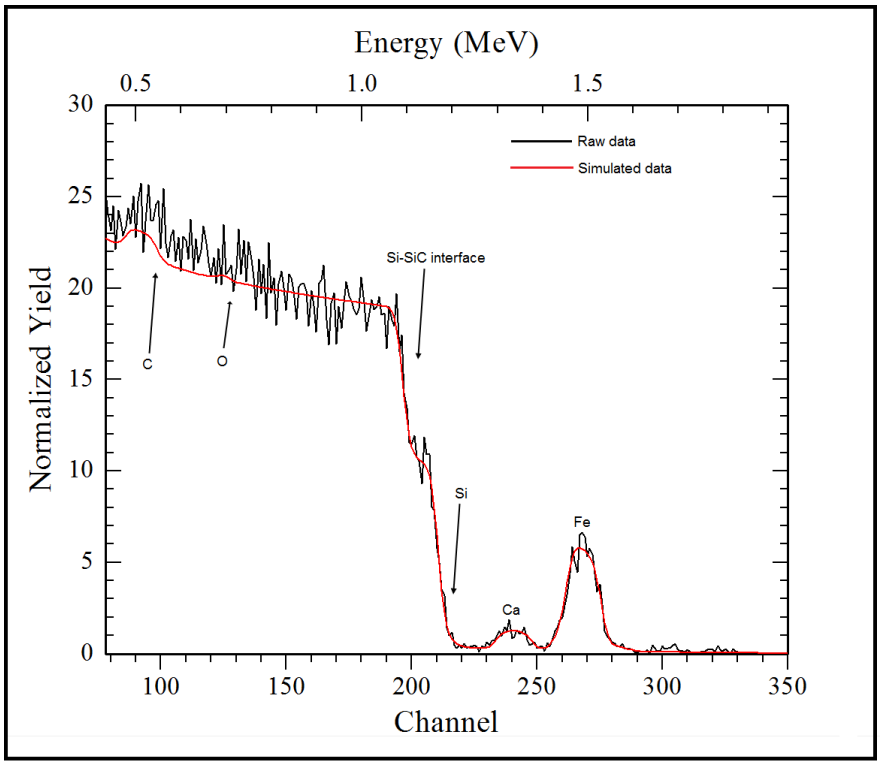

Figure 5.17: RBS spectra for SiC films deposited for ten minutes (145 nm) onto silicon substrate. The black and red plots are actual and simulated profiles respectively.

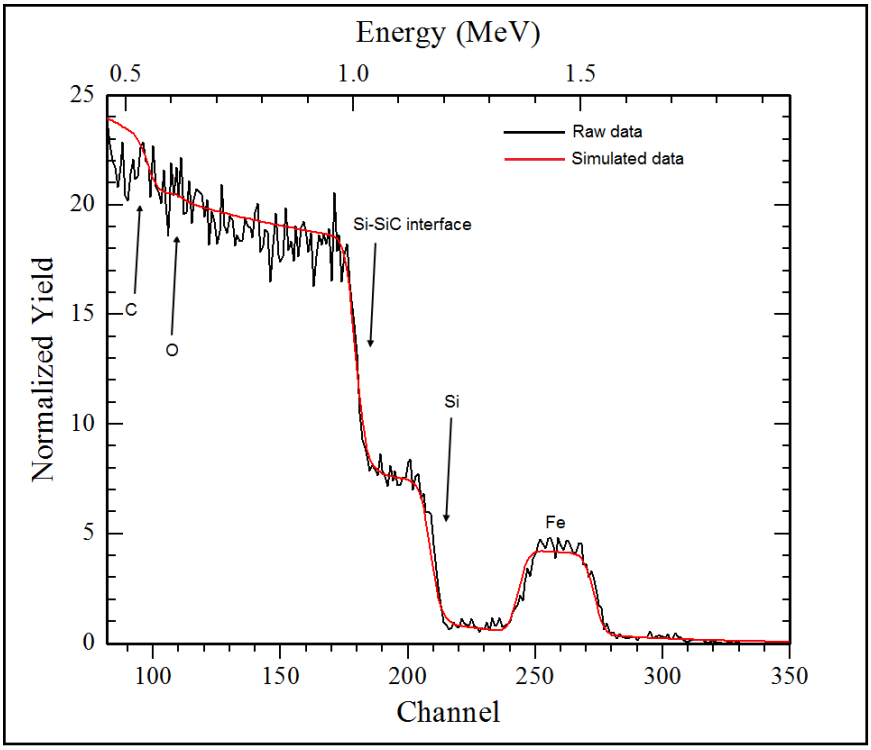

Figure 5.18: RBS spectra for SiC films deposited for twenty minutes (270 nm) onto silicon substrate. The black and red plots are actual and simulated profiles respectively.

5.2 Summary

Chapter five dwelled on the characterization of deposited thin films. Raman and GIXRD confirm that films were amorphous SiC belonging to the 6H polytype. Electron images from the SEM show a general uniform growth of the thin film. EDS and RBS measurements gave relatively similar Si to C ratios on the film taking into account the different probing particles used in respective techniques, namely, x-rays and $4He^{+}$. Knowing the nature of our films, the next step was to probe their elastic constants using surface Brillouin scattering spectroscopy which is presented in chapter six.

Chapter 6

Surface Brillouin scattering studies on SiC films

6.1 Introduction

Due to SiC mechanical and electronic properties, discussed in chapter one, the material has gained applications in microelectronic and optoelectronic devices (solar cells [106–108], light emitting diodes [109], photo-transistors [110, 111]). Full set of elastic constants for a number of different polytypes of bulk, crystalline SiC were first determined by SBS by Kamitani et al. [112].

In this chapter the dynamics of surface acoustic waves in SiC thin films are presented. In order to investigate the influence of the substrate, the present study compares the elastic properties of amorphous SiC films deposited on silicon and sapphire substrates (preparation and characterization of samples are discussed in chapters three and five respectively). Surface Brillouin spectroscopy, discussed in chapters two and three, is employed to study the elastic properties of the films. The chapter ends by comparing the slow-film/fast-substrate and fast-film/slow-substrate systems.

6.2 SBS on a-SiC films on Sapphire substrate

In this study the interesting case of two transparent media: SiC films supported by sapphire (Al_2O_3) substrate was investigated. The latter statement suggested that Brillouin spectra obtained for such a case involves both scattering mechanisms discussed in section 2.2.1. However, the results from transmission measurements in section 5.1.5 show that the ripple scattering is more dominant. A similar system was first studied by Nizzoli et al. [27] on polycarbonate films supported by Pyrex substrate. In their study it was found that in general the ripple scattering from

the transparent surface gave rise to the dominant term. The elasto-optic effects of the film are thickness dependent and were by no means negligible and sometimes were even the largest. Conversely the ripple term of the film-substrate interface and the elasto-optic term of the substrate were small and did not appreciably affect the cross-section.

The data reported here first incorporates Brillouin measurements for bulk (elasto-optic) scattering carried out on sapphire substrate and this was done for baseline referral to identify changes that occur after an a-SiC film deposition. Figure 6.1 shows the measured Brillouin spectra of sapphire substrate and of SiC thin film on sapphire at 70° laser incidence. The Brillouin spectra on a-SiC/sapphire were collected for twelve hours each from a laser with 240 mW power on sample. The spectrum shows Stokes and anti-Stokes sides, the peaks of the Rayleigh mode (SAW) and of bulk modes. The difference between the spectra, shown in Figure

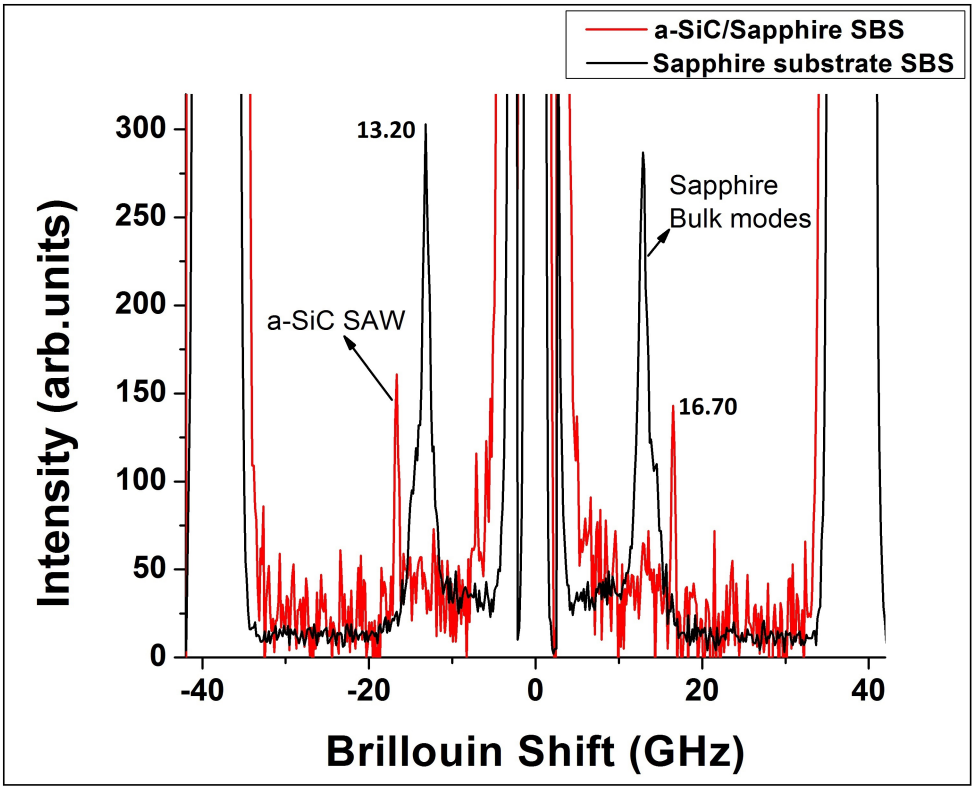

Figure 6.1: Brillouin spectra showing bulk modes on sapphire substrate (black) and surface modes on a 270 nm thick a-SiC film on sapphire (red). Both spectra were taken at laser incident angle of 70°.

6.1, can clearly be noticed, bulk modes that appear on the spectra of sapphire substrate are not visible after a 270 nm a-SiC film has been introduced. To ascertain the identification of the peak observed in the red spectra (a-SiC SAW in Figure 6.1) Green's function (section 2.2.2) was used to calculate the theoretical SBS cross-sectional spectra, shown in Figure 6.2. The Rayleigh surface acoustic

wave (RSAW) of the calculated spectra, for same incident angle, falls within the range (14 - 17 GHz) of the experimental RSAW.

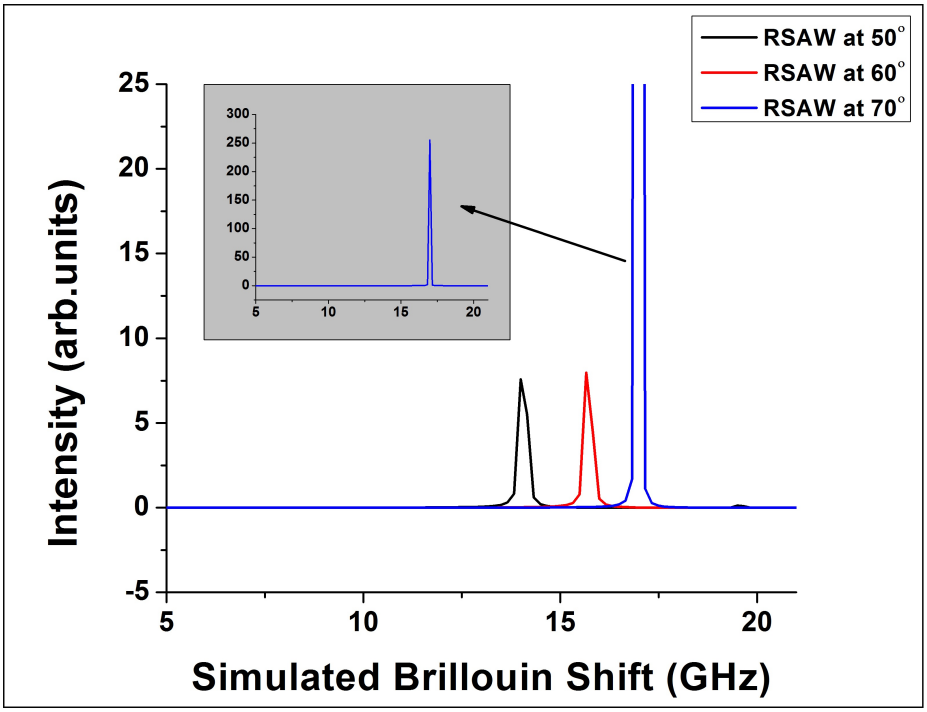

Figure 6.2: Green's function cross-section Brillouin spectra (anti-Stokes side) for a 270 nm thick a-SiC thin film on sapphire, calculated for a range of incident angle (50° - 70°). The simulation was calculated using 60 % of bulk single crystal 6H-SiC elastic constants (c_{11} and c_{44}) reported by Kamitani et al. [112]. In most cases, thin film elastic constants are 60 % of their bulk elastic constants, hence, this estimation [113].

For thinner films, about 145 nm, it was a challenge to identify the SAW modes against the backdrop of the bulk modes. As a result of this predicament, it was necessary to vary laser incident angle, as discussed in section 2.2.1, to identify the nature of modes observed in the a-SiC/Sapphire Brillouin spectra. It should be noted that modes from the sapphire substrate are visible on the a-SiC/sapphire spectra and this is a consequence of some degree of transparency of SiC thin film at 532 nm wavelength. Figure 6.3 shows an SBS spectra of 145 nm thick a-SiC film on sapphire, showing symmetric frequency positions of the observed modes. Tracking the labeled modes as the incident angle was varied gave plots shown in Figure 6.4 and 6.5. According to the discussion in section 2.2.1, bulk modes whose velocity is given by $v = f\lambda/2n$ (n being the refractive index of the material) are not affected by the variation of incident angle as shown by peaks B and C in Figure 6.5. Surface modes (Peak A in Figure 6.4) are linearly affected and the velocity (4062 m/s) of the SAW was calculated from the slope ($2v/\lambda$) of the graph in Figure 6.4 obtained from equation 2.34, $v = f\lambda/2\sin\theta$, where f is

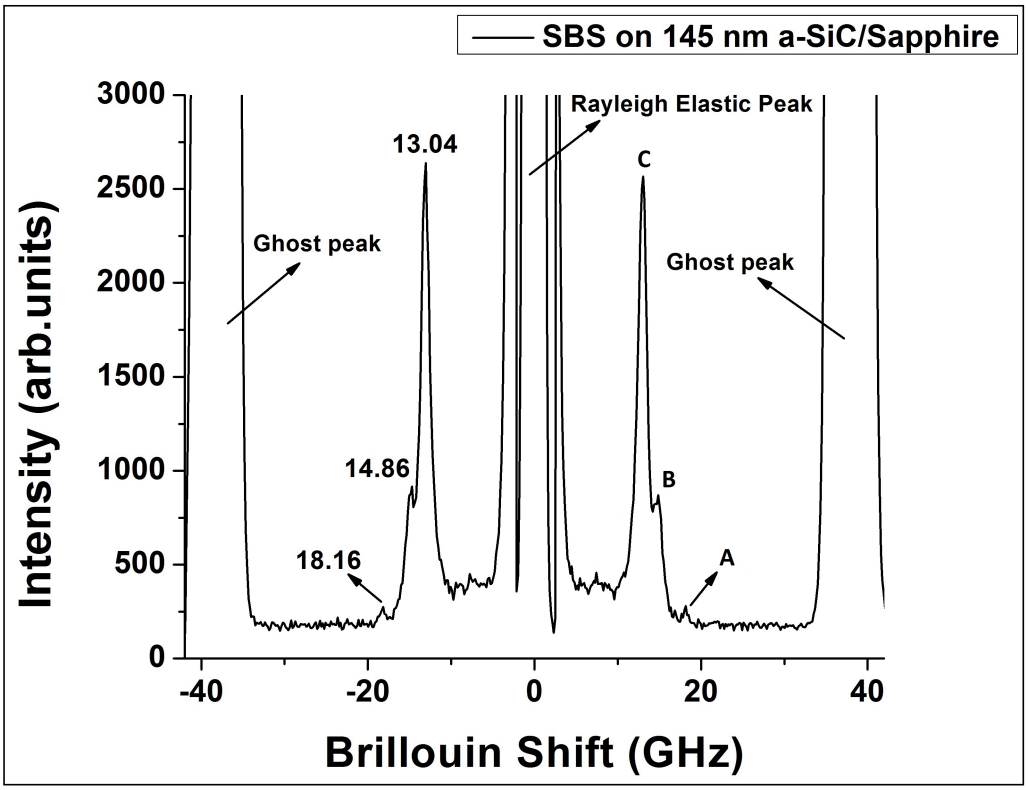

Figure 6.3: SBS spectra for 145 nm thick a-SiC thin film on sapphire, taken at laser incident angle of 70°.

the Brillouin shift frequency of the SAW and θ is the incident angle of light from the normal direction of the sample. The SAW velocity, 4062 m/s, falls within the range reported by Matsukawa et al. [103]. At $\theta = 30^o$ the SAW could not be easily identified because of the peak to noise ratio.

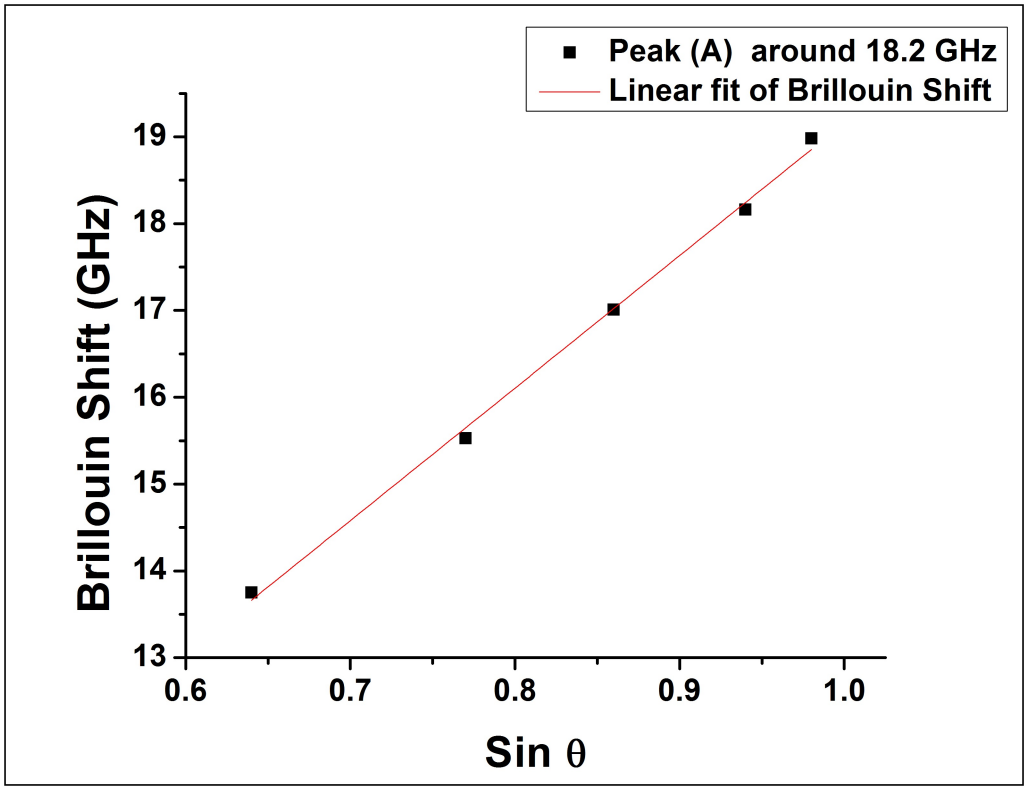

Figure 6.4: Frequency dispersion curves of Peak A as the incident angle is varied from 30° to 80°.

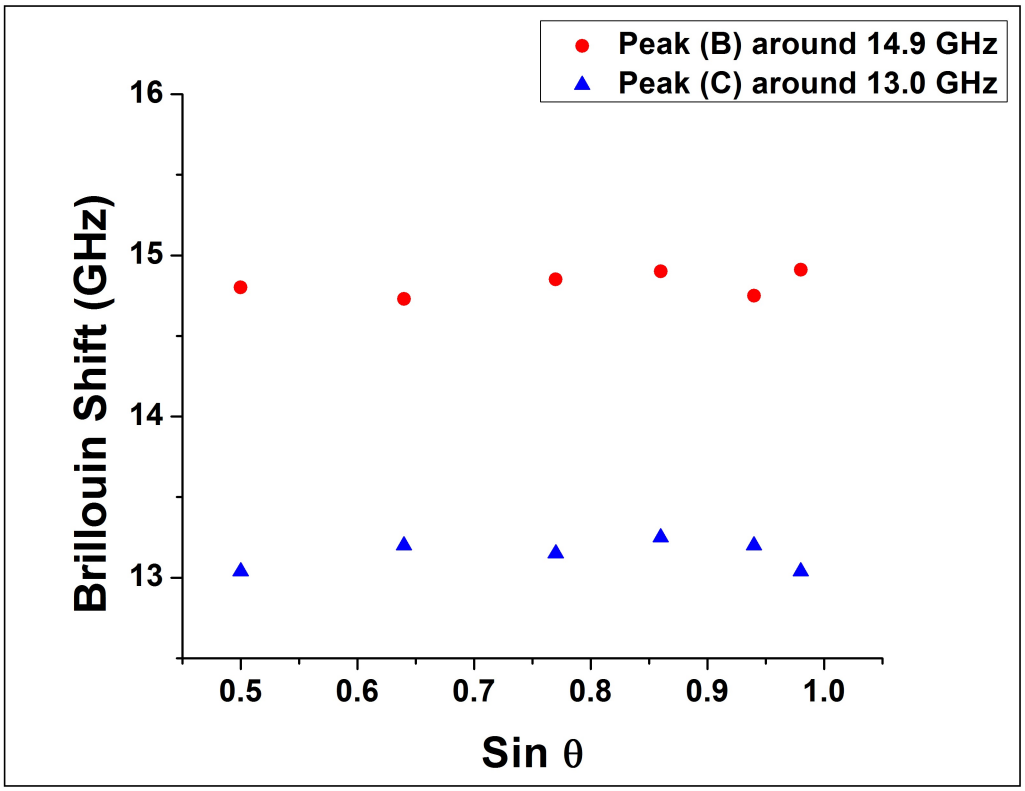

Figure 6.5: Frequency dispersion curves of Peak B and C as the incident angle is varied from 30° to 80°.

6.2.1 Extraction of effective elastic constants of a-SiC thin films

To recover elastic constants from phonon velocities the underlying continuum mechanical model implies the integration of the equation of motion, discussed in section 2.1.2 and discussed in detail by Farnell and Adler [49]. In homogeneous films it was found that the sound velocities of localized modes only depend on the product of $q_{||}$ and the film thickness h [49]. The dispersion of acoustic velocity is examined by varying the dimensionless product $q_{||}h$. As stated by equation 2.32, $q_{||}$ depends on the laser light incidence angle θ. In this work, sin θ was varied from 0.5 to 0.98. This range was narrow to obtain enough information to extract elastic constants, hence, it was necessary to examine films of different h to obtain a wide range of $q_{||}h$ of the dispersion curve. As mentioned in chapter two, all films were deposited under identical conditions, therefore, the combined dispersion curves of the surface wave modes were continuous and were expected to relate to a single set of elastic constants. By means of a least-squares minimization fitting (to the velocity dispersion curves of the system (v vs. $q_{||}h$)) governed by

$$\chi^2 = \sum_i \left(V^i_{cal} - V^i_{meas} \right)^2, \tag{6.1}$$

the method of elastodynamic Green's functions was applied to the film on a substrate system inorder to extract the film's elastic constants. V^i_{cal} and V^i_{meas} are the calculated (determined by Green's function) and measured velocities (determined from the spectra) respectively. The calculations are based on the input values of the elastic constants c_{11}, c_{12}, and c_{44} [114].

Figure 6.6 shows the calculated and experimental dispersion of the surface waves. The waves were detected in a $q_{||}h$ range between 2 and 8 by varying the incidence angle from 30° to 80° as well as using films of different h. The uncertainties in film thickness evaluations are represented by horizontal error bars. The errors in the acoustic velocity is due to uncertainties in determination of peak positions and it is represented by vertical error bars. The experimental dispersion curve shows good agreement with the calculated curve, except for position of transition between film thicknesses where two outliers are observed. Figure 6.6 also demonstrates that only the Rayleigh mode is observed at all laser incident angles from a-SiC/sapphire Brillouin spectra ran for twelve hours each. The Sezawa mode was, however, only observed at laser incident angle of 80 ^{o} on a 145 nm a-SiC film. It should be noted, however, that more Sezawa modes were expected since the current system is an elastically soft film on hard substrate [113]. It was concluded that these modes were not observed as a result of too small scattering

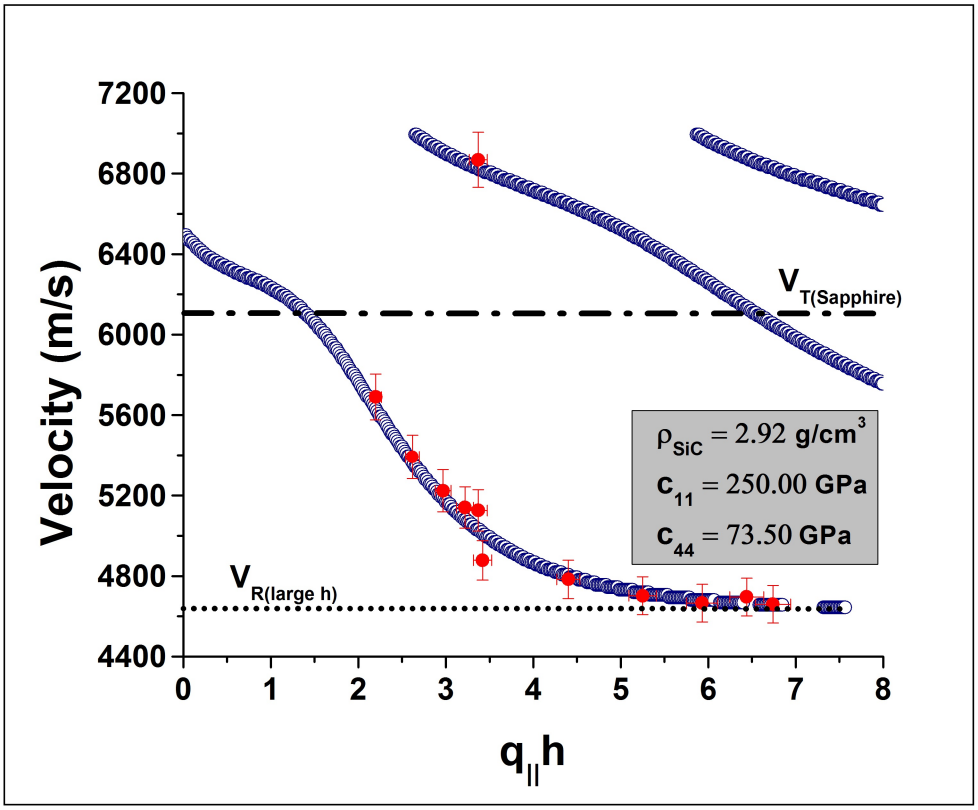

Figure 6.6: Dispersion curves of two samples with thicknesses h of 145 and 270 nm. Noticeably, only the Rayleigh mode is observed in the spectra of each sample and are plotted (combined). A Sezawa mode is observed once on the 145 nm sample at 80° incident angle. Experimental and calculated dispersion plots are shown in red and blue circles respectively.

cross section. The Rayleigh wave velocity of the film is seen to be close to that of sapphire at small film thickness and gradually decreasing and gets constant (4 644 m/s) at large film thicknesses. The film elastic constants which correspond to the best fit in Figure 6.6 are c_{11} = 250.00 GPa and c_{44} = 73.50 GPa, the density (3.00 g/cm^3) of the films obtained from XRR measurements was used. These values are half of those reported by Kamitani et al. [112] on bulk single crystal 6H-SiC, the difference in values is attributed to film and amorphous nature of samples in this work.

6.3 SBS on a-SiC films on Si substrate

The present study looks at transparent a-SiC films on opaque Si, which is a different system as of the previous study. However, as discussed in previous sections, the most dominant Brillouin scattering mechanism is the ripple mechanism and it is most enhanced in this system following the opaqueness of the substrate. As a consequence of opacity of Si, modes from the substrate were not expected. Sample

preparation and characterization were discussed in chapters three and five. Figure

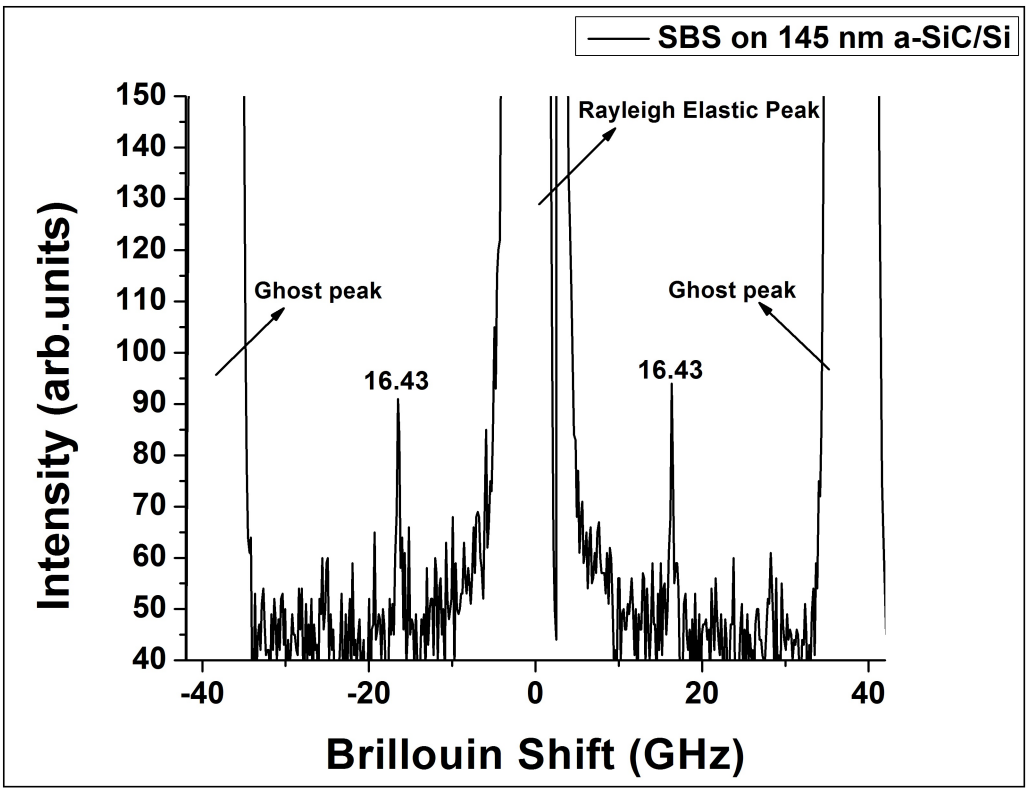

Figure 6.7: Typical SBS spectra for 145 nm thick a-SiC thin film on Si, taken at laser incident angle of 70°. The Rayleigh mode of the film is observed at 16.43 GHz.

6.7 illustrates the Brillouin spectra on a 145 nm a-SiC film on Si.The spectra was collected at laser incident angle of 70° for twenty four hours at 640 mW laser power. It would be noticed that Brillouin spectra acquisition times for films on Si and Sapphire were different as a result of their respective optical properties. Silicon is a weak light scatterer compared to sapphire, hence more acquisition time and more laser power was needed with Si substrates.

6.3.1 Extraction of effective elastic constants of a-SiC thin films

As was done in the previous study on a-SiC/sapphire, the method of elastodynamic Green's functions was applied to extract the film's elastic constants by least-squares minimization fitting to the velocity dispersion curves of the system (v vs. $q_{||}h$). The dispersion of surface waves was detected in a $q_{||}h$ range between 0.6 and 8 by using films of different thicknesses (70 - 270 nm) deposited under similar sputtering conditions as well as by varying the angle of incidence from 30° to 80°. The combined results of these measurements are shown in Figure 6.8. For

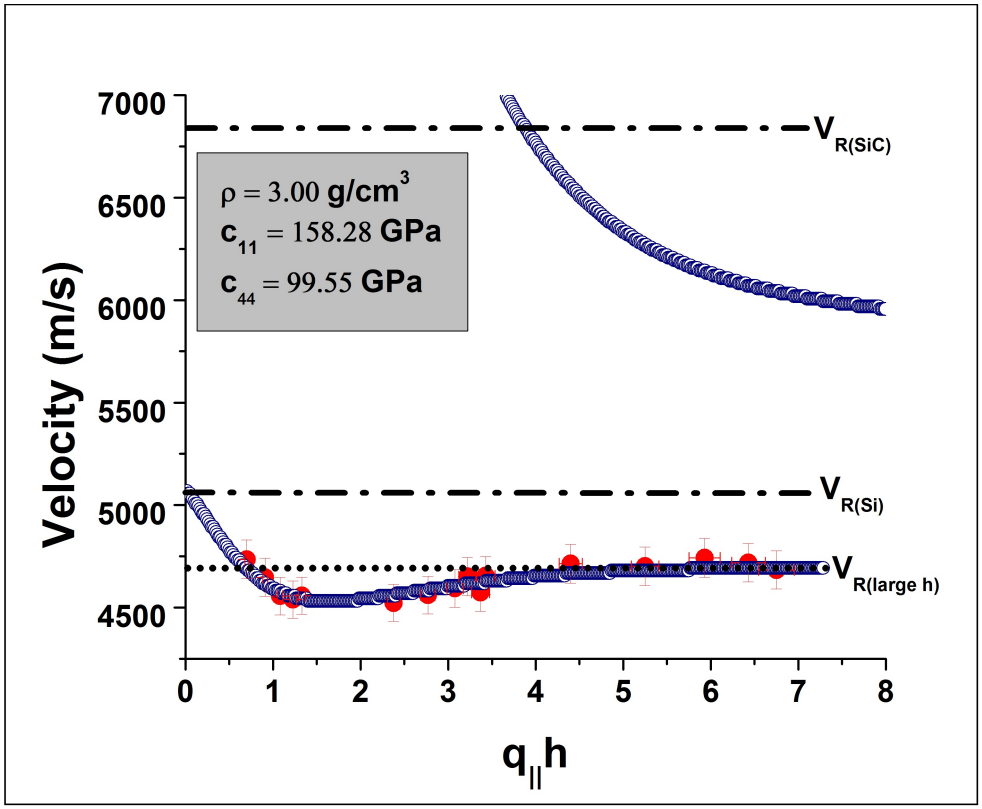

Figure 6.8: Anomalous dispersion curves of a-SiC on Si substrate. Three samples with thicknesses h of 70, 145 and 270 nm were used to construct the dispersion plot, and noticeably only the Rayleigh mode is observed consistently. Experimental and calculated dispersion plots are shown in red and blue circles respectively.

an elastically hard film on an elastically soft substrate, as is in the current study, Sezawa modes are not observed [113], only the Rayleigh mode is present as was illustrated in Figure 6.7. An anomalous dispersion profile is observed, where the Rayleigh mode of the film is near to that of the substrate at low film thicknesses and gradually decreases and becomes constant as the film gets thicker. Appearance of anomaly effects depends on whether [$H = (\rho_f/\rho_s)/(V_{Rf}/V_{Rs})$] is greater or smaller than unity, ρ_f and ρ_s are film and substrate densities and V_{Rf} and V_{Rs} are Rayleigh velocity of film and substrate respectively. Parameter H quantifies the effects of loading with respect to velocities. When $H < 1$, as in the SiC/Si case, the velocity effects is greater than the loading effect. Hence, dominating the anomaly behavior leading to the reduction and/or elimination of the decrease that should be observed, as in the SiC/Si case. The Rayleigh mode velocity gets constant as it approaches the velocity of bulk a-SiC 4 694 m/s. The film elastic constants which correspond to the best fit in Figure 6.8 are c_{11} = 158.28 GPa and c_{44} = 99.55 GPa, the density (2.92 g/cm^3) of the films obtained from XRR measurements was used.

6.4 Summary

A series of Brillouin spectra have been measured for amorphous SiC films formed by RF magnetron sputtering from a SiC target to respective substrates, silicon and sapphire. Films on sapphire, in addition to Rayleigh mode, showed an additional mode at high frequencies (25 GHz) relative to the Rayleigh mode frequency around 18 GHz. This peak was observed only at large scattering angles (80°), hence, it was only observed once. The measured and calculated dispersion curves of the Rayleigh and Sezawa modes were presented, and show that for small values of $q_{||}h$ gave an SBS spectra close to that of crystalline Si. In large values of $q_{||}h$, the Rayleigh mode velocity tended asymptotically to a constant value of 4 644 and 4 694 m/s for films on sapphire and silicon respectively. These values compare very well with SBS results by Matsukawa et al. [103], measured on thin (45 nm) SiC films deposited on Si, with an average of 4 669 m/s which is the phase velocity of the Rayleigh wave on the surface of bulk amorphous SiC. Cros et al. [115] reported the phase velocity of the Rayleigh wave of a-SiC films on Si to be 5 207 m/s, giving a difference of 538 m/s to this work's findings. The discrepancy is attributed to different film growth, film thicknesses and elastic constants probing techniques. The analysis of positive dispersion curves of thin SiC/substrate combinations characterized by stiffness effect showed the appearance of anomalous behavior in a range of small normalized thickness. Thus, the evolution of the dispersion curves are not only influenced by velocity but also by densities (loading effects). The constant c_{11} has no significant effect on the Rayleigh wave velocity, however, it was determined with rather high accuracy on the film on sapphire because of the presence of Sezawa wave which has an appreciable longitudinal component which affects c_{11}. c_{11} was found to be lower on the film on Si (fast on slow system) than that on sapphire (slow on fast system) by 92 GPa and c_{44} was higher on film on Si (fast on slow system) than that on sapphire (slow on fast system) by 26 GPa. Thus, elastically hard substrates (compared to film) promote growth of films with high c_{11} and low c_{44} compared to films grown on elastically soft substrate.

Chapter 7

Conclusion and future work

In this dissertation, SBS has shown to be a effective technique to probe the elastic properties of transparent bulk and semi-transparent thin films. Work on transparent bulk material was done on cubic crystal SrF_2 (chapter four) and presented in a paper titled; "Elastic stiffness coefficients of single crystal SrF_2 by Brillouin light scattering". The elastic constants of RF magnetron sputtered amorphous SiC films deposited on silicon and sapphire substrates were studied at room temperature using Brillouin scattering spectroscopy.

Physical film characterization using Raman spectroscopy, SEM, EDS, GXRD, XRR, RBS and optical transmission were performed. Raman spectra for all as deposited films showed corresponding bands of amorphous SiC, C and Si. Si-Si and C-C vibrations confirmed existence of homonuclear bonds within the SiC network. The relative percentage of Si in the Si_yC_z compound was obtained with the aid of RBS characterization supplemented by EDS measurements and all films showed not to be stoichiometric with a Si:C average ratio of 1:2. The thickness of films were measured using SEM images, RBS and XRR experimental simulations. RBS spectra simulations were done using OMDAQ-3 and XRump softwares. SEM also revealed foreign particles on the films which were also detected by RBS and identified accordingly. GXRD complimented Raman measurements in confirming the 6H-SiC polytype nature of the as deposited films. XRR gave information on film surface roughness and measured the film mass density. Film transmittance properties were investigated using the optical spectroscopy and films were found to be more opaque than transparent.

A series of Brillouin spectra were measured for a-SiC films on sapphire and silicon. Rayleigh SAW were observed in all spectra. Due to the small scattering cross-section the expected Sezawa mode/s on the film on sapphire were not visible in small laser incident angles, however, it was only observed at higher angles. A Green's function method, probing the surface ripple mechanism for the inelastic scattering of light, was used to interpret the experimental spectra. Effective elastic

constants c_{11} and c_{44} were determined for the films on silicon and on sapphire which were presumed isotropic. The substrate effect on effective elastic constants was established from comparing obtained values on films on silicon and those on sapphire. Both systems showed the Rayleigh wave to be dispersing asymptotically to an average constant value of 4 669 m/s which is the phase velocity of the Rayleigh wave on the surface of the bulk a-SiC and it is within a few percent to the values reported by Cros et al. [115]. The constant c_{11}, showed little effect on the Rayleigh wave velocity, however, in theory, it could be determined with high accuracy on the film with Sezawa wave (film on sapphire) owing to its appreciable effect on the longitudinal component. The effective elastic constants extracted by a least squares fitting procedure were $c_{11} = 158.28$ GPa and $c_{44} = 99.55$ GPa for a-SiC/Si films and $c_{11} = 250.00$ GPa and $c_{44} = 73.50$ GPa for a-SiC/sapphire. The values are higher than those of their counterpart bulk silicon $c_{11} = 165.7$ GPa and $c_{44} = 79.6$ GPa reported by Farnell and Adler [49], however, as expected, lower than those of bulk 6H-SiC reported by Kamitani et al. [112], $c_{11} = 501$ GPa and $c_{44} = 163$ GPa. The film values are approximately half of the bulk values.

The important role played by density relation between substrate and film on determining whether a system is a slow on fast or fast on slow was highlighted. Effective elastic constants of as deposited a-SiC films prove to be more superior to their silicon contenders, therefore, are more suitable to be used in MEMS applications.

Future research may be done in the following areas:

1. It would be interesting to investigate the dependence of elastic constants on temperature changes.

2. To use different deposition techniques and make more stoichiometric films and compare their elastic constants with these of the present work.

3. Annealing of the samples to get a more ordered system with the hope of improving on the elastic constants.

4. It would be interesting to use the density functional theory (DFT) to extract elastic constants using either vasp or quantum expresso software and compare with SBS results.

Bibliography

[1] Margaret M Elcombe. The lattice dynamics of strontium fluoride. *Journal of Physics C: Solid State Physics*, 5(19):2702, 1972.

[2] V Shklover, M Schall, J Kraus, O Gloeckl, J Erxmeyer, H Feldermann, K Forcht, and U Heinemeyer. Optical element, July 12 2018. US Patent App. 15/912,722.

[3] R Eden and M Markides. Silicon Carbide and Gallium Nitride Power Semiconductors Report - 2018. *IEEE Power Electronics Magazine*, 5, 2018.

[4] GL Harris. *Properties of silicon carbide*. Number 13 in EMIS datareviews series. INSPEC, Institution of Electrical Engineers, 1995. ISBN 9780852968703. URL `https://books.google.co.za/books?id=Yy_B8GzxNlgC`.

[5] L Jiang and R Cheung. A review of silicon carbide development in MEMS applications. *International Journal of Computational Materials Science and Surface Engineering*, 2(3-4):227–242, 2009.

[6] VM Bermudez. Structure and properties of cubic silicon carbide (100) surfaces: a review. *Physica Status Solidi (b)*, 202(1):447–473, 1997.

[7] CJM van Rijn. Micro-engineered membranes. *Encyclopedia of Membrane Science and Technology*, 2013.

[8] J A Thornton. The microstructure of sputter-deposited coatings. *Journal of Vacuum Science & Technology A: Vacuum, Surfaces, and Films*, 4(6): 3059–3065, 1986.

[9] PM Sarro. Silicon carbide as a new MEMS technology. *Sensors and Actuators A: Physical*, 82(1-3):210–218, 2000.

[10] K Heinz, J Bernhardt, J Schardt, and U Starke. Functional surface reconstructions of hexagonal SiC. *Journal of Physics: Condensed Matter*, 16(17): S1705, 2004.

[11] GTA Kovacs et al. *Micromachined transducers source book*. WCB/McGraw-Hill New York, 1998.

[12] CE Woodell. Wear resistance of SiC. *Transactions of the Electrochemical Society*, 68:111–130, 1936.

[13] A Ong, J Carr, J Balda, and A Mantooth. A comparison of silicon and silicon carbide MOSFET switching characteristics. In *Region 5 Technical Conference, 2007 IEEE*, pages 273–277. IEEE, 2007.

[14] M Mehregany and CA Zorman. SiC MEMS: opportunities and challenges for applications in harsh environments. *Thin solid films*, 355:518–524, 1999.

[15] CH Wu, S Stefanescu, HI Kuo, CA Zorman, and M Mehregany. Fabrication and testing of single crystalline 3C-SiC piezoresistive pressure sensors. In *Transducers 01 Eurosensors XV*, pages 514–517. Springer, 2001.

[16] R Saha and WD Nix. Effects of the substrate on the determination of thin film mechanical properties by nanoindentation. *Acta materialia*, 50(1):23–38, 2002.

[17] S Crouch and DA Skoog. Principles of instrumental analysis. Australia: Thomson Brooks/Cole. Technical report, ISBN 0-495-01201-7, 2007.

[18] J Solé, L Bausa, and D Jaque. *An introduction to the optical spectroscopy of inorganic solids*. John Wiley & Sons, 2005.

[19] I Newton. *Opticks, or, a treatise of the reflections, refractions, inflections & colours of light*. Courier Corporation, 1979.

[20] S Mason et al. Lines of light-the sources of dispersive spectroscopy, 1800-1930, by JCD Brand. *Nature*, 381(6582):488–488, 1996.

[21] TC Ting. *Anisotropic elasticity: theory and applications*. Number 45. Oxford University Press on Demand, 1996.

[22] C Kittel, P McEuen, and P McEuen. *Introduction to solid state physics*, volume 8. Wiley New York, 1996.

[23] M Levy, HE Bass, R Stern, and V Keppens. *Handbook of Elastic Properties of Solids, Liquids, and Gases: Elastic properties of solids: theory, elements and compounds, novel materials, technological materials, alloys, and building materials*, volume 2. Academic Press, 2001.

[24] WC Van Buskirk, SC Cowin, and R Carter. A theory of acoustic measurement of the elastic constants of a general anisotropic solid. *Journal of Materials Science*, 21(8):2759–2762, 1986.

[25] MG Beghi and CE Bottani. Low–frequency Raman and Brillouin spectroscopy from graphite, diamond and diamond–like carbons, fullerenes and nanotubes. *Philosophical Transactions of the Royal Society of London A: Mathematical, Physical and Engineering Sciences*, 362(1824):2513–2535, 2004.

[26] L Brillouin. Diffusion de la lumière et des rayons x par un corps transparent homogène-influence de l'agitation thermique. In *Annales de physique*, volume 9, pages 88–122. EDP Sciences, 1922.

[27] F Nizzoli, A Franchini, and G Santoro. The interface polycarbonate-glass: A theoretical study of Brillouin Spectra and photoelastic properties. *Le Journal de Physique Colloques*, 45(C5):C5–55, 1984.

[28] R Vacher and L Boyer. Brillouin scattering: A tool for the measurement of elastic and photoelastic constants. *Physical Review B*, 6(2):639, 1972.

[29] E Gross. Change of wave-length of light due to elastic heat waves at scattering in liquids. *Nature*, 126(3171):201, 1930.

[30] EHL Meyer. EHL Meyer and W. Ramm, Physik. Z. 33, 270 (1932). *Physik. Z.*, 33:270, 1932.

[31] PR Stoddart, JD Comins, and AG Every. Brillouin-scattering measurements of surface-acoustic-wave velocities in silicon at high temperatures. *Physical Review B*, 51(24):17574, 1995.

[32] X Zhang, PR Stoddart, JD Comins, and AG Every. High-temperature elastic properties of a nickel-based superalloy studied by surface Brillouin scattering. *Journal of Physics: Condensed Matter*, 13(10):2281, 2001.

[33] CRA Catlow, JD Comins, FA Germano, RT Harley, and W Hayes. Brillouin scattering and theoretical studies of high-temperature disorder in fluorite crystals. *Journal of Physics C: Solid State Physics*, 11(15):3197, 1978.

[34] JG Dil. Brillouin scattering in condensed matter. *Reports on Progress in Physics*, 45(3):285, 1982.

[35] HZ Cummins. Brillouin scattering studies of phase transitions in crystals. In *Modern Problems in Condensed Matter Sciences*, volume 5, pages 359–447. Elsevier, 1983.

[36] JD Comins, PE Ngoepe, and CRA Catlow. Brillouin-scattering and computer-simulation studies of fast-ion conductors: a review. *Journal of the Chemical Society, Faraday Transactions*, 86(8):1183–1192, 1990.

[37] Z Bai, H Yuan, Z Liu, P Xu, Q Gao, RJ Williams, O Kitzler, RP Mildren, Y Wang, and Z Lu. Stimulated Brillouin scattering materials, experimental design and applications: A review. *Optical Materials*, 75:626–645, 2018.

[38] JR Sandercock. Fabry-perot interferometer, September 30 1980. US Patent 4,225,236.

[39] R Loudon and JR Sandercock. Analysis of the light-scattering cross section for surface ripples on solids. *Journal of Physics C: Solid State Physics*, 13 (13):2609, 1980.

[40] S Mishra and R Bray. Surface-ripple mechanism for Brillouin scattering of reflected light from bulk acoustic waves. *Physical Review Letters*, 39(4):222, 1977.

[41] R Loudon. Theory of surface-ripple Brillouin scattering by solids. *Physical Review Letters*, 40(9):581, 1978.

[42] AM Marvin, V Bortolani, and F Nizzoli. Surface Brillouin scattering from acoustic phonons. I. General theory. *Journal of Physics C: Solid State Physics*, 13(2):299, 1980.

[43] V Bortolani, AM Marvin, F Nizzoli, and G Santoro. Theory of Brillouin scattering from surface acoustic phonons in supported films. *Journal of Physics C: Solid State Physics*, 16(9):1757, 1983.

[44] DL Mills and KR Subbaswamy. II Surface and size effects on the light scattering spectra of solids. In *Progress in optics*, volume 19, pages 45–137. Elsevier, 1981.

[45] RJJ Riobóo, A Sánchez-Sánchez, and C Prieto. Optical find of hypersonic surface acoustic waves in bulk transparent materials. *Physical Review B*, 94 (1):014313, 2016.

[46] X Zhang, JD Comins, AG Every, PR Stoddart, W Pang, and TE Derry. Brillouin Scattering Study of Sezawa and pseudo-Sezawa waves in Ion-bombarded Silicon Layers. *Phys. Rev. B*, 58:13677–13685, 1998.

[47] AG Every, KY Kim, and AA Maznev. The elastodynamic response of a semi-infinite anisotropic solid to sudden surface loading. *The Journal of the Acoustical Society of America*, 102(3):1346–1355, 1997.

[48] AG Every and JD Comins. Surface Brillouin scattering. *Handbook of Advanced Nondestructive*, 2018.

[49] GW Farnell and EL Adler. Physical acoustics. *Mason, WP, Thurston RN,(eds.)*, 9:35, 1972.

[50] X Zhang, JD Comins, AG Every, PR Stoddart, W Pang, and TE Derry. Surface Brillouin scattering study of the surface excitations in amorphous silicon layers produced by ion bombardment. *Physical Review B*, 58(20): 13677, 1998.

[51] RD Arnell and PJ Kelly. Recent advances in magnetron sputtering. *Surface and Coatings Technology*, 112(1-3):170–176, 1999.

[52] S Ulrich, T Theel, J Schwan, V Batori, M Scheib, and H Ehrhardt. Low-temperature formation of β-silicon carbide. *Diamond and Related Materials*, 6(5-7):645–648, 1997.

[53] AV Singh, S Chandra, S Kumar, and G Bose. Mechanical and structural properties of RF magnetron sputter-deposited silicon carbide films for MEMS applications. *Journal of Micromechanics and Microengineering*, 22 (2):025010, 2012.

[54] W Kern. *Thin film processes II*, volume 2. Elsevier, 2012.

[55] K Wasa and S Hayakawa. Handbook of sputter deposition technology. 1992.

[56] RF Bunshah and JM Blocher. *Deposition technologies for films and coatings: developments and applications*. Noyes Data, 1982.

[57] PJ Kelly and RD Arnell. Magnetron sputtering: a review of recent developments and applications. *Vacuum*, 56(3):159–172, 2000.

[58] V Kouznetsov, K Macak, JM Schneider, Ulf Helmersson, and I Petrov. A novel pulsed magnetron sputter technique utilizing very high target power densities. *Surface and coatings technology*, 122(2-3):290–293, 1999.

[59] M Braun. Magnetron sputtering technique. *Handbook of Manufacturing Engineering and Technology*, pages 1–25, 2013.

[60] P Sigmund. Sputtering by ion bombardment theoretical concepts. In *Sputtering by particle bombardment I*, pages 9–71. Springer, 1981.

[61] SM Rossnagel. Sputter deposition. *Opportunities for Innovation: Advanced Surface Engineering*, 1995.

[62] R Kukla. Magnetron sputtering on large scale substrates: an overview on the state of the art. *Surface and Coatings Technology*, 93(1):1–6, 1997.

[63] CV Raman and KS Krishnan. A new type of secondary radiation. *Nature*, 121(3048):501, 1928.

[64] AM Herrero. Raman spectroscopy a promising technique for quality assessment of meat and fish: A review. *Food Chemistry*, 107(4):1642–1651, 2008.

[65] P Rostron, S Gaber, and D Gaber. Raman spectroscopy, review. *laser*, 21: 24, 2016.

[66] R Parma, KS Gour, Dinesh S, OP Singh, and VN Singh. The role of scanning electron microscope (SEM) in nanotechnology. *Encyclopedia of Nanoscience and Nanotechnology*, 30:479–503, 2018.

[67] M Birkholz. *Thin film analysis by X-ray scattering*. John Wiley & Sons, 2006.

[68] D Milathianaki, J Hawreliak, JM McNaney, BS El-Dasher, MD Saculla, DC Swift, HE Lorenzana, and T Ditmire. A Seeman–Bohlin geometry for high-resolution nanosecond x-ray diffraction measurements from shocked polycrystalline and amorphous materials. *Review of Scientific Instruments*, 80(9):093904, 2009.

[69] GR Janik. X-ray reflectivity measurement, March 23 2004. US Patent 6,711,232.

[70] GW Grime and M Dawson. Recent developments in data acquisition and processing on the Oxford scanning proton microprobe. *Nuclear Instruments and Methods in Physics Research Section B: Beam Interactions with Materials and Atoms*, 104(1-4):107–113, 1995.

[71] W Chu, JW Mayer, and M Nicolet. Backscattering spectroscopy, 1978.

[72] PA Saunders and JF Ziegler. Interactive computer analysis of nuclear backscattering spectra. *Nuclear Instruments and Methods in Physics Research*, 218(1-3):67–74, 1983.

[73] LR Doolittle. RUMP: Rutherford backscattering spectroscopy analysis package. *Nucl. Instrum. Methods Phys. Res., Sect. B*, 9:344, 1985.

[74] G Carlotti. Elastic Characterization of Transparent and Opaque Films, Multilayers and Acoustic Resonators by Surface Brillouin Scattering: A Review. *Applied Sciences*, 8(1):124, 2018.

[75] R Mock, B Hillebrands, and R Sandercock. Construction and performance of a Brillouin scattering set-up using a triple-pass tandem Fabry-Perot interferometer. *Journal of Physics E: Scientific Instruments*, 20(6):656, 1987.

[76] JD Bass, SV Sinogeikin, and B Li. Elastic properties of minerals: A key for understanding the composition and temperature of Earth's interior. *Elements*, 4(3):165–170, 2008.

[77] R Vacher, H Sussner, and M v Schickfus. A fully stabilized Brillouin spectrometer with high contrast and high resolution. *Review of Scientific Instruments*, 51(3):288–291, 1980.

[78] G Pakulski and F Holuj. Fiber-optics Brillouin scattering spectrometer. *Review of Scientific Instruments*, 61(5):1390–1394, 1990.

[79] P Mutti, CE Bottani, G Ghislotti, M Beghi, GAD Briggs, and JR Sandercock. Surface Brillouin scattering-extending surface wave measurements to 20 GHz. In *Advances in acoustic microscopy*, pages 249–300. Springer, 1995.

[80] JR Sandercock. High Contrast Tandem Fabry-Pérot Interferometer TFP-2 HC (Operator Manual). In *JRS TFPI Operator Manual*, pages 9–15. The Table Stable LTD., 1993.

[81] H Sussner and R Vacher. High-precision measurements of Brillouin scattering frequencies. *Applied optics*, 18(22):3815–3818, 1979.

[82] SV Sinogeikin and Jay D Bass. Single-crystal elasticity of pyrope and MgO to 20 GPa by Brillouin scattering in the diamond cell. *Physics of the Earth and Planetary Interiors*, 120(1-2):43–62, 2000.

[83] PH Gammon, H Kiefte, and MJ Clouter. Elastic constants of ice by Brillouin spectroscopy. *Journal of Glaciology*, 25(91):159–168, 1980.

[84] D Gerlich. Elastic constants of strontium fluoride between 4.2 and 300 K. *Physical Review*, 136(5A):A1366, 1964.

[85] E Morris, T Groy, and K Leinenweber. Crystal structure and bonding in the high-pressure form of fluorite (CaF_2). *Journal of Physics and Chemistry of Solids*, 62(6):1117–1122, 2001.

[86] V Kanchana, G Vaitheeswaran, and M Rajagopalan. Structural phase stability of CaF_2 and SrF_2 under pressure. *Physica B: Condensed Matter*, 328 (3-4):283–290, 2003.

[87] ME Thomas. Strontium Fluoride (SrF_2). In *Handbook of Optical Constants of Solids*, pages 883–897. Elsevier, 1997.

[88] SV Firstov, M Zhao, L Su, Q Yang, LD Iskhakova, EG Firstova, SV Alyshev, KE Riumkin, and EM Dianov. Optical properties of bismuth-doped KCl and SrF_2 crystals. *Laser Physics*, 26(9):096201, 2016.

[89] K Momma and F Izumi. VESTA 3 for three-dimensional visualization of crystal, volumetric and morphology data. *Journal of applied crystallography*, 44(6):1272–1276, 2011.

[90] TJ Glynn, W Hayes, and MCK Wiltshire. Raman scattering of F centres in SrF_2. *Journal of Physics C: Solid State Physics*, 10(1):137, 1977.

[91] D Van der Marel and HW Den Hartog. Raman spectroscopy of BaF_2:R^{3+} and SrF_2:R^{3+} solid solutions between 300 and 1400 K. *Physical Review B*, 25(11):6602, 1982.

[92] KC Crouch, RB Rayment, and GW Marks. Elastic Constants of Fluorides of Groups IA and IIA. Technical report, NAVAL UNDERSEA WARFARE CENTER SAN DIEGO CA, 1968.

[93] GB Benedek and K Fritsch. Brillouin scattering in cubic crystals. *Physical Review*, 149(2):647, 1966.

[94] T Błachowicz. Sezawa and love modes in Co/Cu superlattices. *Open Physics*, 1(4):574–595, 2003.

[95] AG Every, C Sumanya, BA Mathe, X Zhang, and JD Comins. Optimized determination of elastic constants of crystals and their uncertainties from surface Brillouin scattering. *Ultrasonics*, 69:273–278, 2016.

[96] A Kudelski. Analytical applications of Raman spectroscopy. *Talanta*, 76(1): 1–8, 2008.

[97] P Musumeci, F Roccaforte, and R Reitano. Angular distortion of Si clusters in a-SiC. *EPL (Europhysics Letters)*, 55(5):674, 2001.

[98] S Sorieul, JM Costantini, L Gosmain, L Thomé, and JJ Grob. Raman spectroscopy study of heavy-ion-irradiated α-SiC. *Journal of Physics: Condensed Matter*, 18(22):5235, 2006.

[99] A El Khalfi, ElM Ech-chamikh, Y Ijdiyaou, M Azizan, A Essafti, L Nkhaili, and A Outzourhit. Infrared and Raman study of amorphous silicon carbide thin films deposited by radio frequency co-sputtering. *Spectroscopy Letters*, 47(5):392–396, 2014.

[100] J Neuhäuser, G Treffer, H Plänitz, W Wagner, and G Marx. Grazing incidence X-ray diffraction analysis of surface modified SiC layers. *Fresenius' journal of analytical chemistry*, 358(1-2):333–334, 1997.

[101] A Höfgen, V Heera, F Eichhorn, and W Skorupa. Annealing and recrystallization of amorphous silicon carbide produced by ion implantation. *Journal of applied physics*, 84(9):4769–4774, 1998.

[102] A Elhaddad. *Growth of SiC by High Temperature CVD and Application of Thermo-gravimetry for an In-situ Growth Rate Measurement*. PhD thesis, Universität Duisburg-Essen, Fakultät für Ingenieurwissenschaften Maschinenbau und Verfahrenstechnik Institut für Verbrennung und Gasdynamik, 2010.

[103] M Matsukawa, S Murata, T Matsumoto, T Matsutani, and M Kiuchi. Brillouin scattering study on the wave properties in thin SiC films. *Ultrasonics*, 42(1-9):391–394, 2004.

[104] AM Hofmeister, KM Pitman, AF Goncharov, and AK Speck. Optical constants of silicon carbide for astrophysical applications. II. Extending optical functions from infrared to ultraviolet using single-crystal absorption spectra. *The Astrophysical Journal*, 696(2):1502, 2009.

[105] J Huran, I Hotovy, AP Kobzev, and NI Balalykin. RBS study of amorphous silicon carbide films deposited by PECVD. *Czechoslovak journal of physics*, 54(3):C1006, 2004.

[106] JN Bullock, C Bechinger, DK Benson, and HM Branz. Semi-transparent a-SiC: H solar cells for self-powered photovoltaic-electrochromic devices. *Journal of non-crystalline solids*, (Part 2):1163–1167, 1996.

[107] J Nelson. *The physics of solar cells*. World Scientific Publishing Company, 2003.

[108] QB Ma, A Galeckas, A Azarov, A Thøgersen, P Carvalho, DN Wright, S Diplas, OM Løvvik, V Jokubavicius, XY Liu, et al. Boron-implanted 3C-SiC for intermediate band solar cells. In *Materials Science Forum*, volume 858, pages 291–294. Trans Tech Publ, 2016.

[109] EF Schubert. *Light-emitting diodes*. E. Fred Schubert, 2018.

[110] IV Grekhov, PA Ivanov, TP Samsonova, AF Shulekin, and MI Vexler. SiC-based phototransistor with a tunnel MOS emitter. *IEEE Transactions on Electron Devices*, 46(3):577–579, 1999.

[111] VSN Chava, SU Omar, G Brown, SS Shetu, J Andrews, TS Sudarshan, and MVS Chandrashekhar. Evidence of minority carrier injection efficiency¿ 90% in an epitaxial graphene/SiC schottky emitter bipolar junction phototransistor for ultraviolet detection. *Applied Physics Letters*, 108(4):043502, 2016.

[112] K Kamitani, M Grimsditch, JC Nipko, CK Loong, M Okada, and I Kimura. The elastic constants of silicon carbide: A Brillouin-scattering study of 4H and 6H SiC single crystals. *Journal of applied physics*, 82(6):3152–3154, 1997.

[113] C Sumanya, JD Comins, and AG Every. Surface Brillouin scattering in opaque thin films. In *Journal of Physics: Conference Series*, volume 92, page 012103. IOP Publishing, 2007.

[114] JD Comins, AG Every, PR Stoddart, X Zhang, JC Crowhurst, and GR Hearne. Surface Brillouin scattering of opaque solids and thin supported films. *Ultrasonics*, 38(1-8):450–458, 2000.

[115] B Cros, E Gat, and JM Saurel. Characterization of the elastic properties of amorphous silicon carbide thin films by acoustic microscopy. *Journal of non-crystalline solids*, 209(3):273–282, 1997.

Publications

1. Elastic stiffness coefficients of single crystal SrF_2 by Brillouin light scattering.

Conference presentations

1. "Elastic stiffness coefficients of amorphous Silicon Carbide thin films by Brillouin light scattering" (Oral, awarded "Best MSc presentation"), 12th African Laser Centre (ALC) Student Workshop, Stellenbosch University, Cape Town, South Africa, 2018.

2. "Elastic constants of a-SiC thin films by Brillouin Spectroscopy" (Poster), 63th South African Institute of Physics Conference, Free State, South Africa, 2018.

3. "Elastic constants of as-deposited α Silicon Carbide thin films by Brillouin Spectroscopy" (Poster), DST-NRF Centre of Excellence in Strong Materials annual students workshop, University of the Witwatersrand, Johannesburg , South Africa, 2018.

4. "Elastic stiffness coefficients of single crystal SrF_2 by Brillouin light scattering" (Oral), African Materials Research Society International Conference (AMRS), Gaborone, Botswana, 2017.

5. "Elastic stiffness coefficients of single crystal SrF_2 by Brillouin light scattering" (Oral), 11th African Laser Centre (ALC) Student Workshop, Stellenbosch University, Cape Town, South Africa, 2017.

6. "Microscopic interface effects on Brillouin acoustic phonons of SrF_2" (Poster), 16th Frontiers of Electron Microscopy in Material Science International Conference, Johannesburg, South Africa, 2017.

7. "Elastic stiffness coefficients of single crystal SrF_2 by Brillouin light scattering" (Poster), 62th South African Institute of Physics Conference, Stellenbosch, South Africa, 2017.